Abstract

Title of Dissertation: Thermal and Magnetorotational Instability in the Insterstellar Medium

Robert Andrew Piontek, Doctor of Philosophy, 2005

Dissertation directed by: Professor Eve C. Ostriker
Department of Astronomy

We have performed three sets of numerical experiments designed to study turbulence in the interstellar medium (ISM) driven by the magnetorotational instability. Our models are local, account for galactic rotation and shear, include magnetic fields, and a cooling function which permits two stable phases of gas in pressure equilibrium.

The first set of simulations was performed in two dimensions, in the radial-vertical plane. These simulations laid the groundwork for the future 3D models to come. The numerical method for including the cooling function, as well as conduction, was developed and implemented. These simulations gave us a glimpse into the workings of the MRI in the presence of a two-phase medium.

In our second set of simulations we extend our models to three dimensions. This allowed us to study the saturated state of the MRI in the presence of a two-phase medium. The scaling of velocity dispersion with density was found to be steeper than that of single phase models, so that at low densities larger turbulent amplitudes were found. The interaction between MRI driven turbulence and the phase structure of the gas was examined in detail. We concluded that turbulence can drive gas into a thermally unstable state, but a two phase model of the ISM was still a fairly good approximation.

Finally, we added vertical gravity to our third set of models. Now, rather than specify the mean density, the vertical distribution of gas in the simulation domain is determined self-consistently. In these models cold dense clouds form due to TI and sink to the mid-plane. Turbulence driven by the MRI thickens the disk compared to non-turbulent models by as much as 100%. Turbulent amplitudes in the cold medium are relatively low, however, as the increased concentration of cold clouds near the mid-plane keep them relatively isolated from the more turbulent warm medium.

Whether or not the MRI is a significant source of turbulence in the ISM is still a question without a definitive answer, but this thesis has made significant progress in furthering our understanding of the behavior of the MRI in a two-phase medium.

Thermal and Magnetorotational Instability in the Insterstellar Medium

by

Robert Andrew Piontek

Dissertation submitted to the Faculty of the Graduate School of the
University of Maryland at College Park in partial fulfillment
of the requirements for the degree of
Doctor of Philosophy
2005

Advisory Committee:

Professor Eve C. Ostriker, Chair/Advisor
Professor James M. Stone
Professor James F. Drake, Dean's Representative
Professor Massimo Ricotti
Professor Stuart Vogel

To Buffy,

For her unconditional Love.

Acknowledgements

The past few years at the University of Maryland have been some of the most enjoyable of the thirty that I've lived so far, and the lifestyle of a graduate student is certainly one that I will miss. So, although I'm very happy to be (almost) done, and eagerly awaiting my flight to Germany where I'll spend the next few years with Franziska, these things come with some sadness.

I would like to thank the faculty, staff, and students of the Department of Astronomy, who made this experience what it was for me. A big part of the reason I decided to come to Maryland was because of the people I met while I was on my prospective visit. I just felt like I fit in a bit better here than the other places I visited. It was a good decision, and I was right. I have made quite a few good friends in this department, both students and faculty, and I will miss every one.

I'd like to thank my advisor, Eve Ostriker, of course, whom I've really enjoyed working with over the past few years. She has invested a large

fraction of her time working with me on this thesis, and for that I owe her my gratitude. The door to her office is always open, and whenever I show up (regularly) she almost always makes time for me, which is greatly appreciated. I hope that we can continue to work together for many years to come.

Finally, I'd like to thank my parents. I've been in school now for an amazing twenty five years, and my parents have been very supportive of me all along. Whenever I've needed anything, they have been there for me. It would have been impossible for me to have come this far without them.

Contents

List of Tables

List of Figures

Chapter 1

Introduction

The interstellar medium (ISM) is an important component of all galaxies, even though by mass it is only a fraction of the stellar mass, which itself is a small fraction of the inferred dark matter mass. A textbook view of the ISM often invokes the concept of a continual star-gas-star cycle (Bennet et al. 2005). Stars form through gravitational contraction of diffuse atomic gas into high density giant molecular clouds (GMCs). After the densest portion of the cloud collapses, pressure and temperature rise in the core, and nuclear fusion begins. Stars live most of their lives shining brightly, but eventually return much of their mass to the ISM through stellar winds and supernovae (SNE) explosions when the supply of nuclear fuel has run out. From this gas, new stars will form, and the star-gas-star cycle continues. In order to understand galaxy formation and evolution, we must first understand star formation, and thus we must also understand the dynamics of the ISM.

When considering the collapse of the ISM to form a protostar, it has long been recognized that taking into account only thermal pressure and gravitational contraction yields a time scale for star formation which is much shorter than is observed (Zuckerman & Palmer 1974). To avoid this problem, the ISM in the classical picture of star formation is threaded with a magnetic field, and gravitational collapse

is mediated by ambipolar diffusion (see Shu, Adams, & Lizano 1987, and references therein for a review). Magnetic pressure and tension slow the crush of gravity, but neutral material is able to drift through the field and collapse to form a protostar.

In recent years, however, both observational and theoretical problems with the magnetic regulation theory have led to the development of a theory in which star formation is largely mediated by interstellar turbulence, the primary source of which has been traditionally thought to be derived from SNE. The level of turbulence in the ISM may therefore strongly affect the star formation rate. From a simple point of view, the global star formation rate is expected to be proportional to the inverse of the Jeans time, $t_J = \sigma^2/G\Sigma$. Here Σ is the gas surface density, and σ^2 is a velocity dispersion including both thermal and turbulent contributions, $\sigma^2 = \sigma_{th}^2 + \sigma_{turb}^2$. High levels of turbulence could in principle suppress star formation altogether. However, large scale but lower amplitude turbulence could also help prompt star formation in regions of interacting blast waves, if there is enough time between shocks to allow collapse to occur. If comparatively little turbulence is present, the global star formation rate could be very high. The relationship between turbulence in the ISM and star formation is one to which we must pay particular attention. It is the study of the source of this turbulence, and the effect of turbulence on the properties of the ISM, which is the focus of this thesis.

Conditions in the ISM are highly variable. In molecular clouds, where star formation occurs, temperatures can be as low as 10 K, and densities as high as 10^5 cm^{-3}. At the other end of the spectrum, shocks from SNE can heat the ISM to temperatures of $10^7 K$, and densities in this ionized plasma can be as low as 0.001 cm^{-3}. Intermediate to these extremes we find the Warm Neutral Medium (WNM) and the Cold Neutral Medium (CNM), which are likely two distinct components of atomic gas existing in rough thermal and pressure equilibrium. The CNM has temperatures

in the range of 10-100 K, and densities of around 20-250 cm^{-3}. The WNM is hotter, with a temperature of around 8000 K, and a density of about 0.1-0.4 cm^{-3}. Gas at temperatures intermediate to the CNM and WNM is thought to be thermally unstable, so that it quickly heats or cools to become part of one of these two phases.

Thermal instability (TI) was first studied in detail by Field (1965) in the context of the ISM. The physical basis for TI is fairly simple. Various heating and cooling processes occur in which radiation is both emitted (cooling) and absorbed (heating) by the ISM. The ISM is in thermal equilibrium when the net heating and cooling rates are equal. These heating and cooling rates are a function of the local gas properties such as temperature, density, composition and ionization state. The net sum of these rates is called the cooling function, with the cooling (per volume) typically proportional to the square of the density and some function of temperature. If gas which is in thermal equilibrium is perturbed to lower temperatures, and continues to cool, the equilibrium is unstable. If gas in thermal equilibrium is perturbed to higher temperature, and continues to heat, it will also be unstable. A stable equilibrium is found when gas perturbed to cooler temperatures warms up, and gas perturbed to warmer temperatures cools back down. Later Field, Goldsmith, & Habing (1969) proposed that the ISM exists in three "phases", F (with T $\sim 10^4\ K$), G (T $\sim 5000\ K$), and H (T $\sim 100\ K$), in pressure equilibrium, with phase G being the thermally unstable phase. Since the time-scale is short for thermally unstable gas to heat or cool to one of the stable phases, phase G was suspected to be much less common in the ISM. Phase F, the warm gas, was proposed as the intercloud medium, enshrouding cold high density clouds of gas in phase H. Their model was in good agreement with observations of the time, and actually the values quoted for typical ISM temperatures, densities, and turbulence levels in this paper have not changed all that much.

This picture of the ISM is incomplete, however. As we already mentioned the ISM is also found to exist at very high temperatures, heated by shock-waves from SNE. The interaction of supernovae remnants (SNR) with the ISM was considered by Cox & Smith (1974), who found that for reasonable supernovae rates the galaxy should contain interconnected tunnel networks of low density gas. A few years later, the standard two phase model of the ISM was expanded to take into account the effects of SNR by McKee & Ostriker (1977, hereafter MO). Cold clouds were proposed to exist, enshrouded by the WNM, and then by a Warm Ionized Medium (WIM), ionized by the stellar UV background. MO proposed that most of the volume in the ISM is occupied by the Hot Ionized Medium (HIM), which is formed from the expanding shock waves of supernovae remnants. In this picture little or no gas is found in the unstable regime between the CNM and WNM, and rough pressure equilibrium is thought to hold between these phases, with the hot medium dictating the level. Although MO overestimated the volume fraction of the hot phase, this theory of the ISM is still quite relevant today, and is essentially the foundation on which many of today's modern numerical simulations are built.

Modern observations have made significant progress in determining the basic properties of the ISM, and are thus able to test the validity of the MO model. Heiles & Troland (2003) made observations of the 21cm line in both absorption and emission. For many of their sources they find good agreement with the MO model, in the sense that the neutral component of the ISM can be viewed as containing cold clouds which are enveloped by the WNM. They also find a higher volume and mass fraction of the WNM than is predicted by MO, as well as a larger fraction of gas in the unstable regime. About half of the WNM is unstable with temperatures between 500-5000 K. The mass weighted velocity dispersions are 7 and 11 km/s for the CNM and WNM, with mean temperature of 70K and 8000K, respectively.

The cold component "clouds" are interpreted as having a typical Mach number of around 3 (although these are "clouds" in velocity space, not physical space). They also find that the morphology of the CNM is sheet-like, consistent with a formation process driven by large scale shocks.

An absorption line survey of the 21cm line was also performed by Mohan, Dwarakanath, & Srinivasan (2004), also yielding a velocity dispersion of 7 km s^{-1}. A high velocity component with dispersion 21 km s^{-1} is detected as well. This high velocity component may be driven by shocks from SNE. By measuring absorption line widths of various ions, Redfield & Linsky (2004) measure the temperature and turbulent velocity of the local ISM. They find a temperature of 6680 K for the warm component, and a turbulent velocity of about 2 km s^{-1}. The turbulence is subsonic, with a typical Mach number of about 0.2. These are typical examples of the observations that numerical simulations strive to explain.

Contemporary simulations of the ISM contain some combination of a few key ingredients: self-gravity, heating due to star formation and/or supernovae, magnetic fields, vertical gravity, sheared rotational flow, and radiative heating/cooling. We have compiled a table of recent ISM simulations, Table 1.1, to summarize which of these physical effects were included in each model. The most common ingredient left out of the recipe is self-gravity, as it is difficult to handle numerically. To the best of our knowledge no simulation to date has included all of these effects in a single model. With density, temperature, length and time-scales varying by orders of magnitude, simulating the ISM is a computationally intensive problem, to say the least.

The majority of simulations are local, in the sense that they model a small part of the galaxy rather than the entire galaxy. Global simulations have a difficult time resolving the appropriate length scales (Wada, Spaans, & Kim 2000), and in fact

even local simulations struggle in this regard. Some researchers account for the vertical stratification of the galaxy (Korpi et al. 1999; de Avillez & Breitschwerdt 2004, 2005), which in some sense puts them somewhere between what would be considered local and global, as they allow material to be exchanged between the halo and the disc.

Star formation is modeled in many different ways. The most simplistic approach is to simply inject kinetic energy into the domain at some appropriate length scale (Gazol, Vázquez-Semadeni & Kim 2005). Sporadic thermal heating due to radiation from massive stars is sometimes included, though the energy input due to SNE is believed to dominate over these sources. In simulations that model SNE, typically the energy from a SN is simply injected into a small number of zones with a radius of typically a few pc. Both clustered and randomly distributed SNE can be modeled (de Avillez & Breitschwerdt 2004), as some stars explode within the environment from which they form, while others live long enough to escape the stellar nursery. Unfortunately, if self gravity is not included, clustered star formation will occur in regions of significantly lower density than is realistic. If the disk is stratified, the differing scale-heights of populations of SNE can be accounted for. The SNE rate is typically a parameter, and most authors thus far have used values which are comparable to or higher than what is considered typical for the Milky Way. The efficiency at which energy from SNE is deposited in the ISM is also a parameter, and a subject of debate. Only recently have authors considered SNE rates and efficiencies which are lower than what is observed for our galaxy (Dib, Bell & Burkert 2005). Slyz et al. (2005) include SNE in their simulations, as well as self-gravity. Mass is converted to stars, which are then evolved with a particle code, and these later explode in type II SNE. Some of the mass is also returned to the fluid portion of the code via. winds from massive stars. However, the critical density for which star

formation can occur is $n = 10$ cm^{-3}, which is quite low. Furthermore, the energy from a SNE event is deposited in a single computational zone. The relative fractions of energy transferred from the blast wave to radiative, kinetic, and magnetic energy may not be correct. To date, all simulations of the ISM which attempt to model star formation fall short of correctly including SNE with regards to at least one of the above mentioned issues.

The thermal structure of the atomic ISM was analyzed by Wolfire et al. (1995), and later updated in Wolfire et al. (2003). Results support a two-phase model of the atomic ISM, consistent with observations. Photo-electric heating from small grains and PAHs are the dominant heating source for atomic gas nearly everywhere in the galaxy, while cooling is primarily by the CII 158 um fine structure line in cold gas at densities greater than $n = 10$ cm^{-3}. At lower densities and higher temperatures, OI, recombination onto small grains and PAHs, Lyman α, and CI fine structure lines all contribute significantly to the cooling. The cooling curve adopted for the simulations presented in this dissertation is a piecewise power-law fit based on this data (Sánchez-Salcedo, Vázquez-Semadeni, & Gazol 2002). The time for the gas to cool was estimated by Wolfire et al. (2003) to be shorter than the time between shocks, therefore unstable gas should evolve into two distinct phases.

The particular form of the cooling function adopted in simulations varies from author to author. Many make use of Dalgarno & McCray (1972), extended to high temperatures when SNE are included. Uniform heating (representing diffuse starlight) is not always included, so a two-phase medium may or may not develop, even in the absence of turbulence and SNE. The particular form of the cooling curve can in principle have a significant effect on the mass and volume fractions observed in simulations, so making direct comparisons of these quantities from one simulation to another can be difficult.

Many authors have looked at the relative fractions of gas in the warm, cold, and unstable phases. Generally the picture that has emerged is that turbulence, regardless of the source, can drive gas from the stable phases into the unstable phase. Dynamics are just as important as thermodynamics. Higher levels of turbulence yield higher levels of unstable gas. This is primarily an issue of time-scales, whether the gas has enough time to cool before the next turbulent episode of supersonic shocks compress and heat the ISM.

Some authors have focused exclusively on the effects of TI in their simulations. Detailed TI simulations in one dimension (1D) have been performed by Burkert & Lin (2000); Sánchez-Salcedo, Vázquez-Semadeni, & Gazol (2002). TI itself has been examined as a potential source of turbulence in the ISM, driven by heating from star formation. Kritsuk & Norman (2002a,b, 2004) perform simulations of which the primary ingredient is a two-phase ISM. These authors concentrate on the turbulence which is produced as thermally unstable gas cools and separates into stable phases. Shocks propagating through a two-phase ISM may serve to transfer thermal energy to kinetic energy if phase transitions are induced (Koyama & Inutsuka 2000, 2002). Simulations of a converging flow in one dimension (Hennebelle & Pérault 1999, 2000) and two dimensions (2D) (Audit & Hennebelle 2005) find generally that cold clouds can be formed in this manner, and for their most turbulent runs (Audit & Hennebelle 2005) find large amounts of unstable gas. Near cold clouds, however, a two-phase medium is still found to be a reasonable description of the thermal state of the gas.

de Avillez and collaborators perform local simulations of the ISM with a vertical extent of typically 10 kpc, and a horizontal extent of 1 kpc. They concentrate their efforts on the effects of SNE, with earlier works addressing the formation of structure in the ISM (de Avillez 2000; de Avillez & Mac Low 2001a; de Avillez &

Berry 2001b). These simulations are stratified hydrodynamical simulations which account for the different types of SNE. They include a radiative cooling function, but do not include heating, so there is not a stable two-phase equilibrium. The authors generally find that they are able to reproduce chimneys, mushrooms, and worms, which are structures observed to be present in the ISM of the Milky Way and other galaxies.

With the inclusion of heating, more recent simulations have begun to address the issue of turbulence and the relative fractions of the ISM in the stable and unstable phases (de Avillez 2002; de Avillez & Breitschwerdt 2004). Most recently magnetic fields have been included (de Avillez & Breitschwerdt 2005). The importance of the disc-halo-disc duty cycle is stressed, where hot material is driven out of the plane of the galaxy and into the halo by SNE. Eventually the gas cools and rains back down on the disc, and the bubbles and outflows created in this process are important in addressing structure formation.

Though these simulations are quite complex and include a number of physical inputs, many questions remain. The majority of these simulations use a SNE rate which is equal to or larger than thought to be typical in the ISM. Simulations with star formation rates at or below those of the galaxy have more difficulty reproducing observed turbulent amplitudes (Dib, Bell & Burkert 2005). Many SNE should occur in the molecular component of the ISM, but self-gravity of the gas is not included in most of these models. SNE then occur in diffuse rather than dense gas, and the energy input to the diffuse ISM may thus be overestimated. In simulations which include SNE, significantly higher levels of turbulence are found in the warm medium than in the cold component (Korpi et al. 1999; de Avillez & Breitschwerdt 2004, 2005), which is not observed to be the case in the real ISM (Heiles & Troland 2003). Furthermore, observationally, turbulence levels are found to be independent

of whether or not active star formation is taking place (Dickey et al. 1990), which calls into question the idea that SNE are the primary driver of ISM turbulence.

The simulations described above mainly focus on turbulence driven by star formation. The aim of my thesis has been to explore another source of turbulence, the magnetorotational instability (MRI) (Balbus & Hawley 1991; Hawley & Balbus 1991, 1992; Balbus & Hawley 1992; Hawley, Gammie, & Balbus 1995, 1996). The MRI is a process which occurs in shearing disk systems, and has traditionally been studied in the context of accretion disks around protostars and compact objects (Hawley, Balbus & Stone 2001; Gammie, Shapiro, & McKinney 2004). There are two requirements for the MRI to be present: a weak magnetic field, and decreasing angular velocity outward through the disk. In the Milky Way and other spiral galaxies, the disk of the ISM satisfies these criteria. The basic mechanism of the MRI is as follows: an outward perturbation of a fluid element moves it to a new location where the angular velocity required to maintain rotational equilibrium is less than was present at its original location. It is therefore left behind fluid elements that are unperturbed while these fluid elements remain connected by the magnetic field. The magnetic field, however, has a tension force associated with it, and this tension force attempts to maintain the original angular velocity of the fluid element. Thus the fluid element gains angular momentum, moves outward, and the perturbation continues to grow. The reverse process occurs for inward perturbations. The MRI was found, in accretion disks, to produce MHD turbulence that transports angular momentum outward through the disk so that material can accrete on to the central object (Balbus & Hawley 1991). Sellwood & Balbus (1999) suggested the the MRI may similarly be a source of turbulence in the ISM of galaxies.

Magnetic fields are often neglected in simulations of the ISM. Comparisons between simulations with and without magnetic fields which focus on SNE find that

their role in the dynamics tends to be minor (de Avillez & Breitschwerdt 2005). The MRI has been studied in the context of accretion disks (Balbus & Hawley 1991; Hawley & Balbus 1991, 1992; Balbus & Hawley 1992; Hawley, Gammie, & Balbus 1995, 1996), but only recently has the role of the MRI begun to be addressed in the context of the ISM in galaxies. The MRI was studied in stratified local isothermal simulations with self gravity by Kim, Ostriker, & Stone (2003). They find velocity dispersions of $2-4$ km s^{-1}, somewhat lower than observed in our Galaxy. They suggested that that turbulent amplitudes may increase in a medium with large density contrasts between the cloud and intercloud medium, as is expected in a two-phase medium. Investigating this question has been one of my research goals, and is a focus of this thesis.

In this dissertation we attempt to answer a number of questions: How do turbulent amplitudes driven by the MRI differ from a single phase medium to a two-phase medium? How do growth rates of the MRI change in a two-phase medium? How does turbulence driven by the MRI affect the phase structure of the ISM? How does the MRI-driven turbulence affect the vertical structure of disks? We have addressed these questions by performing numerical simulations using the ZEUS MHD code. Our simulations are local, account for the shear of the galactic rotation curve, and include magnetic fields, satisfying the requirements for the MRI to be present. Our version of ZEUS has been modified to include cooling by optically thin radiation (due primarily to PAHs), as well as uniform heating (due to UV starlight). We also include conduction so that we can resolve the appropriate length scales of thermal instability, without which TI is most unstable at the grid scale.

With a few exceptions, our models are the only ones to include galactic shear and magnetic fields, which are the essential ingredients for the MRI, combined with a two-phase cooling function. Mac Low, Avillez, & Korpi (2004) performed a low

resolution, vertically stratified two-phase model of the ISM, with rotation and MHD (essentially the same simulation presented in Chapter 4 of this thesis) . However, the description and analysis was limited to two paragraphs in a conference proceedings. Korpi et al. (1999) include MHD, rotation, SNE, vertical gravity, cooling and heating, but make no mention of the MRI. Global simulations of the MRI in the galactic disk were performed by Dziourkevitch , Elstner, & Rüdiger (2004), but heating and cooling were not included.

In Chapter 2 (published as Piontek & Ostriker (2004)) we begin to explore the interplay between turbulence driven by the MRI and a two-phase medium with 2D numerical simulations. These simulations begin with gas that is initially thermally unstable at a density and pressure which is thought to be typical of the ISM. The gas quickly separates into a two-phase medium as the time-scale for TI is much shorter than the MRI. Initially turbulence levels are quite low as the MRI develops from small amplitude perturbations over the first few orbits. Late in the simulation the perturbed velocity reaches a modest level of around 1.5 km s^{-1}. With 2D simulations saturated-state turbulence is not possible, however. Instead, the channel solution becomes very strong. In three dimensions (3D) the channel solution breaks up from non-axisymmetric perturbations, and saturated-state turbulence can develop.

Thus in Chapter 3 we extend the simulations of the previous work to 3D in which we can study the saturated state of the MRI. This work was published as Piontek and Ostriker (2005). In these simulations the box size is double that of the 2D simulations, and the initial vertical magnetic field strength has been increased, closer to a realistic value. Turbulence levels can reach approximately as high as 8 km s^{-1} in all three phases. The ISM is still essentially a two-phase medium with little gas in the unstable regime at this level of turbulence.

In Chapter 4 we include the effects of stratification of the disk in our model. It

has been suggested that stratification may lead to differing turbulence levels and distributions compared to what was found in our non-stratified models. With these models, the mean density is no longer a prescribed value, but is determined self-consistently by vertical redistribution of gas.

Chapter 5 summarizes the results from this dissertation and highlights the main findings of this work. We also look ahead to future prospects for the study of the MRI in the ISM.

Table 1.1. Physical Effects Included in Simulations

Reference	F	V	G	S	M	C	H	Comments
de Avillez (2000)	L	X		X		X		Formation of thin and thick disc, some volume filling factors are computed, but does not have two stable phases
de Avillez & Mac Low (2001a)	L	X		X		X		Formation of mushroom shaped structures driven by SNE
de Avillez & Berry (2001b)	L	X		X		X		Formation of worms and chimneys
de Avillez (2002)	L	X		X		X	X	Heating is now included with two stable phases. Primarily looks at mixing through a tracer field. SNE rates are high. Temperature and density PDFs are presented. No cold gas present because of high SNE rate.
de Avillez & Breitschwerdt (2004)	L	X		X		X	X	Now really starting to look at the different phases. They stress the disk-halo duty cycle, which effects the filling factors
de Avillez & Breitschwerdt (2005)	L	X		X	X	X	X	Magnetic fields are now included. Half of the gas is unstable. Cool gas is formed by the interaction of shock compressed layers. The field delays transport of hot gas into the halo, but does not prevent it.
Mac Low, Avillez, & Korpi (2004)	L	X			X	X	X	Essentially this is the same stratified model that we are running now, with beta=1000, and H=250 pc. Very few details and results. They do say that the MRI may maintain velocity dispersions outside of star forming regions.
Mac Low et al. (2005)	L			X	X			Concentrates on the pressure distribution in the ISM, large variation, and large amount of gas out of thermal equilibrium. Their cooling function is not two-phase, but nevertheless they say that a multi-phase medium is not produced (as one might expect).
Balsara et al. (2004)	L			X	X	X		No cold gas. Concentrates on the development of the magnetic field. High SNE rates, starting with 8 times the galactic rate. Magnetic fields are amplified quickly.

Table 1.1 (cont'd)

Reference	F	V	G	S	M	C	H	Comments
Korpi et al. (1999)	L	X		X	X	X	X	No cold phase, but they do have shear, so they should have the MRI. Galactic SNE rate. They find two distinct phases, warm and hot. Seems to be rough pressure equilibrium, two distinct temperature phases, but density does not show two phases. Volume filling factors are included. Turbulent velocities in the cold are about 3 km $s^{-1}$and 10 km s^{-1}in warm. The warm scale height it 200 pc, cold is less than 100 pc. No mention of the MRI. Vázquez-Semadeni, Gazol, & Scalo (2000) says there is no heating, so in reality there is no TI, and no thermal equilibrium.
Slyz et al. (2005)	L		X	X		X		No thermal instability. The most interesting thing is that they self consistently model star formation, so that gas actually turns into stars, which is followed with a particle code. Some of the PDFs are two phase and look quite a bit like ours, but this is apparently some combination of SNE/cooling. Feedback was a source of high density gas and thus encouraged star formation.
Dziourkevitch , Elstner, & Rüdiger (2004)	G	X			X			Global models of the MRI. Isothermal equation of state. Lower turbulent velocities are found at the midplane. Turbulent velocities of around 5 km $s^{-1}$are observed.
Kritsuk & Norman (2002a)	L					X	X	Basically just decaying turbulence looking at the formation of a two phase medium. They have TI and a stable two phase equilibrium. The unstable phase is 11 to 25 percent (not sure if this is mass or volume).
Kritsuk & Norman (2002b)	L					X	X	Same as above but now they have time dependent heating which moves gas into and out of different phases. Mass weighted Mach number, for all phases, is subsonic, and looks comparable to our pure TI runs. Some quotes of mass/volume fractions.

Table 1.1 (cont'd)

Reference	F	V	G	S	M	C	H	Comments
Kritsuk & Norman (2004)	L					X	X	Again, similar to the above. Just TI. Mostly looks at the turbulent power spectrum as the gas cools. Box size is only 5 pc.
Koyama & Inutsuka (2000)	L					X	X	1D TI in a propagating shock. Wolfire et al. (1995) cooling function. TI produces a thin dense layer in the shock, which they think will form small molecular clouds.
Koyama & Inutsuka (2002)	L					X	X	2D Shock propagating through the ISM, with a two phase cooling function. They argue that the shock can cause material to become thermally unstable, at which point some fraction of the energy is converted to kinetic energy which is not easily lost.
Wada & Norman (1999)	G		X			X	X	Two phase model, 2D, global. Although the say they form a multiphase ISM, they say that this is an inadequate description. Typical velocity dispersion is 15-20 km s^{-1}.
Wada, Spaans, & Kim (2000)	G		X	X		X	X	2D, concentrate on SNE effects. Also they run models without SNE. Star formation is followed with test particles. Some talk about formation of HI holes, which are difficult to form with SNE. No comments on phase structure.
Wada & Norman (2001a)	G		X	X		X	X	Very similar to the above. Star formation to the 1999 paper. They say the density PDF is "one-point lognormal" but if you look at the figure you could argue that it's two-phase where most of the mass is. They say that the large HI cavities are not always caused by SNE, but are a natural feature of self gravitating radiative discs. Disc is far from pressure equilibrium, very dynamic. SNE is self consistent, and the actual rate varies quite a bit.

Table 1.1 (cont'd)

Reference	F	V	G	S	M	C	H	Comments
Wada (2001b)	L	X	X	X		X	X	Simulating the inner 100 pc of the galaxy. 3D now, but the box is only 32 zones/16 pc tall. Same results as above concerning the density PDF. Temperature distribution looks to be two phase. They argue that there is a large fraction of of gas at intermediate temperatures, which can't be understood in terms of multi-phase gas in pressure equilibrium.
Wada & Koda (2001c)	L/G		X			X	X	2D, inner 1 kpc rotating spiral potential. smooth spiral structure that forms in isothermal models does not form with cooling and gravitational instability. Some observational implications that you don't normally see in numerical papers.
Wada, Meurer, & Norman (2002)	G		X			X	X	Same numerics as the 1999 paper, but now at higher resolution. Lots of energy spectrum analysis. 2D. energy inputs from galactic rotation and self-gravity drive turbulence and are sustaining.
Chiang & Bregman (1988)	L					X	X	Heating due to star formation, but not localized heating due to SNE. Two fluid simulation, which is apparently unstable. Looks like TI to me, but I don't think they have a two phase cooling function.
Rosen & Bregman (1995)	L	X		X		X	X	No two phase medium. They have star formation, but it's not quite clear what that means. Rework of 1988 paper above. 2D but they do both X-Y and X-Z runs. They find filaments of neutral gas, with regions of hot gas filling the voids between them.
Audit & Hennebelle (2005)	L					X	X	Basically just a two phase converging flow, similar to Koyama & Inutsuka (2002). Good cooling function, though, based on Wolfire et al. (1995). They find a large fraction of the gas in the unstable regime for very turbulent flows, but even in this case the presence of a two phase medium is still seen, especially near cold clouds.

Table 1.1 (cont'd)

Reference	F	V	G	S	M	C	H	Comments
Hennebelle & Pérault (1999)	L					X	X	1D converging flow with TI, stressing that these kinds of flows can form cold clouds and structure.
Hennebelle & Pérault (2000)	L				X	X	X	Same as above, but with MHD. With a weak field the flow aligns the field. With stronger fields the flow and field must be aligned within 20-40 degrees of each other. Otherwise things are pretty much the same.
Vázquez-Semadeni, Gazol, & Scalo (2000)	L		X		X	X	X	2D TI, with forcing. Cooling function is a fit do Dalgarno & McCray (1972), and they actually show it in the paper. Looks like it is significantly different than ours, and could significantly affect the results. The PDFs sometimes show two-phase structure. Some simulations include forcing. In some cases the TI is only found to be of second order importance compared to the magnetic field, the coriolis force, stellar energy injection, and self gravity. Their TI runs look like ours, 'honeycomb' they call it. In Gazol et al. (2001) they say the signature of TI is erased.
Gazol et al. (2001)	L		X		X	X	X	Also says they have rotation, but but no mention of MRI, possibly because it's in-plane, 2D, 1000 kpc, localized heating due to SF, but not SNE. They find 50% of gas in the unstable regime. Few details and results. The main difference between this and Vázquez-Semadeni, Gazol, & Scalo (2000) is a more realistic cooling function (same as ours), and higher resolution.
Sánchez-Salcedo, Vázquez-Semadeni, & Gazol (2002)	L					X	X	Basically just TI in 1D with some forcing and various initial conditions. This is the paper we took the our cooling curve from. For some levels of forcing clouds do not condense.
Burkert & Lin (2000)	L					X	X	Detailed TI paper.

Table 1.1 (cont'd)

Reference	F	V	G	S	M	C	H	Comments
Dib, Bell & Burkert (2005)	L			X		X	X	They use the Dalgarno & McCray (1972) cooling function, augmented by Sutherland and Dopita. Only SNE are included. They look at a nice range of SNE rates and efficiencies. At low values they find the velocity dispersion is around 3 km $s^{-1}$for HI, at less than half the galactic value (not sure of the efficiency here). For low rates they say the velocity dispersion falls short by a factor 2-3, suggesting that other processes may be need to maintain turbulence.
Gazol, Vázquez-Semadeni & Kim (2005)	L					X	X	They have turbulent forcing. Same cooling function as ours. 2D. This is pretty similar to Sánchez-Salcedo, Vázquez-Semadeni, & Gazol (2002), but 2D. They concentrate on the pressure distribution, which gets wider as the Mach number of the forcing is increased. The fraction of unstable gas increases as well.

Note. — F - Local (L) or Global (G), V - Vertical Gravity, G - Self Gravity, S - Supernovae, M - Magnetic Fields, C - Cooling, H - Heating

Chapter 2

Thermal and Magnetorotational Instability in the ISM: Two-Dimensional Numerical Simulations

Abstract

The structure and dynamics of diffuse gas in the Milky Way and other disk galaxies may be strongly influenced by thermal and magnetorotational instabilities (TI and MRI) on scales $\sim 1 - 100$ pc. We initiate a study of these processes, using two-dimensional numerical hydrodynamic and magnetohydrodynamic (MHD) simulations with conditions appropriate for the atomic interstellar medium (ISM). Our simulations incorporate thermal conduction, and adopt local "shearing-periodic" equations of motion and boundary conditions to study dynamics of a $(100\ \mathrm{pc})^2$ radial-vertical section of the disk. We demonstrate, consistent with previous work, that nonlinear development of "pure TI" produces a network of filaments that con-

dense into cold clouds at their intersections, yielding a distinct two-phase warm/cold medium within ~ 20 Myr. TI-driven turbulent motions of the clouds and warm intercloud medium are present, but saturate at quite subsonic amplitudes for uniform initial $P/k = 2000$ K cm^{-3}. MRI has previously been studied in near-uniform media; our simulations include both TI+MRI models, which begin from uniform-density conditions, and cloud+MRI models, which begin with a two-phase cloudy medium. Both the TI+MRI and cloud+MRI models show that MRI develops within a few galactic orbital times, just as for a uniform medium. The mean separation between clouds can affect which MRI mode dominates the evolution. Provided intercloud separations do not exceed half the MRI wavelength, we find the MRI growth rates are similar to those for the corresponding uniform medium. This opens the possibility, if low cloud volume filling factors increase MRI dissipation times compared to those in a uniform medium, that MRI-driven motions in the ISM could reach amplitudes comparable to observed HI turbulent linewidths.

2.1 Introduction

The Galactic interstellar medium (ISM) is characterized by complex spatial distributions of density, temperature, and magnetic fields, as well as a turbulent velocity field that animates the whole system. The relative proportions of ISM gas in different thermal/ionization phases, and their respective dynamical states, may reflect many contributing physical processes of varying importance throughout the Milky Way (or external galaxies). Even considering just the Galaxy's atomic gas component, observable in HI emission and absorption, a wide variety of temperatures and pervasive high-amplitude turbulence is inferred (Heiles & Troland 2003), and a number of different physical processes may collude or compete in establishing these

conditions.

In the traditional picture of the ISM, turbulence in atomic gas is primarily attributed to the lingering effects of supernova blast waves that sweep through the ISM (Cox & Smith 1974; McKee & Ostriker 1977; Spitzer 1978). Densities and temperatures of atomic gas are expected to lie preferentially near either the warm or cold stable thermal equilibria available given heating primarily by the photoelectric effect on small grains (Wolfire et al. 1995, 2003). Thermal instability (TI) is believed to play an important role in maintaining gas near the stable equilibria (Field 1965).

Certain potential difficulties with this picture motivate an effort to explore effects not emphasized in the traditional model. In particular, because energetic stellar inputs are intermittent in space and time, while turbulence is directly or indirectly inferred to pervade the whole atomic ISM, it is valuable to assess alternative spatially/temporally *distributed* turbulent driving mechanisms. Candidate mechanisms recently proposed for driving turbulence include both TI (Koyama & Inutsuka 2002; Kritsuk & Norman 2002a,b) and the magnetorotational instability (MRI) (Sellwood & Balbus 1999; Kim, Ostriker, & Stone 2003). In addition to uncertainties about the source of turbulence in HI gas, other puzzles surrounding HI temperatures (e.g. Kalbera, Schwarz, & Goss (1985); Verschur & Magnani (1994); Spitzer & Fitzpatrick (1995); Fitzpatrick & Spitzer (1997)) have grown more pressing with recent observations (Heiles 2001; Heiles & Troland 2003). Namely, the Heiles and Troland observations suggest that significant HI gas ($\gtrsim 48\%$) could be in the thermally-unstable temperature regime between 500-5000 K. Using observational evidence from various tracers, Jenkins (2004) has also recently argued that very large pressures and other large departures from dynamical and thermal equilibrium are common in the ISM, and indicate rapid changes likely driven by turbulence. To assess and interpret this evidence theoretically, it is necessary to understand the nonlinear development of

TI, the effects of independent dynamical ISM processes on TI, and the ability in general of magnetohydrodynamic (MHD) turbulence to heat and cool ISM gas via shocks, compressions, and rarefactions.

In recent years, direct numerical simulation has become an increasingly important tool in theoretical investigation of the ISM's structure and dynamics, and has played a key role in promoting the increasingly popular notion of the ISM as a "phase continuum". In MHD (or hydrodynamic) simulations, the evolution of gas in the computational domain is formalized in terms of time-dependent flow equations with appropriate source terms to describe externally-imposed effects. Fully realistic computational ISM models will ultimately require numerical simulations with a comprehensive array of physics inputs. Recent work towards this goal that address turbulent driving and temperature/density probability distribution functions (PDFs) include the three-dimensional (3D) simulations of Korpi et al. (1999), de Avillez (2000), Wada (2001b), and Mac Low et al. (2005); and the two-dimensional (2D) simulations of Rosen & Bregman (1995), Wada, Spaans, & Kim (2000), Wada & Norman (2001a), and Gazol et al. (2001). Among other physics inputs, all of these simulations include modeled effects of star formation, with either supernova-like or stellar-like localized heating events that lead to expanding flows. For some of these models, the cooling functions also permit TI in certain density regimes.

Since many of the individual processes affecting the ISM's structure and dynamics are not well understood, in addition to comprehensive physical modeling, it is also valuable to perform numerical simulations that focus more narrowly on a single process, or on a few processes that potentially may interact strongly. This controlled approach can yield significant insight into the relative importance of multiple effects in complex systems such as the ISM. Using models that omit supernova and stellar energy inputs, it is possible to sort out, for example, whether the appearance

of phase continua in density/temperature PDFs requires localized thermal energy inputs, or can develop simply from the disruption of TI by moderate-amplitude turbulence such as that driven by MRI.

Recent simulations that have focused on the nonlinear development of TI under ISM conditions include Hennebelle & Pérault (1999), Burkert & Lin (2000), Vázquez-Semadeni, Gazol, & Scalo (2000), Sánchez-Salcedo, Vázquez-Semadeni, & Gazol (2002), Kritsuk & Norman (2002a,b), Vázquez-Semadeni et al. (2003). Previous simulations of MRI in 2D and 3D have focused primarily on the situation in which the density is relatively uniform, for application to accretion disks (e.g. Hawley & Balbus (1992), Hawley, Gammie, & Balbus (1995), Stone et al. (1996)). In recent work, Kim, Ostriker, & Stone (2003) began study of MRI in the galactic context using isothermal simulations, focusing on dense cloud formation due to the action of self-gravity on turbulently-compressed regions.

In this work, we initiate a computational study aimed at understanding how density, temperature, velocity, and magnetic field distributions would develop in the diffuse ISM in the absence of localized stellar energy input. Of particular interest is the interaction between TI and MRI. TI tends to produce a cloudy medium, and this cloudy medium may affect both the growth rate of MRI and its dissipation rate, and hence the saturated-state turbulent amplitude that is determined by balancing these rates. On the other hand, the turbulence produced by MRI may suppress and/or enhance TI by disrupting and/or initiating the growth of dense condensations. Evaluation of quasi-steady-state properties such as the mean turbulent velocity amplitude and the distribution of temperatures will await 3D simulations. In the present work, which employs 2D simulations, we focus on evaluation of our code's performance for studies of thermally bistable media, and on analysis of nonlinear development in models of pure TI, TI together with MRI, and MRI in a

medium of pre-existing clouds.

In §2, we describe our numerical methods and code tests. In §3, we present results from simulations of thermally unstable gas without magnetic fields, and in §4 we present results of models in which magnetic fields and sheared rotation have been added so that MRI occurs. Finally, in §5, we summarize our results, discuss their implications, and make comparisons to previous work.

2.2 Numerical Methods

2.2.1 Model Equations and Computational Algorithms

We integrate the time-dependent equations of magnetohydrodynamics using a version of the ZEUS-2D code (Stone & Norman 1992a,b). ZEUS uses a time-explicit, operator-split, finite difference method for solving the MHD equations on a staggered mesh, capturing shocks via an artificial viscosity. Velocities and magnetic field vectors are face-centered, while energy and mass density are volume-centered. ZEUS employs the CT and MOC algorithms (Evans & Hawley 1988; Hawley & Stone 1995) to maintain $\nabla \cdot \mathbf{B} = 0$ and ensure accurate propagation of Alfvén waves.

For the present study, we have implemented volumetric heating and cooling terms, and a thermal conduction term. We also model the differential rotation of the background flow and the variation of the stellar/dark matter gravitational potential in the local limit with $x \equiv R - R_0 \ll R_0$, where R_0 is the galactocentric radius of the center of our computational domain. The equations we solve are therefore:

$$\frac{\partial \rho}{\partial t} + \boldsymbol{\nabla} \cdot (\rho \mathbf{v}) = 0 \tag{2.1}$$

$$\frac{\partial \mathbf{v}}{\partial t} + \mathbf{v} \cdot \boldsymbol{\nabla} \mathbf{v} = -\frac{\boldsymbol{\nabla} P}{\rho} + \frac{1}{4\pi\rho}(\boldsymbol{\nabla} \times \mathbf{B}) \times \mathbf{B} + 2q\Omega^2 x\hat{x} - 2\boldsymbol{\Omega} \times \mathbf{v} \tag{2.2}$$

$$\frac{\partial \mathcal{E}}{\partial t} + \mathbf{v} \cdot \boldsymbol{\nabla} \mathcal{E} = -(\mathcal{E} + P)\boldsymbol{\nabla} \cdot \mathbf{v} - \rho\mathcal{L} + \boldsymbol{\nabla} \cdot (\mathcal{K}\boldsymbol{\nabla} T) \tag{2.3}$$

$$\frac{\partial \mathbf{B}}{\partial t} = \boldsymbol{\nabla} \times (\mathbf{v} \times \mathbf{B}) \tag{2.4}$$

All symbols have their usual meanings. The net cooling per unit mass is given by $\mathcal{L} = \rho\Lambda(\rho, T) - \Gamma$. We adopt the simple atomic ISM heating and cooling prescriptions of Sánchez-Salcedo, Vázquez-Semadeni, & Gazol (2002), in which the cooling function, $\Lambda(\rho, T)$, is a piecewise power-law fit to the detailed models of Wolfire et al. (1995). The heating rate, Γ, is taken to be constant at 0.015 erg $\mathrm{s}^{-1}\mathrm{g}^{-1}$. In the tidal potential term of equation (2.2), $q \equiv -d\ln\Omega/d\ln R$ is the local dimensionless shear parameter, equal to unity for a flat rotation curve in which the angular velocity $\Omega \propto R^{-1}$.

The present set of simulations is 2D, with the computational domain representing a square sector in the radial-vertical $(x-z)$ plane. In the local frame, the azimuthal direction $\hat{\phi}$ becomes the $\hat{y}$ coordinate axis; y-velocities and magnetic field components are present in our models, but $\frac{\partial}{\partial y} = 0$ for all variables. To reduce diffusion from advection in the presence of background shear, we apply the velocity decomposition method of Kim & Ostriker (2001). We employ periodic boundary conditions in the $\hat{z}$-direction, and shearing-periodic boundary conditions in the $\hat{x}$-direction (Hawley & Balbus 1992; Hawley, Gammie, & Balbus 1995). This framework allows us to incorporate realistic galactic shear, while avoiding numerical artifacts associated with simpler boundary conditions.

Because cooling times can be very short, the energy equation update from the net cooling terms is solved implicitly using Newton-Raphson iteration. At the start

of each iteration the time step is initially computed from the CFL condition using the sound speed, Alfvén speed, and conduction parameter. This is followed by a call to the cooling subroutine. The change in temperature within each zone is limited to ten percent of its initial value. If this requirement is not met for all cells in the grid, the time step is reduced by a factor of two, and the implicit energy update is recalculated. Tests with our cooling function show that this time step restriction could in principle become quite prohibitive if zones were far from thermal equilibrium. In practice, though, for our model simulations this is typically not the case, and the time step is reduced once or twice at most.

The update from the conduction operator is solved explicitly, using a simple five point stencil for the spatial second derivative of temperature (cf. Press et al. (1992) equation 19.2.4). In two dimensions the CFL condition is $\Delta t < (\Delta x)^2[nk/(\gamma - 1)]/(4\mathcal{K})$. As (Koyama & Inutsuka 2003) have recently pointed out, the importance of incorporating conduction in simulations which contain thermally unstable gas has been occasionally overlooked in past work. Without conduction, the growth rates for thermal instability are largest at the smallest scales, and unresolved growth at the grid scale may occur.[1] The inclusion of conduction, however, has a stabilizing effect on TI at small scales, and the conduction parameter can be adjusted to allow spatial resolution of TI on the computational grid. Here, we treat $\mathcal{K}$ as a parameter that may be freely specified for numerical efficacy; we discuss the physical level of conduction in the ISM below.

[1]Similar numerical difficulties arise if the Jeans scale is not resolved in simulations of self-gravitating clouds (Truelove et al. 1997).

2.2.2 Code Tests

The ZEUS MHD code has undergone extensive numerical testing and has been used in a wide variety of astrophysical investigations. In addition, we have tested the code without cooling and conduction and have found it can accurately reproduce the linear growth rates of the MRI for an adiabatic medium (see also (Hawley & Balbus 1992)). To test our implementation of the heating, cooling, and conduction terms, we performed 1D simulations to compare with the linear growth rates of the thermal instability (Field 1965). The models were initialized with eigenmodes of the instability, and three levels of conduction were chosen: $\mathcal{K} \in (7.48 \times 10^6, 7.48 \times 10^7, 7.48 \times 10^8)$ erg cm^{-1} K^{-1} s^{-1}. For these tests, the grid was 128 zones and the box size $L = 100$ pc. The initial density and pressure were set to $n = 0.79$ cm^{-3} and $P/k = 2000$ cm^{-3} K, implying corresponding cutoffs for thermal instability ("Field Length"), $\lambda_{\rm F} \in \{2.7, 8.4, 27\}$ pc for our adopted cooling function (see §3.1) [2]. In Figure 2.2 we plot the growth rates from the simulations on top of the analytic curves. The numerical growth rates are obtained by measuring the logarithmic rate of change of the maximum density. The agreement between the analytic and numerical growth rates is quite good. This test confirms that the newly added cooling and conduction subroutines are working correctly, and is critical in assessing the performance of the code as applied to multi-phase ISM simulations. Note that at small scales TI is essentially isobaric, so that this test demonstrates the ability of the code to maintain near-uniform pressure via hydrodynamic flow to compensate for changes in temperature driven by the cooling term (see eq. 3).

By comparison with simulations in which we set $\mathcal{K} = 0$, tests with non-zero $\mathcal{K}$ also confirm that conduction provides a needed numerical stabilization. When

[2] The Field length is $\lambda_F = 2\pi \left[\frac{\rho^2 \Lambda}{\mathcal{K} T}\left(1 - \frac{\partial ln \Lambda}{\partial ln T}\right)\right]^{-1/2}$ when $\Lambda =$ function of T.

conduction is omitted, growth rates for TI will always be greatest at the largest available wavenumbers. Our 2D tests with $\mathcal{K} = 0$ have confirmed this is indeed the case: simulations in which TI is seeded from random perturbations form high density clouds which are the size of a single grid zone. Further 2D tests show that provided $\lambda_{\rm F}$ is resolved by at least 8 zones, this grid-scale growth is suppressed. For the models we shall present, the conduction parameter and grid resolution were chosen such that we can adequately resolve all modes for which TI is unstable.

Because we are modeling a medium containing very large density contrasts, it is desirable to assess the evolution of contact discontinuities between the high and low density regions, representing cold and warm phases in pressure equilibrium. The diffusive smearing of contact discontinuities is an inherent limitation of all finite difference codes, but the numerical problem can be magnified with the inclusion of a thermally bistable net cooling function. As these contact discontinuities are advected through the grid, upstream and downstream zones adjacent to the discontinuity are set to intermediate densities which may be thermally unstable. Thermally unstable gas adjoining the initial contact rapidly heats or cools to reach a pressure different from the initial equilibrium, and this can potentially introduce additional dynamics to the problem.

To explore this numerical issue for the problem at hand, we have performed 1D advection tests of relaxed profiles of high density clouds in a low density ambient medium. The resolution is 512 zones for all runs. We define $n_c \equiv \lambda_F/\delta x$, i.e. the number of zones in a Field length at the mean density, giving a measure of the resolution at scales for which conduction is important. We vary $\mathcal{K}$ so that n_c varies from 8 to 32 in powers of 2. The initial conditions consist of a top-hat function of high and low density set to be in approximate pressure equilibrium. The exact equilibrium state is the solution of $\rho\mathcal{L} = \nabla \cdot (\mathcal{K}\nabla T)$ from equation (2.3), and is

different for each value of $\mathcal{K}$. Initial oscillations in pressure, velocity, and density gradually decay, and we consider the profile to be relaxed when these oscillations reach approximately one percent of their value early in the simulation. After a relaxed "cloud" profile is achieved the velocity of all cells is set to a constant value comparable to the sound speed, and the "cloud" is advected through the grid twice. Profiles at the end of these runs are compared to the initial relaxed equilibrium profile in Figure 2.1. Notice that as n_c increases so does the number of zones over which the contact discontinuity is spread; the results clearly show that the profile is preserved more faithfully as n_c increases from 8 to 32. For comparison we also show results from the original ZEUS-2D code, without conduction and cooling.

It is clear that running higher levels of conduction at a given resolution has the advantage of smearing contact discontinuities over an increasing number of zones, thus improving the performance of the code in the advection tests. However, increasing $\mathcal{K}$ has the disadvantage of inhibiting thermal instability at larger and larger spatial scales, such that only very large scale structures can develop from thermal instability. As we are interested in how wavelengths of growing MRI modes in a cloudy medium may be affected by the distances between condensations, it is undesirable to limit the available dynamic range for this exploration. For $n_c = 32$ at a resolution of 256 zones, λ_F is 12.5pc, and the maximum TI growth rate occurs at 29 pc, about one third of our box. A second disadvantage of increasing $\mathcal{K}$ is that conduction quickly begins to set the time step for the simulations. So, we make the practical choice of setting $n_c = 8$. At resolution of 256^2, and a box size of 100 pc, we then set $\mathcal{K} = 1.03 \times 10^7$ erg cm^{-1} K^{-1} s^{-1}, to yield $\lambda_F = 3.125$ pc. This compromise choice allows us to resolve TI developing from the initial conditions, to maintain advection profiles within $\sim 20\%$, and to have adequate numbers and resolution of the condensations that form to represent a cloudy medium in a meaningful way.

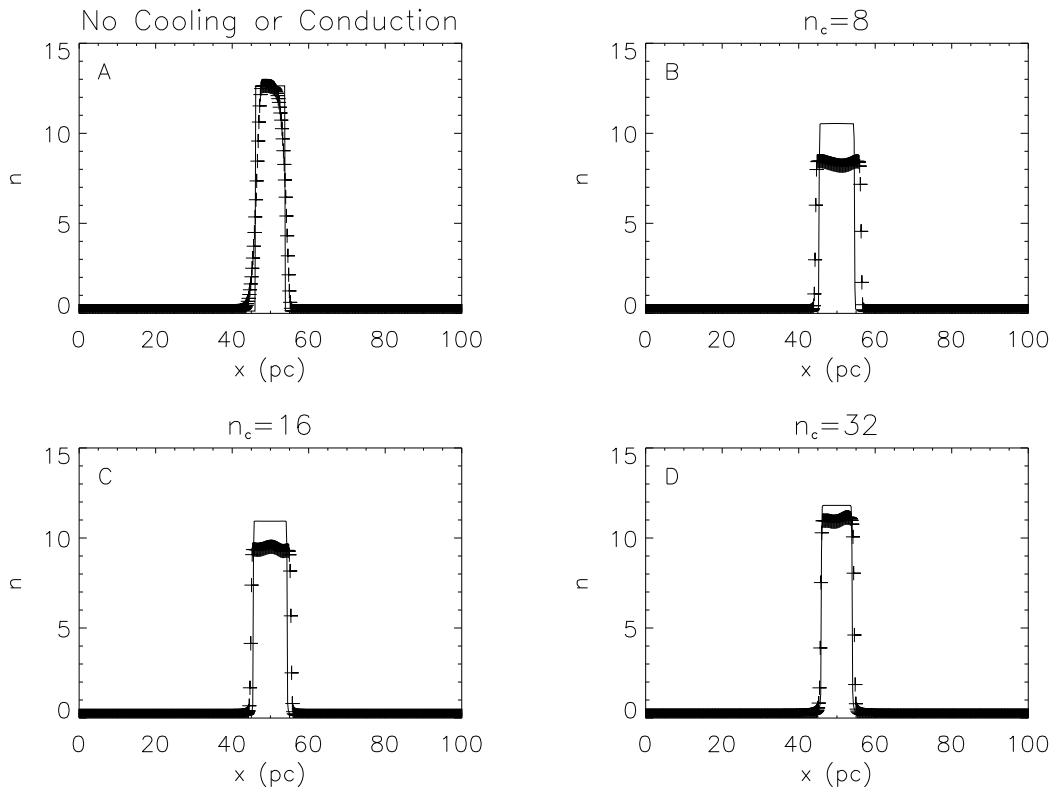

Figure 2.1: Advection test results (crosses) compared with the initial profile (solid line) of a 1D cloud. In Panel A we show results from the original ZEUS-2D code, without cooling and conduction. In Panels B, C, and D we set the conduction parameter so that $n_c = 8$, 16, and 32, respectively. Advection test results improve as n_c increases.

The true thermal conduction level in the ISM is not well known observationally, and must be affected by the fractional ionization (since electrons are highly mobile when present) and magnetic field geometry. A minimum level of conduction for the atomic ISM is that of neutral hydrogen gas, $\mathcal{K} = 2.5 \times 10^3\ T^{1/2}$ erg cm^{-1} K^{-1} s^{-1} (Parker 1953). At 2000 K, $\mathcal{K} = 1.1 \times 10^5$ erg cm^{-1} K^{-1} s^{-1}, about a factor of one hundred smaller than our value, such that λ_F would be reduced by a factor ~ 10. The use of a smaller conduction parameter would not, however, significantly alter our main results. The most unstable wavelength for TI (see Figure 2.2) would be significantly smaller, 3 pc compared to 12 pc for our adopted $\mathcal{K}$ – which would reduce

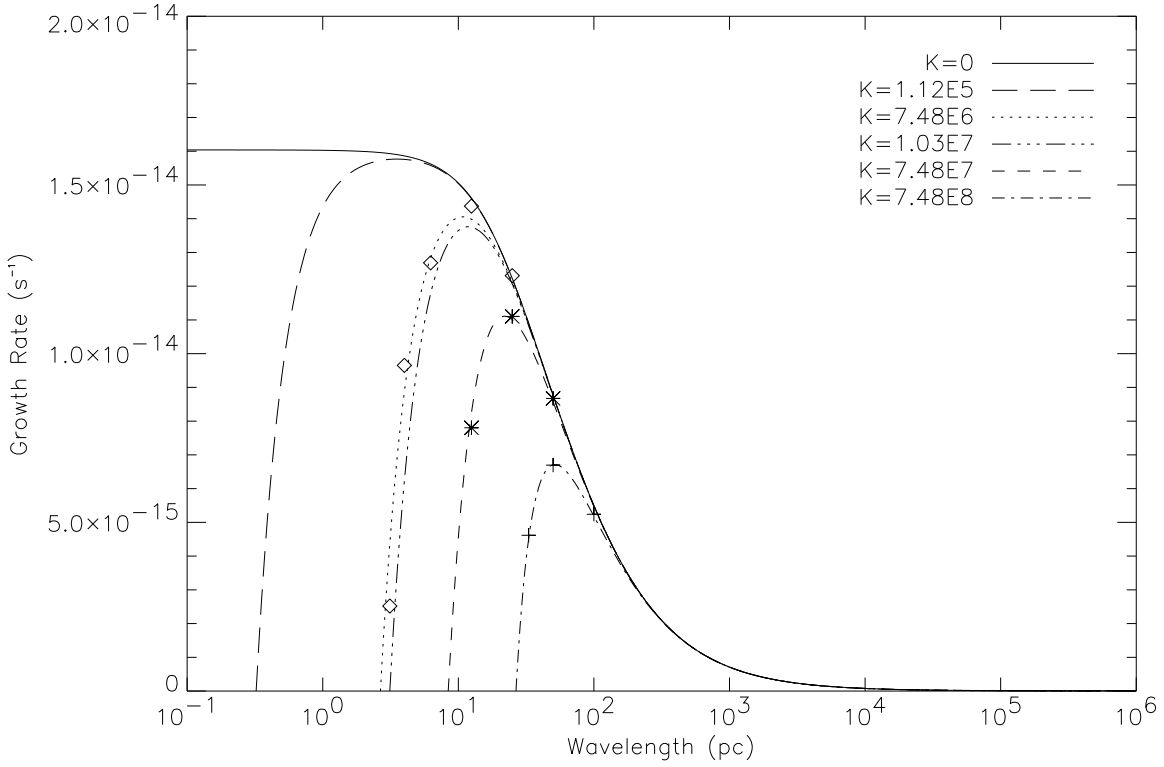

Figure 2.2: Theoretical thermal instability growth rates (Field 1965) for varying levels of conduction $\mathcal{K} = 7.48 \times 10^6, 10^7, 10^8$ (curves as indicated), overlayed with measured growth rates (points) from test simulations. For reference we include the theoretical curves for $\mathcal{K} = 0$ and for our chosen value of $\mathcal{K} = 1.03 \times 10^7$ erg cm^{-1} K^{-1} s^{-1}, as well as using an estimate of the physical conduction in the ISM at 2000K, $\mathcal{K} = 1.12 \times 10^5$ erg cm^{-1} K^{-1} s^{-1}. The asymptotic growth rate at small scales is (2 Myr)$^{-1}$ for the adopted parameters.

the size scale of the clouds in the initial condensation phase. However, the growth rate of TI for the most unstable wavelength would increase by only 15% compared to our models. The evolution towards more massive clouds via agglomeration would proceed similarly to the results we have found. In addition, the overall tendency to maintain a two-phase medium after TI has developed, as well as the characteristics we identify for MRI growth in a cloudy medium, would not be affected by the initial sizes of clouds that form.

2.3 Thermal Instability Simulations

2.3.1 Physical Principles and Timescales

Various heating and cooling processes in the ISM define a thermal equilibrium pressure-density curve on which energy is radiated at the same rate it is absorbed. Perturbations from the equilibrium curve will either be stable or unstable depending on its local shape (Field, Goldsmith, & Habing 1969). Our adopted equilibrium curve (Vázquez-Semadeni, Gazol, & Scalo 2000) is shown in Figure 2.3 (together with contours of temperature corresponding to transitions in the cooling function, and with scatter plots from our first simulation). Gas in the region above the curve has net cooling ($\mathcal{L} > 0$), and gas below the curve net heating ($\mathcal{L} < 0$). When gas on the equilibrium curve in the warm phase (phase "F", at T $>$ 6102 K) is perturbed to higher (lower) temperatures, there is net cooling (heating) and the gas returns to equilibrium. The same situation applies to gas in the cold phase (phase "H", at T $<$ 141 K). At intermediate temperatures (phase "G", 313 K $<$ T $<$ 6102 K), however, perturbations from equilibrium to higher (lower) temperatures results in net heating (cooling), and the gas continues heating (cooling) until it reaches equilibrium in Phase F (H). This is the physical basis for TI, which was first analyzed comprehensively by Field (1965).

Thermal instability has long been believed to play an important role in structuring the ISM because at typical volume-averaged atomic densities estimated for the ISM (e.g. $n_{HI} = 0.57$ from Dickey & Lockman (1990)) gas in thermal equilibrium would lie on the unstable portion of the curve. Thus, much of the mass of the ISM in the Milky Way and similar galaxies is believed to be in cold clouds or a warm intercloud medium, the two stable neutral atomic phases (e.g. Wolfire et

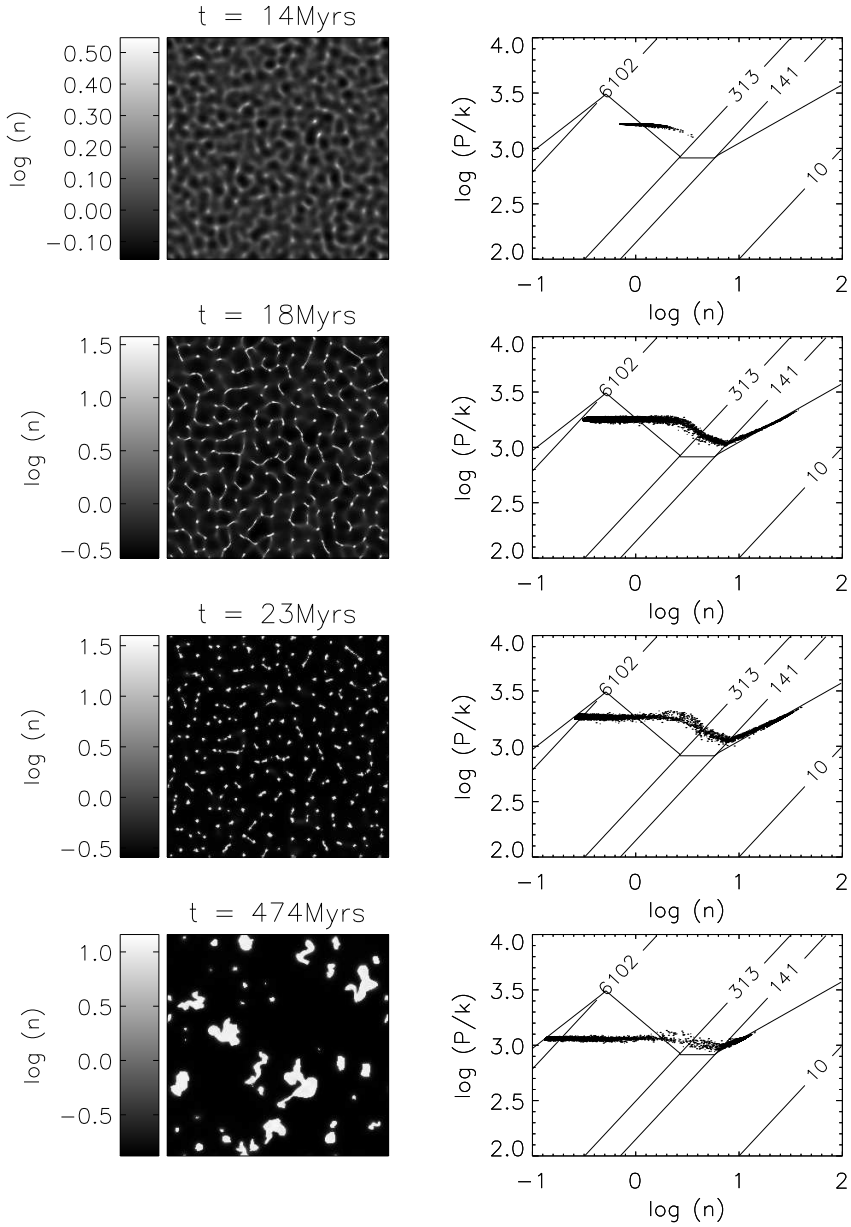

Figure 2.3: Density evolution in the TI simulation. *Left*: snapshots of $\log(n)$ at representative times as noted. *Right*: scatter plots of n and P/k from the simulation, together with the equilibrium cooling curve and the labeled temperature contours that demark the transitions between the F, G, and H phases.

al. (2003)). Recent theoretical work has emphasized that dynamical processes may drive gas away from these two stable phases, potentially explaining observationally-inferred temperatures that depart from equilibrium expectations; we shall discuss these issues in § 2.5. It is, nevertheless, of significant interest to study in detail how TI develops nonlinearly to establish a two-phase cloudy medium in the absence of other potential effects such as localized heating, impacts from large-scale shocks, or stresses associated with MHD turbulence. Results of these carefully-controlled "pure TI" simulations are valuable for characterizing the timescale to develop a two-phase medium as well as its structural and kinetic properties. "Pure TI" models also represent a baseline for comparison of models incorporating more complex physics.

Once the particular form of the cooling curve has been chosen, the development of TI is primarily a function of four parameters: the cooling time, t_{cool}, the heating time, t_{heat}, the sound crossing time, t_{sound}, and the conduction length scale, λ_F. The cooling time depends on the specific cooling function; for the cooling curve we adopt (Sánchez-Salcedo, Vázquez-Semadeni, & Gazol 2002), in varying temperature regimes we have

$$t_{cool} = \frac{\mathcal{E}}{\rho^2 \Lambda} = \begin{cases} 1.2 \times 10^4 \text{ yr } \frac{(P/k)/2000}{(n/20)^2 (T/100 \text{ K})^{2.12}} & 10 \text{ K} < T < 141 \text{ K} \\ 1.5 \times 10^4 \text{ yr } \frac{(P/k)/2000}{(n/10)^2 (T/200 \text{ K})^{1.00}} & 141 \text{ K} < T < 313 \text{ K} \\ 3.7 \times 10^5 \text{ yr } \frac{(P/k)/2000}{(n/1)^2 (T/2000 \text{ K})^{0.56}} & 313 \text{ K} < T < 6102 \text{ K} \\ 1.1 \times 10^6 \text{ yr } \frac{(P/k)/2000}{(n/0.25)^2 (T/8000 \text{ K})^{3.67}} & 6102 \text{ K} < T < 10^5 \text{ K} \end{cases} \tag{2.5}$$

The heating time,

$$t_{heat} = \frac{\mathcal{E}}{\rho \Gamma} = 4.1 \times 10^5 \text{ yr} \frac{(P/k)/2000}{(n/1)} \tag{2.6}$$

for $\Gamma = 0.015$ erg s^{-1}g^{-1}. We can also define an effective cooling/heating time as $t_{cool,eff} = |t_{cool}^{-1} - t_{heat}^{-1}|^{-1}$; at thermal equilibria, $t_{cool,eff}$ becomes infinite. The sound

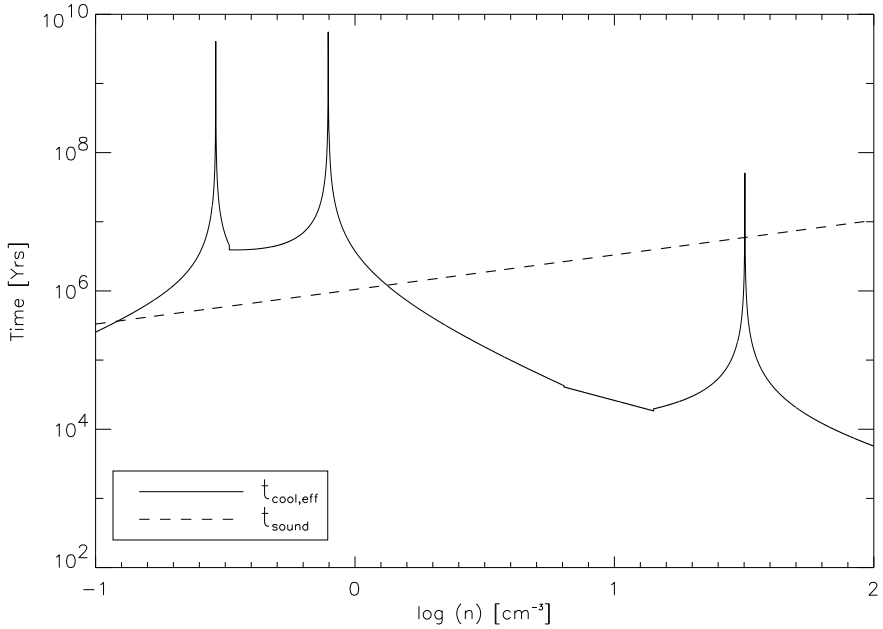

Figure 2.4: Comparison of $t_{cool,eff}$ and t_{sound} as a function of less than the effective cooling time, so that gas can evolve at approximately constant pressure. For higher densities, $t_{cool,eff}$ is typically an order of magnitude shorter than t_{sound}, and the gas tends to cool towards the equilibrium curve. The peaks where $t_{cool,eff}$ approaches infinity represent the equilibrium densities (n= 0.29 cm^{-3}, 0.78 cm^{-3}, 32 cm^{-3}) at which heating and cooling rates are equal for $P/k = 2000$.

crossing time over distance ℓ is

$$t_{sound} = \frac{\ell}{c_s} = 1.1 \times 10^6 \text{ yr} \frac{\ell/5\,\text{pc}}{(T/2000\text{ K})^{1/2}} \tag{2.7}$$

In Figure 2.4, we plot $t_{cool,eff}$, and t_{sound} for $\ell = 5\,\text{pc}$ as a function of density for $P/k = 2000$ K cm^{-3}. For a range of densities 0.1 cm^{-3} < n < 1 cm^{-3}, the sound crossing time is significantly shorter than the effective cooling time; otherwise t_{sound} is typically more than an order of magnitude longer than $t_{cool,eff}$.

To simulate thermal instability under conditions representative of the general diffuse ISM, we adopt an initial density of $n = 1$ cm^{-3} and set the initial pressure to $P/k = 2000$ K cm^{-3}; all velocities are initially set to zero. Random pressure perturbations with an amplitude less than 0.1% are added to seed the TI . The gas is initially in a weakly cooling state, since the equilibrium pressure corresponding

to $n = 1$ cm^{-3} is $P/k = 1660$ K cm^{-3}. The simulation proceeds for 470 Myr, corresponding to two galactocentric orbits at the solar circle.

2.3.2 Structural Evolution

The initial development of TI proceeds quickly. In Figure 2.3 we show four snapshots at different times of the density distribution alongside scatter plots of pressure versus density overlayed on the equilibrium cooling curve. Structure begins to form at about 5 Myr, and density contrasts continue to increase at constant pressure until 14 Myr as shown in Figure 2.3. The Fourier transform of the density distribution at this time, Figure 2.5, shows that the majority of the power is concentrated at $k = 14$. Allowing for geometrical factors, this is consistent with the one-dimensional linear theory prediction that the most unstable wavelength is $k \sim 9$ for our chosen value of conduction. A network of filaments briefly forms at about 18 Myr connecting the regions of highest density, with flow moving along the filaments increasing the number density to as high as 18 cm^{-3}. By 23 Myr the dense gas has collected in condensations and has relaxed to approximate thermal equilibrium. The size scale of the cold clumps is initially only a few parsecs and is relatively uniform. However, random motions of the newly formed clouds leads to merging and disassociation; conductive evaporation at its boundaries can also alter the shape of a clump. By the end of the simulation, at 474 Myr, the typical cloud size has increased significantly to ~ 10 pc, though a number of smaller clouds either remain from the initial TI development or have formed as a result of disassociation.

In Figure 2.6, Panels A, B, and C, we plot the volume-weighted and mass-weighted density probability distribution functions (PDFs) for the first three snapshots from Figure 2.3. At t=14 Myr, in Panel A, all of the gas is in the unstable range. Already, though, in Panel B, after 18 Myr, the distribution has begun to

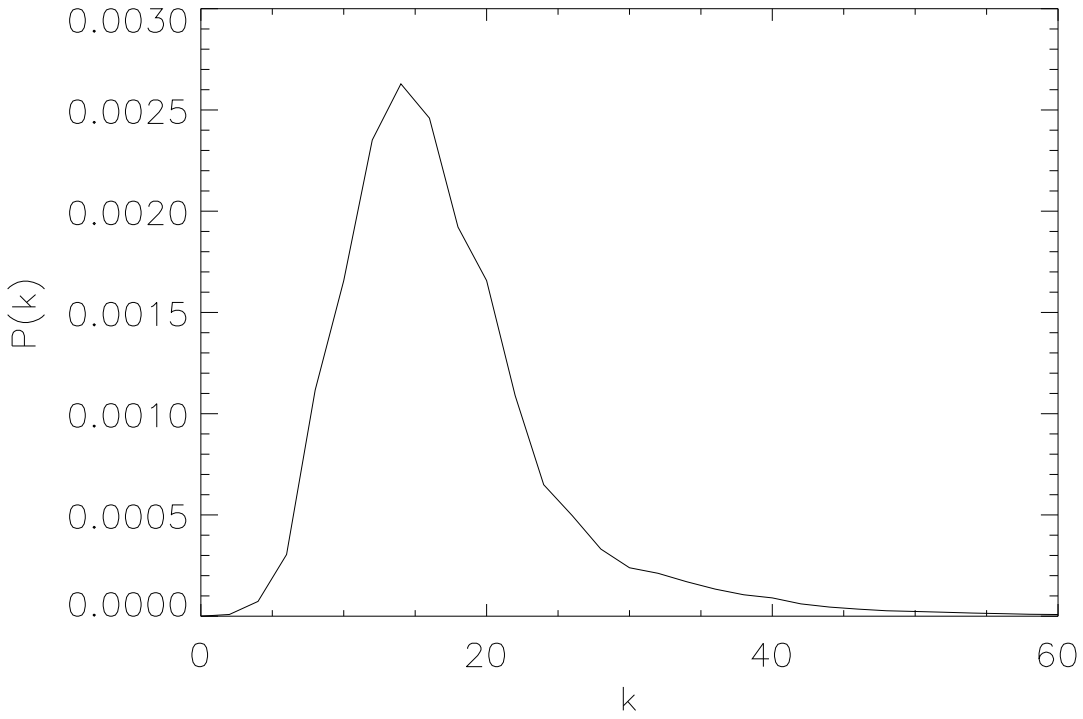

Figure 2.5: Power spectrum of the TI density distribution at 14 Myr.

separate into two distinct phases. At t=18 Myr, 69%, 28%, and 3% of the gas by volume is in the F (warm), G (unstable), and H (cold) phases respectively, which are defined by our cooling curve as the ranges $n < 0.5$ cm^{-3}, 0.5 cm^{-3} $< n <$ 5.8 cm^{-3}, and 5.8 cm^{-3} $< n$, respectively. By mass these proportions are reversed to 29%, 23%, and 49%, respectively. From about 100 Myr through the end of the simulation, the distribution of cloud sizes evolves, but the PDF remains relatively unchanged, with 12%, 2%, and 86% of the mass residing in the F, G, and H phases.

We also performed the same simulation, but increased the resolution to 512^2. The conduction coefficient is not changed, so $n_c = 16$. We find similar results overall. In particular, the mass-weighted density PDFs are compared in Panel D of Figure 2.6. These PDFs exhibit no significant differences, confirming the robustness of our results.

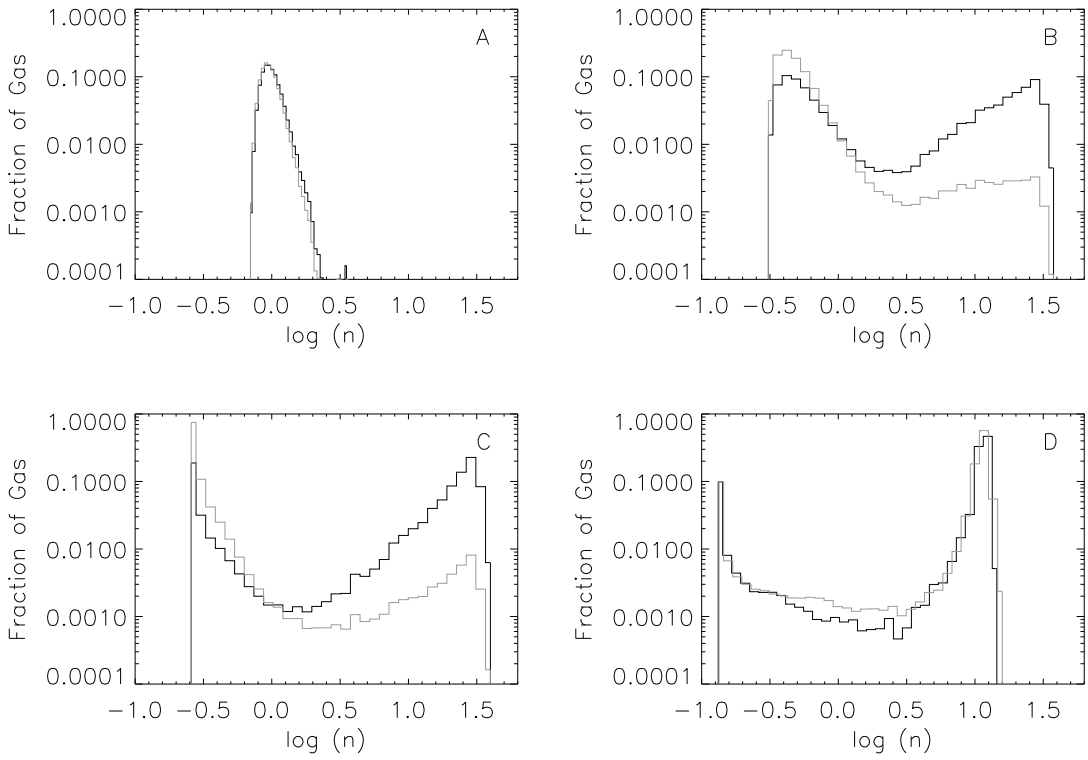

Figure 2.6: Panels A,B and C show the mass (black line) and volume (grey line) density PDFs for TI at the same times as the first three snapshots in Figure 2.3. Panel D compares the mass weighted density PDF for the standard resolution of 256^2 (black line) and 512^2 (grey line) at time 474 Myr.

2.3.3 Thermal Evolution

Alongside the images of density in Figure 2.3 we show scatter plots of n against P for all zones in the grid at the same times. In the initial state, pressure is constant, and t_{sound} at 5 pc ($\sim 1/2$ the length of the fastest-growing TI mode) is shorter than t_{cool} (see Figure 2.4). Towards the low density warm phase, $t_{sound} << t_{cool}$, and gas parcels in regions undergoing rarefaction are able to heat nearly isobarically. Thus, all zones at densities lower than the mean are filled with an intercloud medium that maintains spatially nearly uniform pressure. For gas parcels undergoing compression and net cooling, as $\delta\rho$ becomes large, $t_{cool} << t_{sound}$, so the gas tends to cool towards

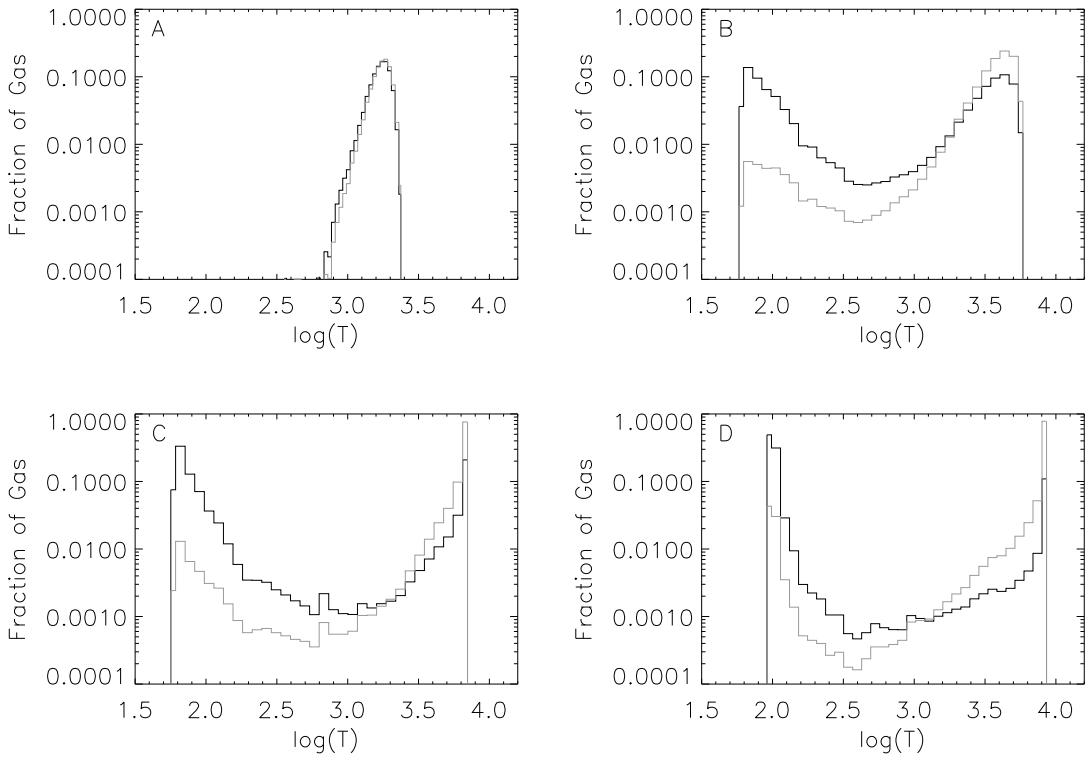

Figure 2.7: Mass (black line) and volume (grey line) temperature PDFs for the snapshots in Figure 2.3 (time increases A-D).

the thermal equilibrium curve at a faster rate than the flow is able to readjust dynamically. After gas parcels reach near thermal equilibrium in the cold phase, they continue to be compressed until pressure equilibrium with the warm medium is re-established. Over time, the average pressure in the simulation box decreases due to radiation from the cold phase.

Because the scatter plots in Figure 2.3 contain a large number of points, many fall in the unstable range, although the actual amount of material there is small. To quantify this, in Figure 2.7 we plot mass-weighted and volume-weighted temperature PDFs at times corresponding to the snapshots in Figure 2.3. As with the density PDF, the distribution is separates into two distinct phases in Panel B at 18 Myr, and remains so for the duration of the simulation.

2.3.4 Kinetic Evolution

Thermal instability is a dynamic process, and a number of recent works have proposed that TI may help contribute to exciting turbulence in the ISM. In Figure 2.8 we plot the mass-weighted velocity dispersions for gas in the F, G, and H phases separately. For all phases, the largest velocities occur during the condensation stage at early times (10-20 Myr), corresponding to about 5 times the e-folding time of the dominant linear instability. The peak velocity is about 0.45 km s^{-1} for the unstable (G) phase, and is $\sim$ 0.3 km s^{-1} for the two stable phases. At later times the velocity dispersion in each phase remains relatively constant, with the largest value (0.35 km s^{-1}) for phase G, next largest (0.25 km s^{-1}) for the warm phase, F, and smallest (0.15 km s^{-1}) for the cold phase, H. The standard deviation of the total velocity dispersion is typically 0.15 km s^{-1}. For comparison, typical sound speeds of the F, G, and H phases are 7-8 km s^{-1} , 1-5 km s^{-1} and 0.6-1 km s^{-1}, respectively. Thus, the mean turbulent velocities are all subsonic.

2.4 MRI Simulations

2.4.1 MRI Physics

In a series of four papers, Balbus & Hawley presented the first linear analysis and numerical simulations of MRI in the context of an astrophysical disk (Balbus & Hawley 1991; Hawley & Balbus 1991, 1992; Balbus & Hawley 1992). The physical basis for the instability is relatively simple, and there are two requirements for the instability to be present: a differentially rotating system with decreasing angular velocity as one moves outward through the disk, and a weak magnetic field (strong magnetic fields have a stabilizing effect). As fluid elements are displaced outward

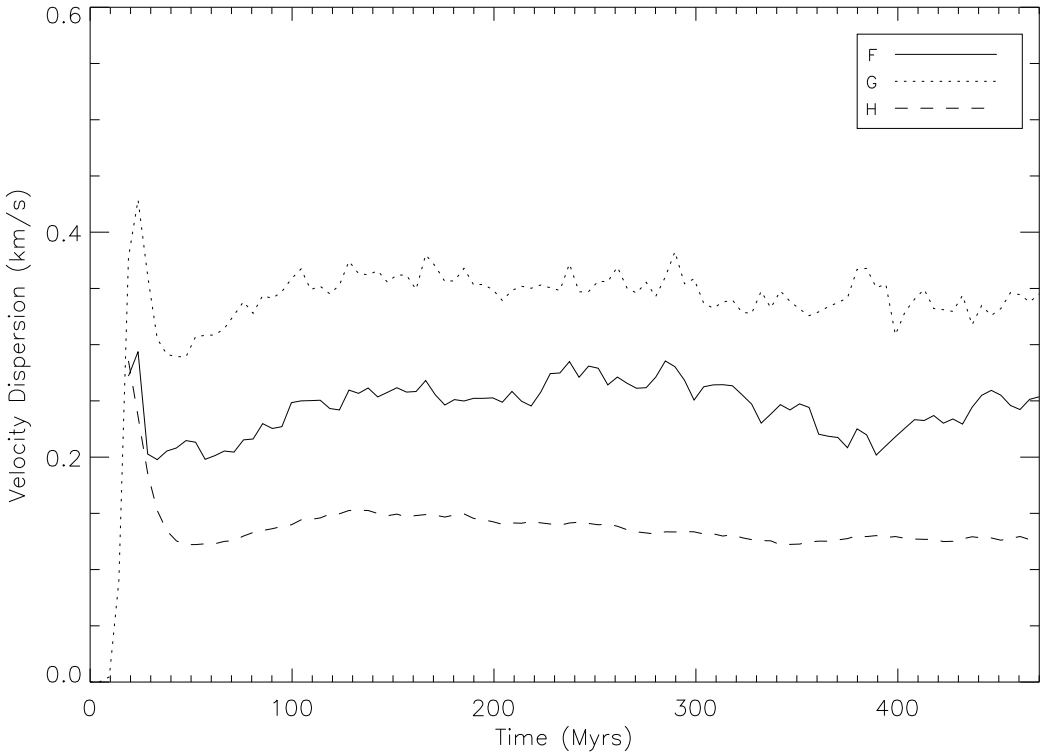

Figure 2.8: Evolution of velocity dispersion $= (v_x^2 + v_z^2)^{1/2}$ in the TI model. Typical velocities for the F (warm), G (unstable), and H (cold) phases are 0.35 km s^{-1}, 0.25 km s^{-1}, and 0.15 km s^{-1}.

(inward) the magnetic field resists shear and tries to keep the fluid moving at its original velocity. Due to these magnetic stresses, fluid elements gain (lose) angular momentum, the centrifugal force becomes too large (small) to maintain equilibrium at the new position, and the fluid element moves farther outward (inward). This leads to the transport of angular momentum outward through the disk.

For a complete linear analysis of the MRI in 2D we refer the reader to Balbus & Hawley (1991). Here we simply summarize the important formulae for axisymmetric modes with wavenumber $\mathbf{k} = k_z \hat{z}$ and $\mathbf{B}_0 = B_0 \hat{z}$. The growth rates are given by

$$\frac{\gamma^2}{\Omega^2} = \nu^2 \left[\frac{2q - \nu^2}{\nu^2 + 2 - q + [4\nu^2 + (2-q)^2]^{1/2})} \right] \tag{2.8}$$

where $\nu \equiv k_z v_{\mathrm{A}z}/\Omega$ in terms of the Alfvén speed $v_{\mathrm{A}z} \equiv B_{0z}(4\pi\rho)^{-1/2}$. The maximum

growth rate occurs when

$$\left(\frac{kv_{\rm Az}}{\Omega}\right)_{peak} = \frac{(4-(2-q)^2)^{1/2}}{2}, \tag{2.9}$$

i.e. $\lambda_{peak} = 4\pi v_{\rm Az}/(\sqrt{3}\Omega)$ for $q = 1$; here the growth rate is $\gamma_{peak} = \Omega q/2 \to \Omega/2$. The highest wavenumber for which axisymmetric MRI exists when $\mathbf{B}_0 = B_0\hat{z}$ is

$$\left(\frac{kv_{\rm Az}}{\Omega}\right)_{max} = \sqrt{2q}. \tag{2.10}$$

We have tested the code without cooling and conduction, and found that it can accurately reproduce the predicted linear growth rates of the MRI. We do not detail the results here; instead we refer the reader to (Hawley & Balbus 1992) for a complete analysis of similar models.

Based on the linear dispersion relation, for sufficiently weak magnetic fields, modes with a range of k_z (and also k_r) may grow. The smallest permissible wavenumber for a simulation is $(k_z)_{min} = 2\pi/L_z$, where L_z is the vertical dimension of the computational box. At late times in 2D axisymmetric simulations (Hawley & Balbus 1992), MRI becomes dominated by a "channel" solution corresponding to the smallest permissible vertical wavenumber, i.e. with flow moving towards the inner regions of the disk on one (vertical) half of the grid, and flow moving towards the outer regions in the other (vertical) half of the grid. This pure "channel flow" is unphysical; for a 3D system it is subject to nonaxisymmetric parasitic instabilities (Goodman & Xu 1994). In 3D non-axisymmetric simulations (e.g. Hawley, Gammie, & Balbus (1995)) the channel solution forms at early times, but later develops into a fully turbulent flow.

The MRI has primarily been studied in the context of accretion disks, but can be important in any differentially rotating disk system provided the magnetic fields are not too strong. In addition to axisymmetric modes, nonaxisymmetric MRI modes can also grow directly (see e.g. Balbus & Hawley (1992) and (Kim & Ostriker 2000)

eqs. 80, 81 for instantaneous growth rates and instability threshold criteria in various limits). The axisymmetric mode with wavelength $\lambda_z \sim 2\mathrm{H}$ is the most difficult to stabilize as B_z increases; from equation (2.10), taking $\Omega = 26$ km s^{-1} kpc^{-1}, $q = 1$, a disk scale height H=150 pc and a uniform density $n = 0.6$ cm^{-3}, MRI will be present provided $B_z < 0.6\ \mu G$. For the Milky Way, this is consistent with the observed solar-neighborhood estimate $|B_z| = 0.37\ \mu$G (Han, Manchester, & Qiao 1999). If a multi-phase system behaves similarly to the corresponding uniform-density medium, then we may expect MRI to be important in the galactic ISM. Here, we explore how MRI development can be affected by strong non-uniformity in the density structure.

2.4.2 Evolutionary Development: TI + MRI Model

To study nonlinear development of the MRI in a nonuniform medium, we first perform a simulation identical to the TI model run described in § 2.3, but now include magnetic fields and sheared rotation. All hydrodynamical variables are initialized as described in § 2.3. The magnetic field is vertical with $\beta = P_{gas}/P_{mag} = 1000$. The rotation rate is set to 26 km s^{-1} kpc^{-1} representative of the local value near the Sun, and we set the shear parameter $q = 1.0$ to describe a flat rotation curve. With these parameters, from equation (2.10), the smallest-scale uniform-density MRI mode that would fit within our $L_z = 100$ pc box has $k_z = 3$ (in units of $2\pi/L_z$).

On the left in Figure 2.9 we show snapshots of number density overlayed with magnetic field lines at three representative times, and on the right we show the corresponding mass-weighted density PDF. The time-scale for development of the MRI is much longer than that of TI, so that the initial development is essentially the same as in the purely hydrodynamical case. During the TI condensation phase

the magnetic field becomes kinked as the filaments condense into small clouds. The remaining random motions of the clouds leads to further distortion of the magnetic field, as can been seen at 237 Myr. The channel solution has clearly taken hold by 474 Myr, and the $k_z = 1$ mode (in units of $2\pi/L_z$) dominates.

Similarly to our analysis of kinetic evolution for the TI model, in Figure 2.10 we plot the velocity dispersion for the F, G, and H phases as a function of time in the TI + MRI model. Initially these are similar to the hydrodynamical case, with all velocities less than 0.5 km s^{-1}. As the channel solution develops the velocity dispersion begins to increase at about 500 Myr, and peaks at the end of the simulation in phase F at approximately 1.5 km s^{-1}. The peak velocity dispersion is about 1.2 km s^{-1} for phase G, and 0.9 km s^{-1} (approximately the sound speed) for phase H, all towards the end of the simulation.

As in the hydrodynamical model, the PDFs for the TI + MRI model are clearly two-phase, with small amounts of gas contained in the unstable regime. At very late times the fully developed channel solution tends to increase the proportion of unstable gas. In Figure 2.11 we plot the mass-weighted temperature PDF of the TI + MRI model 800 Myr, and the same quantity for the TI run at 474 Myr. We do not expect that the PDF for the TI run would evolve significantly if the simulation had been continued to 800 Myr. Evidently, the dynamical flows induced by the MRI can significantly affect the temperature distribution. The larger velocity dispersion and kinked magnetic fields due to the channel solution can compress portions of cold clouds, decreasing the temperature correspondingly. Although still dominated by distinct warm and cold phases, there is also a higher proportion of gas in the unstable regime. For the same model snapshot, Figure 2.12 shows a P/k vs. n scatter plot, overlayed on the equilibrium cooling curve. In the high density regime, cooling times are short, and the gas is not far from equilibrium. At low densities

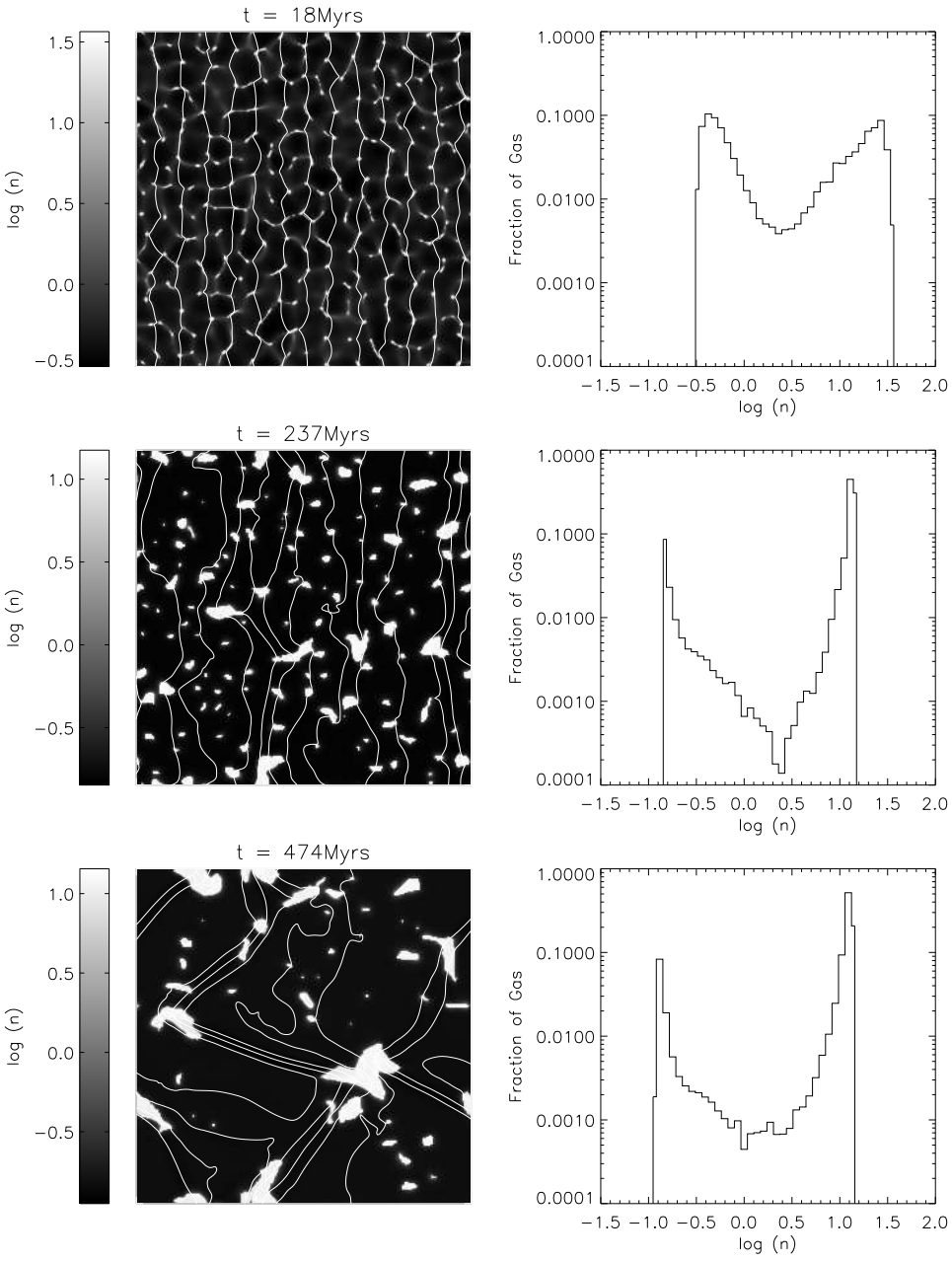

Figure 2.9: Structural evolution of the TI + MRI simulation. *Left*: snapshots of $\log(n)$ at representative times as noted, overlayed with magnetic field lines. *Right*: mass-weighted density PDF at the same times as the snapshots.

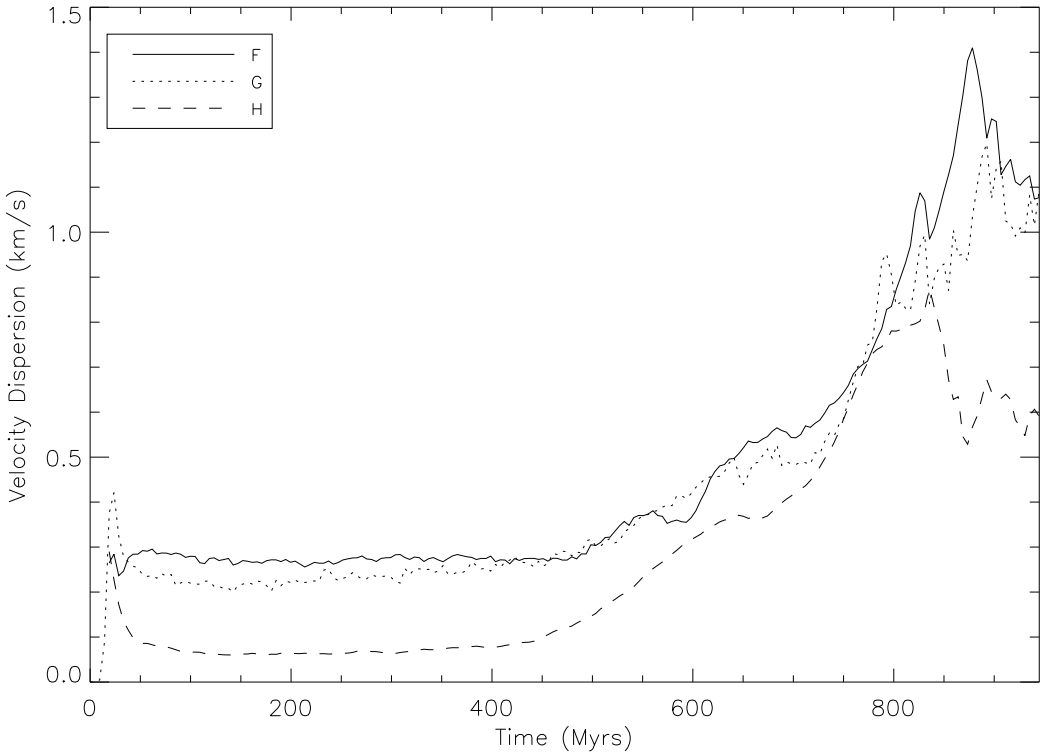

Figure 2.10: Mass-weighted velocity dispersion $= (v_x^2 + v_z^2)^{1/2}$ for TI + MRI model, separated by phase. The initial velocity dispersion is due to the development of TI (see Figure 2.8). After 400 Myr the MRI becomes important, and the channel solution increases the velocity dispersion to as high as 1.4 km s^{-1} towards the end of the simulation.

cooling times are longer, and gas can be found out of thermal equilibrium.

Since the 2D channel solution would break up in a real 3D disk due to parasitic instabilities (Goodman & Xu 1994), we do not expect the late-time effects seen in our models to have direct implications for the temperature distribution in the diffuse ISM. They illustrate, however, the more generic point that spatially-varying rotational shear coupled to magnetic fields can create stresses that force gas away from the stable equilibrium phases. We shall discuss this further, highlighting differences that might be expected for 3D MRI, in § 2.5.

Important questions for assessing MRI development in a cloudy medium are how

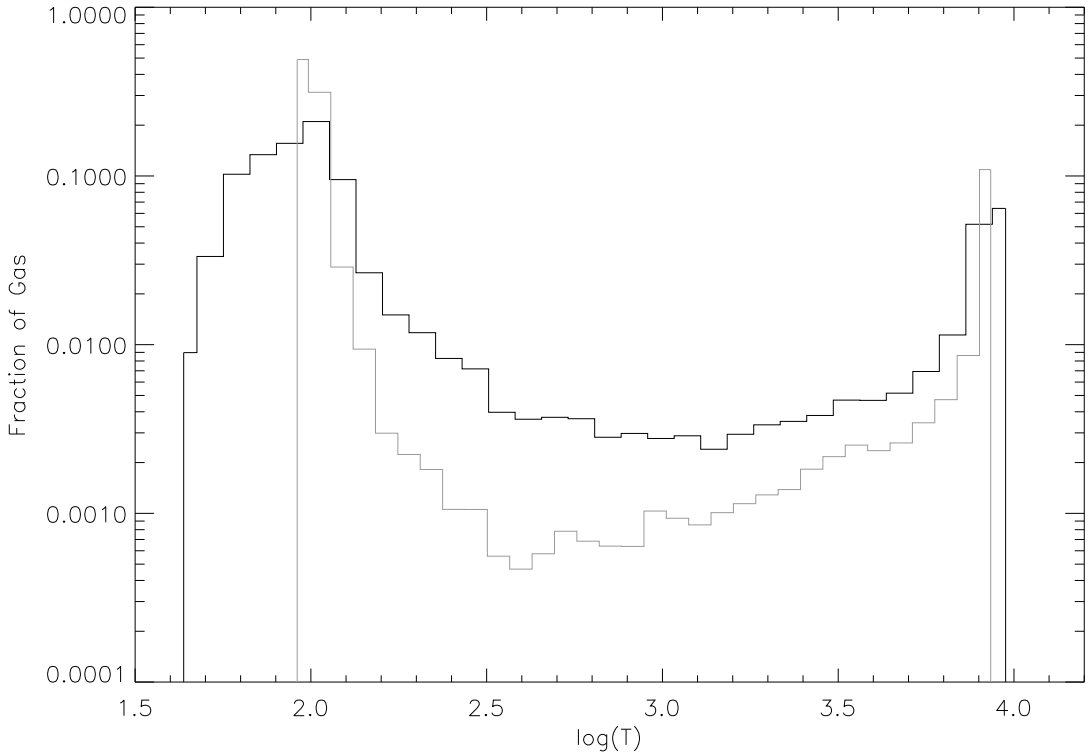

Figure 2.11: Mass-weighted temperature PDF for the TI run at 474 Myr (grey line) and TI + MRI at 800 Myr (black line), after the channel solution has fully developed. The active dynamics of MRI leads to the presence of high density/low temperature gas.

the spatial- and time-scales of the fastest-growing modes differ compared to those in single-phase counterpart systems. We measure MRI mode amplitudes in the simulations by taking the Fourier transform of B_y as a function of time, from which we can calculate the growth rates. The $k = 1, 2$ and 3 mode amplitudes are plotted in Figure 2.13. There is not an obvious linear stage from which we can measure the growth rate, but between 284 and 470 Myr the average $k = 1$ growth rate is about 0.28 Ω, compared to the predicted rate of 0.34 Ω at the average density of the model. At the average density linear theory predicts that the most unstable mode is at $k = 2$, with a growth rate of 0.50 Ω, and the $k = 3$ mode is unstable as well, with a predicted growth rate of 0.41 Ω. Between 284 and 470 Myr we

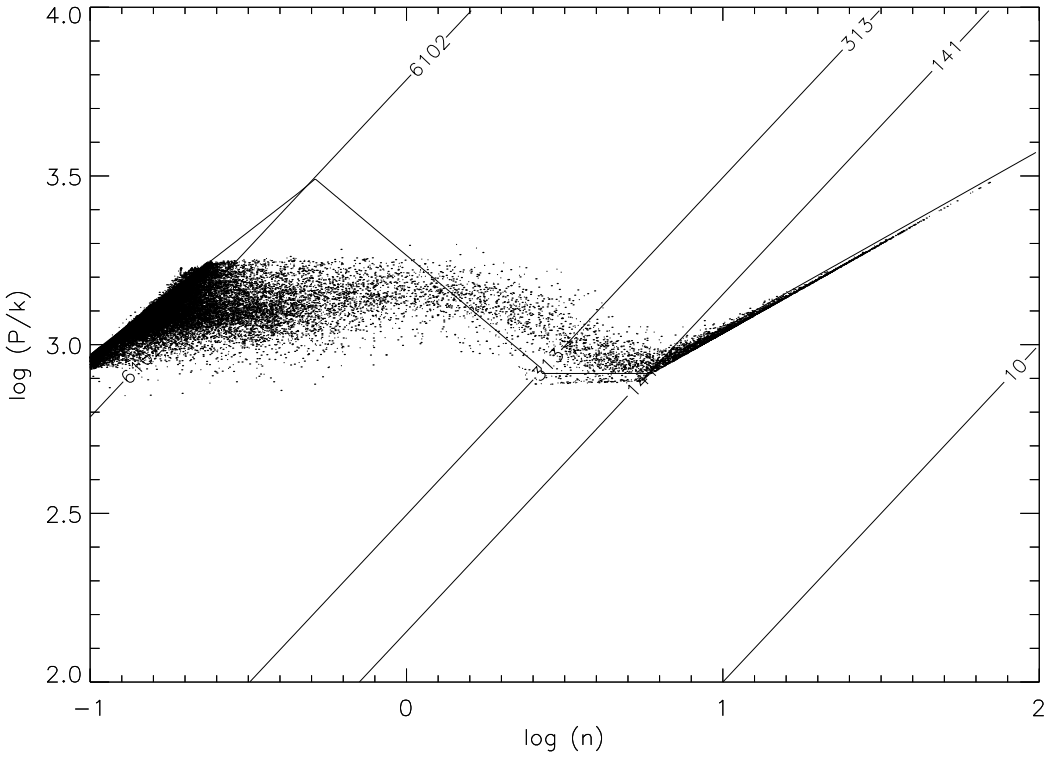

Figure 2.12: Scatter plot of n and P/k at 800 Myr, near the end of the simulation, for the TI + MRI model. Cooling timescales are short for the high density gas, so gas remains near thermal equilibrium for a range of pressures. In the low density regime, cooling time-scales are longer, and there can be significant departures from thermal equilibrium.

measure a mean growth rate for the $k = 2$ and $k = 3$ modes to be 0.12 Ω and 0.18 Ω, respectively. At the density of the warm medium, only the $k = 1$ mode is predicted to be unstable in our simulations, with a growth rate of 0.45 Ω. Thus, growth rates of available modes appear somewhat lower than they would be for a medium at either the mean density or the density of the warm medium. In addition, initial growth does not show the clear dominance of a single fastest growing mode that is evident in comparison adiabatic test simulations for a single-phase medium. However, at late times, the $k = 1$ mode grows to exceed the other low-order modes, similarly to the findings of Hawley & Balbus (1992) for a single-phase medium.

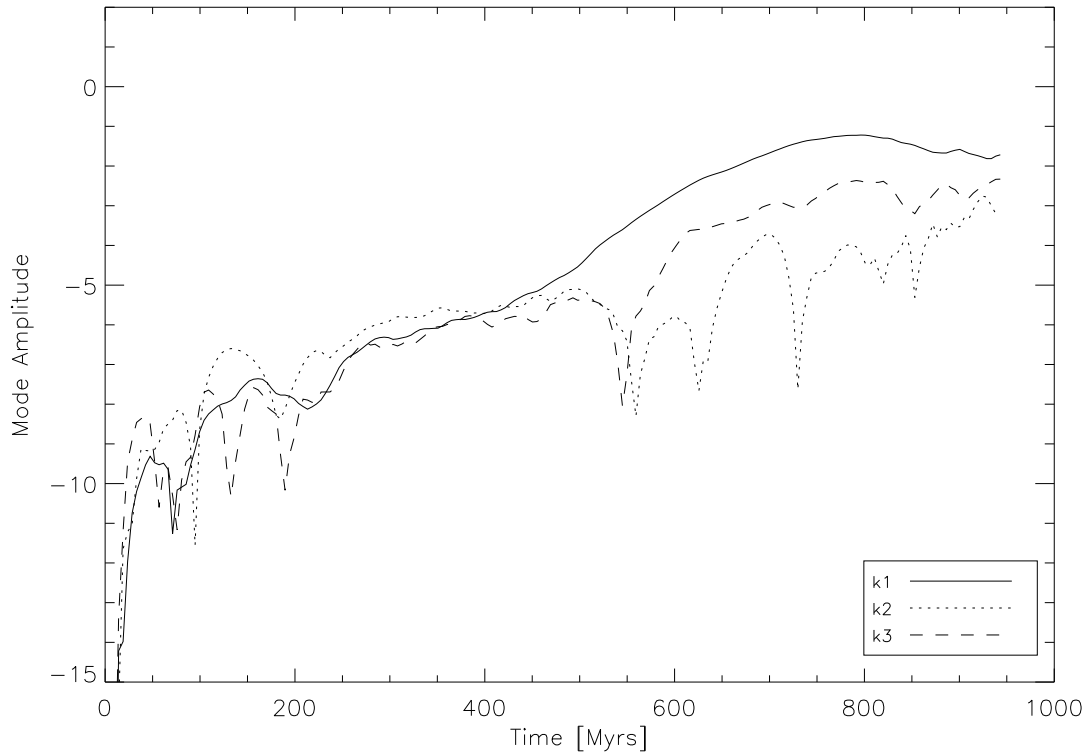

Figure 2.13: Mode amplitudes for B_y in the TI + MRI model. For the first 500 Myr the $k = 1, 2$ and 3 modes are approximately equal in amplitude, but the $k = 1$ mode is dominant after this point.

2.4.3 Evolutionary Development: Cloud + MRI Model

Because the initial MRI growth in the previous model may be strongly affected by lingering dynamical effects of TI, it is of interest to consider MRI development in a medium which contains two distinct phases from the outset. In our next simulation we therefore begin with a two phase medium in approximate equilibrium, rather than developing a two phase medium from thermally unstable gas. We embed 59 high density clouds in a low density ambient medium such that the average density is the same as that of previous TI simulations. To set up the initial conditions allowing for conduction at cloud/intercloud interfaces, we first create "template" cloud profiles by embedding a single high density cold cloud in a low density warm medium and

evolving until a thermally- and dynamically-relaxed state is reached. This profile (density, pressure and velocity) is then copied to randomly chosen locations on the grid, with the condition that cloud centers must be at least 20 zones apart. We initialize the magnetic field after this "cloud embedding" procedure. The simulation is then evolved as the MRI develops.

In Figure 2.14 we show three snapshots from the "cloud + MRI" simulation, along with mass-weighted density PDFs. The MRI takes about 500 Myr until its development begins to become apparent, as can be seen in the poloidal field lines at 464 Myr in Figure 2.14. At 701 Myr many of the clouds have merged and have significant velocities as the MRI channel solution begins to take hold. Initially the mass weighted density PDF shows almost no gas in the unstable range, but as the MRI begins to develop, this phase begins to become populated, and the PDF becomes very similar to those from the TI + MRI simulations.

Perhaps the most interesting results from this "cloud + MRI" simulation are the behavior of the mode amplitudes and growth rates. Initially the clouds contain negligible velocities, and are in what would be a steady state if magnetic fields were not present. We might expect, then, to find "cleaner" MRI growth rates than for the TI + MRI runs. The mode amplitudes for $k = 1, 2$, and 3 are plotted in Figure 2.15. Initially the $k = 2$ mode is dominant and shows approximate linear growth between 300 Myr - 700 Myr, with an average growth rate of 0.34 Ω, compared to the predicted rate 0.50 Ω at the average density. The $k = 1$ mode also shows approximate linear growth with an average rate of 0.47 Ω measured from 450 Myr - 900 Myr, and becomes the dominant mode at around 800 Myr. At the density of the warm medium the theoretical growth rate of the $k = 1$ mode is 0.45 Ω, and at the average density it is 0.34 Ω. The $k = 3$ growth rate, measured between 400 Myr and 800 Myr is 0.33 Ω, which we can compare to the predicted value at the

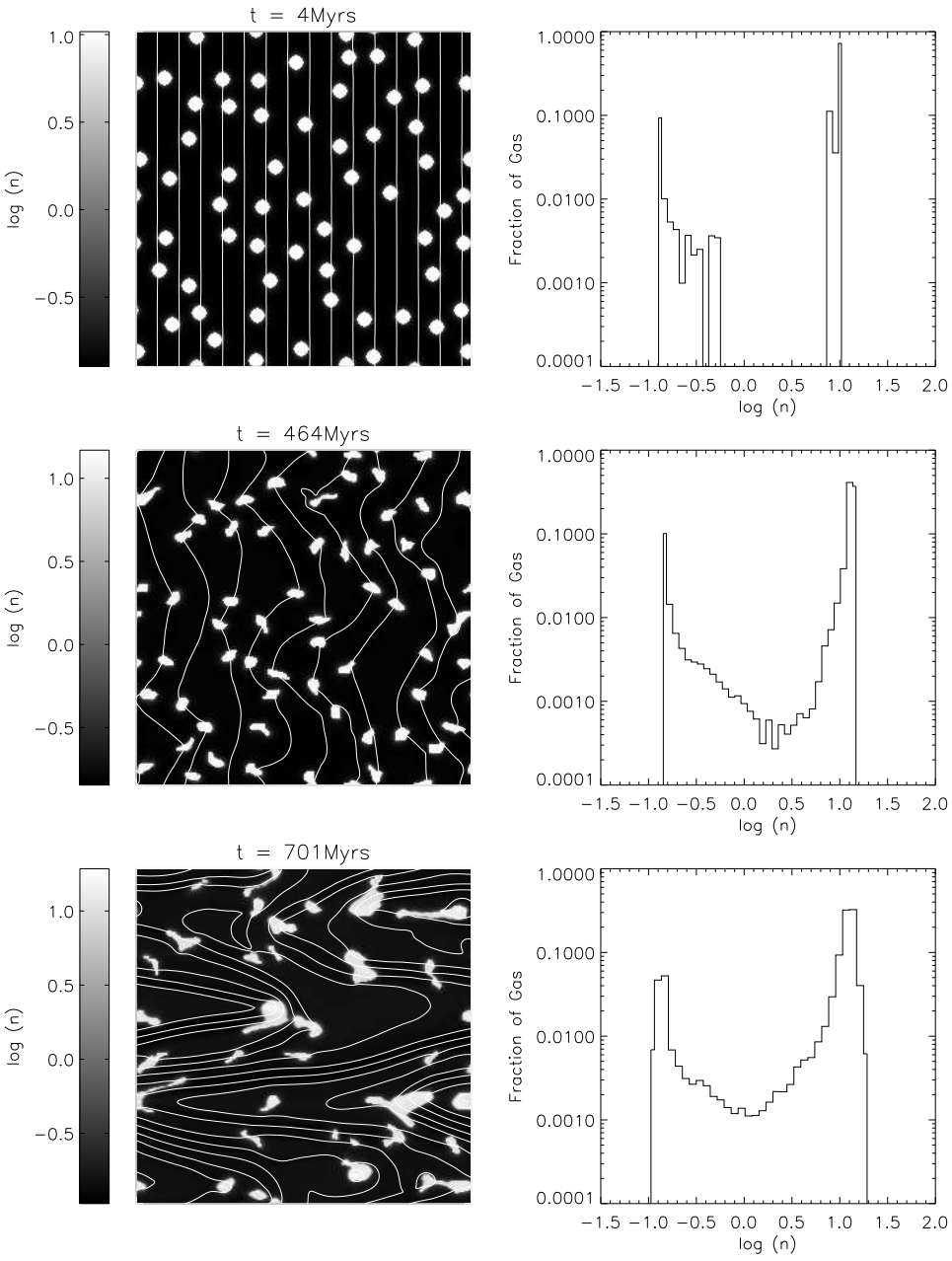

Figure 2.14: Structural evolution of cloud + MRI simulation. *Left*: snapshots of $\log(n)$ at representative times as noted, overlayed with magnetic field lines. *Right*: mass-weighted density PDF at the same times as the snapshots.

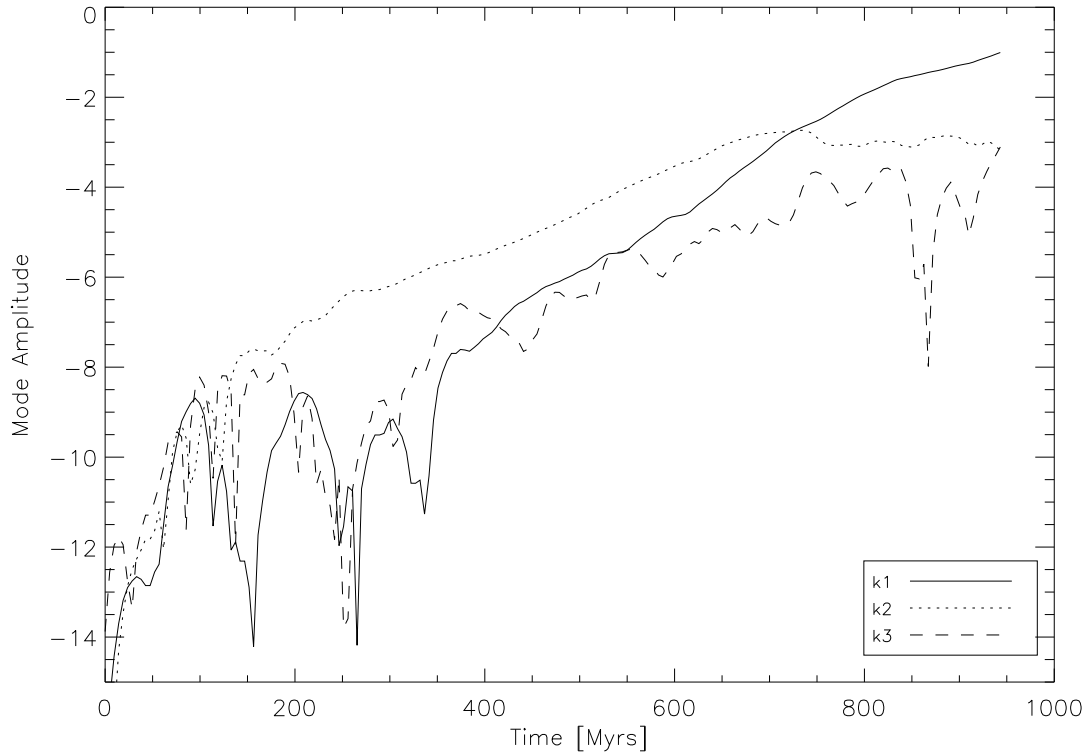

Figure 2.15: Mode amplitudes of B_y in the cloud + MRI simulation. The $k = 2$ mode is initially the largest, but by the end of the simulation the $k = 1$ mode has become dominant.

average density of 0.41 Ω. Thus, similarly to the TI + MRI model, growth rates are slightly lower than they would be in a medium with the same mean density. There is, however, a longer period of dominance by the mode with the fastest expected growth rate.

For comparison we also performed an MRI simulation with cooling and conduction disabled, initially at uniform density and seeded with the velocity and pressure profiles from the initial state of the previous "cloud + MRI" simulation; we also performed zero-conduction, zero-cooling test simulations seeded with random perturbations. The growth rates are in reasonable agreement between these simulations, although the case directly seeded with random perturbations had cleaner growth of mode amplitudes. Most importantly, we find that rather than $k = 2$ predominating

as we found in the "cloud + MRI" simulation, the $k = 3$ mode in the single-phase comparison model is dominant until late time. This suggests that the initial perturbations are strongest at $k = 3$, but the presence of the multi-phase medium in the "cloud + MRI" model significantly inhibits the growth of this mode because the inertial load varies strongly over a wavelength for $k = 3$.

2.4.4 Perspective: Effects of Cloudy Structure

There are a number of ways MRI growth rates and preferred scales could be affected by the influence of a cloudy background density structure, and signs of these effects are evident in our simulations. First, both growth rates and preferred scales are dependent on the Alfvén speed, which is a function of density. The cold, dense clouds will be MRI unstable at small scales compared to the larger preferred scales of the warm, low density, ambient medium. For fixed magnetic field strength, MRI wavelengths are inversely proportional to density. Thus, MRI wavelengths in cold, dense gas will be a few parsecs, while MRI wavelengths in warm, diffuse gas will be several tens of parsecs. Although the MRI wavelengths in dense gas may be smaller than individual cold clouds, permitting initial rapid growth, further development of the small-scale instability is limited by clouds' small radial extent. Long term MRI development must therefore have characteristic wavelengths representative of either the average density conditions or the pervasive low-density warm, intercloud gas. This expectation is indeed consistent with our results. As seen in Figures 2.9 and 2.14, both the diffuse gas and the cold clouds participate together in an overall large-scale flow. The cold clouds frequently are the sites of strong kinks in the magnetic field.

One might also expect the preferred scales for MRI to be affected by cloud spacing. If cloud spacing is small compared to a given wavelength, then the MRI

growth rate might be expected to be similar to that under average density conditions. Thus, if the fastest-growing wavelength at the mean density is large compared to cloud spacing along a field line then this might be expected to be the dominant wavelength. This situation is indeed evident in the second frame (464 Myr) of Figure 2.14, in which the $k = 2$ mode dominates, even though, as described above, the input perturbation spectrum is such that the $k = 3$ mode would dominate if the density were uniform. On the other hand, if fewer, more massive clouds exist, cloud separations will be larger, which could suppress MRI growth at wavelengths shorter than cloud spacings and encourage MRI development on the largest scales. Evidence of this effect can be seen in the third panel (474 Myr) of Figure 2.9.

Finally, if total mass is distributed very unevenly with magnetic flux, then MRI may develop more rapidly and at longer wavelengths in regions where there is a comparatively low inertial load. In simulations (not shown) we have performed which have alternating radial zones of high and low mass loading on field lines (initiated with cold clouds at intersections in a Cartesian grid), we indeed see this effect. Development of MRI in the low-inertia "pure warm" phase is, however, checked when the radially-moving flow collides with the high-inertia cold clouds.

To test whether the growth rate of the smaller-scale k=2 mode (essentially near the lower wavelength limit for behavior as at a single average density) could be enhanced in TI+MRI models, we also performed an additional random TI simulations in which a $k = 2$ perturbation was added shortly after the initial condensation phase. The perturbation was added at about the 20 percent level in v_1. For the first 500 Myr the $k = 2$ mode is strongest with a growth rate of 0.36 Ω. After 500 Myr the k=1 mode, with a growth rate of 0.47 Ω, is again dominant.

Taken together, the simulations of this section show that the development of the MRI in the presence of a cloudy medium has modest differences compared to

the corresponding development in a single phase medium at the average density. The dominant wavelengths are similar to those predicted by linear theory at mean-density conditions, and growth rates are also similar, but slightly smaller. The spacings between clouds affects which among the low-k modes dominates the power during the exponential-growth phase. At very late times the $k_z = 1$ mode is dominant in all simulations, consistent with the ultimate dominance of this channel flow in the single-phase models of Hawley & Balbus (1992).

2.5 Summary and Discussion

Thermal and magnetorotational instabilities may play a major role in determining the physical properties of the diffuse ISM. In regions far from active star formation or a recent supernova explosion, TI and MRI may even be the primary processes driving structure and dynamics in the ISM on scales $\lesssim 100$ pc. The PDFs of gas density and temperature, the characteristic sizes, shapes, and spatial distributions of cloudy structures, and the amplitudes and spectral properties of turbulent velocities and magnetic fields may all be strongly influenced by TI and MRI. In addition, development and saturation of TI and MRI may be strongly interdependent. In this paper, we have initiated a study of these important processes using numerical MHD simulations. The current work focuses on code tests and 2D models using a microphysics implementation appropriate for the atomic ISM. In addition to characterizing the properties of TI and MRI modes in their nonlinear stages, this study lays the groundwork for future 3D simulations which will be used to investigate quasi-steady turbulence.

In the following, we summarize the results presented herein, compare to other recent work, and discuss key issues for future investigation.

1. *Numerical methods:* We have implemented atomic-ISM heating/cooling and thermal-conduction source terms in the energy equation of the ZEUS code (using implicit and explicit updates, respectively). For conditions representing the mean pressure and density in the ISM, we find excellent numerical agreement with the analytic growth rates of thermally-unstable modes for a large range of wavelengths and thermal conductivity coefficients. Based on these tests and confirmation of acceptable results for advection of high-contrast contact discontinuities (warm/cold pressure equilibrium interfaces) on the grid, we adopt a value of $\mathcal{K} = 10^7$ erg cm^{-1} s^{-1} K^{-1} such that the Field length is resolved by 8 (16) zones in (100 pc)^2 simulations with 256^2 (512^2) cells.

Explicit inclusion of conduction is important for suppressing numerically-unresolved TI-driven amplification of grid-scale noise; Koyama & Inutsuka (2003) have also recently highlighted the importance of implementing conduction for simulations of thermally bistable media. In some previous simulations of TI (Kritsuk & Norman 2002a,b) under strongly cooling conditions, conduction was not included; since those simulations began with relatively large-amplitude (5%) perturbations on resolved scales, however, sub-dominant effects from unresolved growth at grid scales in the initial stages of TI would be less noticeable. In other recent work (Vázquez-Semadeni et al. 2003) simulations of TI using spectral algorithms (with explicit diffusive terms in the equations of motions) appear to have difficulty reproducing the analytic growth rates in some circumstances. Conceivably, this may be a sign of numerical diffusion that could tend to produce more gas in thermally-unstable regimes than is realistic, in simulations using these computational methods.

2. *Nonlinear development of TI:* In "pure TI" simulations where we initialize gas at $P/k = 2000$ K cm^{-3} and $n = 1$ cm^{-3} in a (100 pc)^2 box with 0.1% initial pressure perturbations, we find that TI develops at a characteristic length scale

consistent with the predicted fastest-growing mode, ~ 12 pc for our adopted value of $\mathcal{K}$. As seen in other 2D simulations (e.g. Vázquez-Semadeni, Gazol, & Scalo (2000)), the structure initially resembles a "honeycomb" network of cells, and as nonlinear development proceeds, gas condenses into cold, compact clouds at the intersections of filaments. Gas undergoing rarefaction towards the warm phase heats nearly isobarically, because the sound crossing time is short compared to the net heating-cooling time. Gas undergoing compression towards the cold phase initially has isobaric evolution (while density perturbations remain low-amplitude), but then tends first to cool toward the equilibrium curve very rapidly (with an attendant pressure drop), and then dynamically readjusts its density and temperature until the pressure again matches ambient conditions. The time to establish a distinct two-phase structure of well-separated cold clouds within a warm ambient medium (see third panel of Fig. 4) is ~ 20 Myr, or about 10 e-folding times in terms of the linear growth rate. In the subsequent evolution, the cold, dense clouds undergo successive mergers to produce larger structures.

The transition from nearly isobaric to more "isochoric"-like evolution for cold gas during nonlinear stages of condensation was recently emphasized by Burkert & Lin (2000), and snapshots of phase diagrams in Kritsuk & Norman (2002a) show a similar dip in pressure for overdense gas as it cools toward thermal equilibrium. Vázquez-Semadeni et al. (2003) found, similar to our results, that initial perturbations of similar or larger sizes to our dominant TI wavelength require times > 10 Myr to complete the condensation process, even when a much larger (10%) initial perturbations are used. The real level of conduction in the atomic ISM may be lower than the value we adopted (for numerical efficacy), with the fastest-growing TI wavelength a factor ~ 4 smaller than our 12 pc value and the condensation time correspondingly shorter; Sánchez-Salcedo, Vázquez-Semadeni, & Gazol (2002) found

that 3 pc-scale overdensities condense into clouds within 4 Myr. As the turbulent cascade is likely to maintain nonlinear-amplitude entropy perturbations down to sub-pc scales, we expect that the fastest-growing wavelength [3] is likely to dominate when TI occurs under "natural" circumstances, with later mergers producing larger clouds (see also Sánchez-Salcedo, Vázquez-Semadeni, & Gazol (2002)).

3. *Gas phase distributions from TI:* The bimodal density and temperature PDFs in our TI simulations mirror the distinct two-phase structure evident in late-time snapshots. Typical late-time warm-, cold-, and intermediate-temperature mass fractions are 12, 86, and 2%. For a two-phase medium with mean density $\bar{n}$ and cold and warm densities $n_{\rm c}$ and $n_{\rm w}$, the fraction of mass in the cold medium is $f_{\rm c} = (1 - n_{\rm w}/\bar{n})(1 - n_{\rm w}/n_{\rm c})^{-1}$. Provided $n_{\rm c} \gg n_{\rm w}$, the mass fraction in the warm medium is thus $f_{\rm w} \approx n_{\rm w}/\bar{n}$. Since the pressure at late stages of our evolution has dropped near the minimum value of P at which two phases are present, and in thermal equilibrium at this pressure $n_{\rm w} \approx 0.1$ cm^{-3} (with $n_{\rm c} \approx 10$ cm^{-3}), the relative proportions of gas $f_w \approx 0.1, f_c \approx 0.9$ in the cold and warm phases are just as expected (with $\bar{n} = 1$ cm^{-3}).

Findings on density and temperature PDFs from other recent TI simulations are varied. From the 3D simulations of Kritsuk & Norman (2002a,b), the late-time (1.5 Myr) mass fractions are $f_{\rm w} = 0.42$, $f_{\rm c} = 0.44$ in the stable phases and $f_{\rm i} = 0.14$ in the intermediate, unstable regime. Kritsuk and Norman use a somewhat different cooling curve from ours, with $n_{\rm w} = 0.4$ cm^{-3} in thermal equilibrium at the minimum pressure at which two stable phases are available. Since they use $\bar{n} = 1$ cm^{-3}, their result that $f_{\rm w} \approx n_{\rm w}/\bar{n}$ is consistent with expectations for a two-phase medium, while the gas at intermediate temperatures appears to be due to mass exchange with the

[3] From Field (1965), this is essentially the geometric mean of $\lambda_{\rm F}$ and the product of the sound speed and the cooling time.

cold medium (see their discussion).

In the 1D simulations of Sánchez-Salcedo, Vázquez-Semadeni, & Gazol (2002) (and using the same cooling curve and mean density as ours), only a few percent of the gas in their "multiple condensation" runs remains at intermediate densities, similar to our results, and their $f_{\rm w} = 0.3 - 0.4$ at $t \sim 20 - 25$ Myr is similar to our results at comparable (early) times. In the 2D simulations of Gazol et al. (2001) that also include "stellar-like" local heat sources, the late-time mass fractions are $f_{\rm w} = 0.25$, $f_{\rm c} = 0.25$ $f_{\rm i} = 0.50$. It is not clear to what extent this large proportion of gas at intermediate temperatures is sustained by turbulence (via adiabatic expansion/compression and/or shocks heating or cooling gas that would otherwise be in the warm or cold stable phases), versus being maintained by the localized heating turned on when $n > 15{\rm cm}^{-3}$. [4] With 3D MRI simulations in which turbulent driving is "cold", it will be possible to address this important issue.

4. *Turbulent driving by TI:* We find that turbulence produced by "pure TI" has only modest amplitudes, when initiated from "average ISM" pressure and density conditions. For the warm, unstable, and cold phases, respectively, we find typical mass-weighted velocity dispersions of 0.25, 0.35, and 0.15 km s^{-1}. These velocities are all quite subsonic. In simulations starting from thermal equilibrium, Kritsuk & Norman (2002a) similarly find subsonic turbulence ($\mathcal{M}_{rms} \sim 0.3$ at $t < 2$Myr), although when gas is initially very hot, supersonic turbulence can be produced. When they include repeated episodes of strong UV heating Kritsuk & Norman (2002b) find Mach number variations $\mathcal{M}_{rms} \sim 0.2 - 0.6$ between "low" and "high"

[4] Since real star formation is confined to giant molecular clouds rather than occurring in a more distributed fashion in cold atomic clouds, localized stellar heating (and turbulent driving by expanding HII regions) may have much less impact on HI density and temperature PDFs in the real ISM.

states; since their "low state" is dominated by cold gas with $c_s \sim 1$ km s^{-1}, this is consistent with our results for typical turbulent amplitudes. In the simulations of Koyama & Inutsuka (2002) in which warm gas shocks on impact with a low-density, hot ($T = 3 \times 10^5$ K) layer, TI develops near the interface of shocked gas with the hot medium, leading to the formation of cold cloudlets with velocity dispersions of a few km s^{-1}. Although Koyama and Inutsuka attribute this turbulence to the effects of TI, it is possible that other dynamical instabilities associated with the hot/warm interface contribute in driving these motions.

5. *Nonlinear development of axisymmetric MRI:* We have studied the development of axisymmetric MRI under atomic ISM conditions, both with "TI+MRI" models starting from uniform density and pressure ($P/k = 2000\ K$ cm^{-3} and $n = 1$ cm^{-3}), and with "cloud+MRI" models that are initiated with the same uniform pressure and total mass, but start with a population of cold clouds embedded in a warm ambient medium. The magnetic field in both types of models is vertical and initially uniform, with $B^2/8\pi = P/1000$. The peak growth rate of MRI (in a uniform medium) is $\Omega/2$, where Ω is the local angular velocity of the galaxy. Since this growth rate is a factor ~ 40 lower than typical TI growth rates, the early development of the TI+MRI model is the same as in the "pure TI" model. By the time MRI begins to develop (after a few 100 Myr), the TI+MRI model has similar cloud/intercloud structure – except with more variations in cloud size – to the cloud+MRI model. At early times, the density and temperature PDFs are essentially the same as those produced by TI; at late times, however, while the PDFs remain bimodal, the dense gas is distributed over a somewhat larger range of densities and temperatures, due to the dynamics of the "channel flow" solution (see below).

6. *Spatial scales of MRI in a cloudy medium:* In both our TI+MRI and cloud+MRI

simulations, after a few galactic orbital times, the velocity and magnetic fields become dominated by large-scale structures. Since the smallest-scale MRI mode that would fit in our $L_z = 100\,\mathrm{pc}$ box under *uniform-density* conditions has vertical wavenumber $k = 3$ (in units $2\pi/L_z$; i.e. wavelength $\lambda = L_z/3$), and the fastest-growing mode would have $k = 2$, this implies, consistent with expectations, that cloudy density structure in the supporting medium does not grossly alter the character of MRI. We quantify MRI structural development in terms of mode amplitudes of B_y, the azimuthal magnetic field. For the TI+MRI model, the amplitudes of the $k = 1, 2$, and 3 modes are all similar – and motions in the $x - z$ plane continue to be dominated by TI effects, with cloud agglomeration – until $t \sim 400$ Myr, after which the clouds have become highly concentrated and the $k = 1$ MRI mode associated with the "channel solution" (Hawley & Balbus 1992) takes hold. For the cloud+MRI model, on the other hand, the $k = 2$ mode grows first (with clouds remaining small and distributed) and it dominates until ~ 800 Myr, when the channel solution ($k = 1$) begins to take precedence.

These differences show that the spatial distribution of clouds can have a significant effect on selecting which MRI modes are important. If intercloud distances are small compared to its wavelength, the dominant MRI mode is the same as that predicted for uniform-density conditions. If, however, other turbulent processes acting on scales *small* compared to MRI wavelengths (and times small compared to Ω^{-1}) collect the clouds and correspondingly increase their separations, then only MRI modes at scales larger than twice the typical intercloud distance will be able to grow. As a consequence, for MRI to play an important role in the ISM, either the majority of the gas must remain in a warm, diffuse phase, or else if it collects in clouds their separations must not be too large.

It is interesting to relate these constraints to observational inferences of the HI

spatial distribution. From the Heiles & Troland (2003) HI absorption observations that yielded 142 separate cold gas components on 47 lines of sight at $|b| > 10^\circ$, their mean separation would be ~ 40 pc (taking the cold disk semi-thickness ~ 100 pc). The distribution of warm gas is much harder to interpret, but in the limiting situation where it is mainly in overdense clouds[5], and using Heiles and Troland's finding that $\sim 25\%$ of emission components have no associated absorption, the mean distance between clouds would be ~ 30 pc. Intercloud separations similar to these estimates are small enough that vertical MRI modes could be supported; if cloud spacings are appreciably larger, however, they could not be.

7. *Growth rates and saturation amplitudes of MRI:* For the low-k modes that are present in both our TI+MRI and cloud+MRI models, typical growth rates are generally comparable to those for modes of the same wavelength in a medium of the same mean density. For the TI+MRI model, typical growth rates are measured to be 0.28 Ω, 0.12 Ω, and 0.18 Ω for the $k = 1$, 2, and 3 modes, respectively, compared to the rates $\gamma/\Omega = 0.45$, 0.5, and 0.41 that would apply for a uniform medium. For the cloud+MRI model, the exponential MRI growth is "cleaner"; rates are $\gamma/\Omega = 0.47$, 0.34, and 0.33 for $k = 1$, 2, and 3 modes, respectively. The growth rates of smaller-scale ($k = 2, 3$) modes are thus slightly more affected by the presence of cloudy structure than that of the largest-scale ($k = 1$) mode, consistent with expectations.

Although definitive results await 3D simulations, these findings provide support for the possibility that MRI may drive turbulence in the diffuse ISM at amplitudes consistent with observations of HI emission and absorption. From previous 3D simu-

[5]According to Heiles and Troland, of the 60% of the HI that is in warm gas, $> 50\%$ at high latitudes is at lower temperatures than the $T \sim 8000$K required for approximate pressure equilibrium with the cold clouds; since significant underpressures are difficult to achieve, this gas is likely to be in clouds denser than $\bar{n}$.

lations under relatively *uniform* conditions (accomplished by adopting an isothermal equation of state), the velocity dispersions driven by MRI in steady-state were found to be smaller than observed values. In particular, Kim, Ostriker, & Stone (2003) found that the typical 1D turbulent amplitudes are 3 - 4 km s^{-1}, whereas the observed nonthermal contribution to the 1D velocity dispersion for both cold and warm gas amounts to $\sigma_v \sim 7$ km s^{-1} (Heiles & Troland 2003). Thus, for a *single phase medium*, MRI-driven turbulent velocity amplitudes in steady state – which are determined by a balance between excitation and dissipation – fall a factor ~ 2 short of explaining observations.

Since our present cloudy-medium models show growth rates quite comparable to those in a one-phase medium, the key question is therefore whether MRI dissipation rates are reduced in a cloudy medium, and if so, whether the reduction can yield a factor two increase in σ_v. To see that a quantitative effect at this level is not unreasonable, consider the comparison to an idealized system of $\mathcal{N}_{cl} \equiv \ell^{-3}$ clouds per unit volume having individual radii r, internal density relative to the mean value $n_{cl}/\bar{n}$, and RMS relative velocity dispersion σ_v. With turbulent energy driving and dissipation rates $\dot{\mathcal{E}}_{in}$ and $\sim \sigma_v^2/t_{coll}$, where the collision time $t_{coll} = (4\sqrt{\pi} r^2 \mathcal{N}_{cl} \sigma_v)^{-1}$, σ_v in steady state is an order-unity factor times $(\dot{\mathcal{E}}_{in}\ell)^{1/3}(n_{cl}/\bar{n})^{2/9}$. For this idealized situation, concentrating material into clouds with $n_{cl}/\bar{n} \sim 30$ (similar to cold ISM clouds) would indeed increase σ_v by a factor two compared to the case with near-uniform conditions, $n_{cl}/\bar{n} \sim 1$. With 3D simulations, it will be possible to test whether a similar scaling behavior holds for the saturated state of MRI-driven turbulence in cloudy vs. single-phase ISM models.

Chapter 3

Saturated-State Turbulence and Structure from Thermal and Magnetorotational Instability in the ISM: Three-Dimensional Numerical Simulations

Abstract

This paper reports on three-dimensional numerical simulations of dynamics and thermodynamics in the diffuse interstellar medium (ISM). Our models are local, account for sheared galactic rotation, magnetic fields, and realistic cooling, and resolve scales $\approx 1 - 200$ pc. This combination permits the study of quasi-steady-state turbulence in a cloudy medium representing the warm/cold atomic ISM. Turbulence is driven by the magnetorotational instability (MRI); our models are the first to study the saturated state of MRI under strongly inhomogeneous conditions, with

cloud/intercloud density and temperature contrasts ~ 100. For volume-averaged densities $\bar{n} = 0.25 - 4$ cm^{-3}, the mean saturated-state velocity dispersion ranges from $8 - 1$ km s^{-1}, with a scaling $\delta v \propto \bar{n}^{-0.77}$. The MRI is therefore likely quite important in driving turbulence in low-density regions of the ISM, both away from the midplane in the inner Galaxy (as observed at high latitudes), and throughout the far outer Galaxy (where the mean density drops and the disk flares). The MRI may even be key to suppressing star formation at large radii in spiral galaxies, where the pressure can be high enough that without MRI-driven turbulence, a gravitationally-unstable cold layer would form. As expected, we find that turbulence affects the thermal structure of the ISM. In all our simulations, the fraction of thermally-unstable gas increases as the MRI develops, and in the saturated state is largest in high-δv models. The mass fractions of warm-stable and unstable gas are typically comparable, in agreement with observations. While inclusion of resistive dissipation of magnetic fields could enhance the amount of thermally-unstable gas compared to current models, our present results indicate that even high levels of turbulence cannot wipe out the signature of thermal instability, and that a shift to a "phase continuum" description is probably unwarranted. Instead, we find that temperature and density PDFs are broadened (and include extreme departures from equilibrium), but retain the bimodal character of the classical two-phase description. Our presentation also includes results on the distribution of clump masses (the mass spectrum peaks at ~ 100 M$_\odot$), comparisons of saturated-state MRI scalings with single-phase simulation results (we find $\langle B^2 \rangle$ is independent of $\bar{n}$), and examples of synthetic HI line profile maps (showing that physical clumps are not easily distinguished in velocity components, and vice versa).

3.1 Introduction

Far from the energizing regions of star formation in the Milky Way and other galaxies, the interstellar medium (ISM) is still roiling with activity, and rife with structure. Both the microphysical properties and turbulent activity have been increasingly well characterized by Galactic and extragalactic radio observations. In particular, recent high-resolution Galactic emission surveys in the 21 cm hydrogen line (e.g. McClure-Griffiths et al. (2001); Taylor et al. (2003)), combined with Galactic absorption surveys (e.g. Heiles & Troland (2003); Mohan, Dwarakanath, & Srinivasan (2004)), and mapping of face-on external galaxies (e.g. Dickey et al. (1990); van Zee & Bryant (1999)), have begun to provide a wealth of thermal and kinematic information about the atomic ISM component, which comprises the majority of the total ISM mass in most spiral galaxies. Analysis of this data promises to yield a detailed empirical description of the atomic gas, which is known to consist of both warm and cold components, and to be strongly turbulent (e.g. Dickey & Lockman (1990)).

As observations of the ISM advance, there is a need on the theoretical side for increasingly sophisticated ISM modeling. With modern computational tools, it is possible to pursue time-dependent hydrodynamic models which incorporate many physical processes. This numerical modeling can extend established "classical" results for simplified systems into more realistic regimes, and test conceptual proposals for the behavior of complex systems in a rigorous fashion. The goal of detailed ISM modeling, of course, is not sophistication for its own sake, but to gain understanding about how different "elemental" processes interact, to ascertain which among many contributing processes are most important, and to aid in interpreting and developing reliable physical diagnostics from observations.

Broadly, the presence of structure in the atomic ISM can be easily understood as

a consequence of the bistable thermal equilibrium curve over a range of pressures, including those typical of the ISM. Since the temperatures of the two stable thermal equilibria differ by a factor of ~ 100 (at fixed pressure), the "classical" expectation based on the principle of pressure equilibrium is a system of cold, dense clouds embedded in a much more diffuse warm intercloud medium (Field, Goldsmith, & Habing 1969). Thermal instability (TI) tends to move gas parcels at intermediate temperatures into one of the stable phases (Field 1965). Clouds are initially expected to condense at preferred scales where conduction limits local thermal gradients. While these basic processes are certainly involved in establishing the ISM's structure, the end result is a complex product of evolution and interactions with other physical processes, leaving many open questions. For example, how do the agglomerations and disruptions of cold clouds depend on the turbulence properties, and how does this affect the mass function of condensations that results?

Many processes have been proposed that can produce turbulence in the ISM (see e.g. Mac Low & Klessen. (2004); Elmegreen & Scalo (2004) for recent reviews). Traditionally, turbulence is thought to be driven primarily by supernovae (McKee & Ostriker 1977) (and, to a lesser extent, expanding HII regions), because the total kinetic energy they are able to supply could be sufficient to offset the turbulent dissipation in the Milky Way's diffuse ISM (Spitzer 1978, Ch. 11). Supernovae are certainly the primary source of turbulence near regions of high-mass star formation. However, it is not clear how effectively this energy can in fact be shared with the bulk of the ISM, so other sources may be (or combine to be) of comparable importance. Indeed, observations indicate that the levels of turbulence are not strongly correlated with spiral arms (where star formation is enhanced), and are just as large in outer galaxies (where overall star formation rates are low) as in inner regions (van Zee & Bryant 1999; Petric & Rupen 2001). Moreover, recent 3D simulations (Korpi et

al. 1999; de Avillez & Breitschwerdt 2005) in which turbulence is driven solely by supernovae find that velocity dispersions are significantly lower in cold gas than in warm gas, inconsistent with observations (Heiles & Troland 2003).

An obvious non-stellar energy source for the ISM is galactic rotation. Wherever the angular velocity decreases outward and magnetic fields are present, the powerful magnetorotational instability (MRI) is expected to tap this rotation and drive large-amplitude ISM turbulence (Sellwood & Balbus 1999; Kim, Ostriker, & Stone 2003; Dziourkevitch , Elstner, & Rüdiger 2004). Detailed development of MRI has primarily been studied in adiabatic or isothermal gas, where turbulent velocities and Alfvén speeds grow into rough equipartition at slightly subsonic levels (e.g. Hawley, Gammie, & Balbus (1995, 1996) hereafter HGB1, HGB2)). Adiabatic and isothermal models, however, are essentially single phase, with only small variations in density and temperature. How do turbulent saturation levels differ in a medium where there are huge variations in conditions, such that subsonic speeds with respect to the diffuse gas are highly supersonic with respect to the dense gas?

In the real ISM, dynamics must affect thermodynamics, and vice versa. The turbulent power input is significant, and both (irreversible) dissipative heating and (reversible) PdV heating and cooling can alter distributions of temperatures compared to the narrow spikes at warm and cold equilibria that would otherwise occur. In turn, thermodynamics potentially can affect loss rates of turbulence: supersonic compressions are dissipative while subsonic compressions are not, and dissipation of magnetic energy by reconnection depends on local conditions of density and temperature. Cloudy structure also changes effective flow "collision" times, as well as field line geometry. Indeed, recent observational evidence has shown that the fraction of unstable gas in the ISM may be significant; Heiles & Troland (2003) found that at high latitudes, about half the warm neutral medium (WNM) lies at thermally

unstable temperatures between 500-5000 K. Numerical models which include effects of star formation (Rosen & Bregman 1995; Korpi et al. 1999; de Avillez 2000; Wada, Spaans, & Kim 2000; Gazol et al. 2001; Wada & Norman 2001a; Wada 2001b; Mac Low et al. 2005; Slyz et al. 2005) find both turbulence and significant fractions of unstable gas, although it is not clear how much the temperature distributions are affected by the direct heat inputs in the star formation feedback algorithms of these models.

Recent simulations have addressed nonlinear evolution, in 2D and 3D, of TI in the ISM without "stellar" energy inputs (Hennebelle & Pérault 1999; Burkert & Lin 2000; Vázquez-Semadeni, Gazol, & Scalo 2000; Sánchez-Salcedo, Vázquez-Semadeni, & Gazol 2002; Kritsuk & Norman 2002a; Vázquez-Semadeni et al. 2003; Audit & Hennebelle 2005; Kritsuk & Norman 2004), and there have also been many numerical studies, in 2D and 3D, of the MRI in single-phase gas. In previous work, we performed 2D studies of TI and MRI in combination (Piontek & Ostriker (2004), hereafter Paper I). Paper I showed that MRI growth rates in a two-phase medium are comparable to those in a single-phase medium with the same $\bar{\rho}$ and $\bar{\mathbf{B}}$, provided that the cloud separation along field lines does not exceed half of the fastest-growing MRI wavelength (typically $\sim 100\,\mathrm{pc}$). Although there have been suggestions that TI itself could be a significant source of turbulence, "pure TI" models we performed show that for pressures comparable to mean galactic values (i.e. away from HII regions or recent supernovae), velocity dispersions are only a few tenths of a km s^{-1}. In our 2D simulations, the MRI leads to large-amplitude velocities and magnetic fields, but as for single-phase 2D models, late time behavior is dominated by the "channel flow;" quasi-steady turbulence is possible only for 3D flows. The present work constitutes the extension of Paper I to 3D, in order to study the saturated state of MRI in the presence of a two-phase medium. As we shall describe, we have performed a variety

of simulations, with parameters covering a range of conditions characteristic of the atomic ISM.

The plan of this paper is as follows: In §2 we briefly describe the numerical method, and the initializations for the various models we have performed. In §3 we present the results of our simulations in terms of the models' physical structure, thermodynamic distributions, and turbulent states (in velocities and magnetic fields), as well as exhibiting sample synthetic observations based on our simulated data. We summarize, discuss the astronomical implications of our results, and compare to previous work in §4.

3.2 Numerical Methods and Model Parameters

The numerical methods utilized for the present study are essentially the same as those of Paper I, but extended from 2D to 3D. For a complete description of the numerical method and tests, please see that work. Here, we briefly summarize the salient points.

We integrate the time-dependent equations of magnetohydrodynamics with a version of the ZEUS code (Stone & Norman 1992a,b). ZEUS uses a time-explicit, operator-split, finite difference method for solving the MHD equations on a staggered mesh, capturing shocks via an artificial viscosity. Velocities and magnetic field vectors are face-centered, while energy and mass density are volume-centered. ZEUS employs the CT and MOC algorithms (Evans & Hawley 1988; Hawley & Stone 1995) to maintain $\nabla \cdot \mathbf{B} = 0$ and ensure accurate propagation of Alfvén waves.

We have implemented volumetric heating and cooling terms, and a thermal conduction term. The update due to net cooling is solved implicitly using Newton-Raphson iteration. For a given hydrodynamical time step, the change in tempera-

ture in each zone is limited to be less than 25%. This is a somewhat larger fraction than the 10% limit used in Paper I, which allows us to run with larger time steps needed to make 3D calculations practical. Tests have shown that relaxing this constraint does not affect cloud structure; ΔT exceeds 10% only in a very small fraction of zones. The conduction term is solved explicitly using a seven point stencil for the second derivative of temperature. We also model the differential rotation of the background flow and the variation of the stellar/dark matter gravitational potential in the local limit with $x \equiv R - R_0 \ll R_0$, where R_0 is the galactocentric radius of the center of our computational domain. The equations we solve are therefore:

$$\frac{\partial \rho}{\partial t} + \boldsymbol{\nabla} \cdot (\rho \mathbf{v}) = 0 \tag{3.1}$$

$$\frac{\partial \mathbf{v}}{\partial t} + \mathbf{v} \cdot \boldsymbol{\nabla} \mathbf{v} = -\frac{\boldsymbol{\nabla} P}{\rho} + \frac{1}{4\pi\rho}(\boldsymbol{\nabla} \times \mathbf{B}) \times \mathbf{B} + 2q\Omega^2 x \hat{x} - 2\boldsymbol{\Omega} \times \mathbf{v} \tag{3.2}$$

$$\frac{\partial \mathcal{E}}{\partial t} + \mathbf{v} \cdot \boldsymbol{\nabla} \mathcal{E} = -(\mathcal{E} + P)\boldsymbol{\nabla} \cdot \mathbf{v} - \rho\mathcal{L} + \boldsymbol{\nabla} \cdot (\mathcal{K} \boldsymbol{\nabla} T) \tag{3.3}$$

$$\frac{\partial \mathbf{B}}{\partial t} = \boldsymbol{\nabla} \times (\mathbf{v} \times \mathbf{B}) \tag{3.4}$$

All symbols have their usual meanings. The net cooling per unit mass is given by $\mathcal{L} = \rho\Lambda(\rho, T) - \Gamma$. We adopt the simple atomic ISM heating and cooling prescriptions of Sánchez-Salcedo, Vázquez-Semadeni, & Gazol (2002), in which the cooling function, $\Lambda(\rho, T)$, is a piecewise power-law fit to the detailed models of Wolfire et al. (1995). The heating rate, Γ, is taken to be constant at 0.015 erg s^{-1}g^{-1}. In the tidal potential term of equation (3.2), $q \equiv -d \ln \Omega / d \ln R$ is the local dimensionless shear parameter. We adopt q equal to unity, to model a flat rotation curve in which the angular velocity $\Omega \propto R^{-1}$.

The present set of simulations is 3D, with the computational domain representing a cubic sector of the ISM in the radial-azimuthal-vertical ($x - y - z$) domain. We employ shearing-periodic boundary conditions in the $\hat{x}$-direction (Hawley & Balbus 1992; Hawley, Gammie, & Balbus 1995), and periodic boundary conditions in the $\hat{y}$- and $\hat{z}$-directions, as originally implemented in ZEUS by Stone et al. (1996). This framework allows us to incorporate realistic galactic shear, while avoiding numerical artifacts associated with simpler boundary conditions. We have previously used an isothermal version of the same code to study larger-scale galactic ISM problems (Kim, Ostriker, & Stone 2002, 2003).

We have parallelized the code with MPI to run on distributed-memory platforms. We perform a standard domain decomposition in $\hat{x}$, so that each processor works on a slab of the domain. Decomposing in $\hat{y}$ and $\hat{z}$ as well would reduce message-passing time when running on more than eight processors, but for gigabit networks and faster the compute time exceeds the message-passing time for 128 or fewer processors in any case. Thus, for our moderate problem sizes, the additional effort that would be required to parallelize the shearing-periodic boundary conditions is not merited.

Our standard resolution is 128^3 zones. To confirm numerical convergence, we also performed one simulation at 256^3 and found the results to be similar to the standard resolution run. Our box is 200pc on each side, giving a resolution of about 0.8 pc in our 256^3 run, and about 1.6 pc in our 128^3 resolution runs. We set the conduction coefficient to $\mathcal{K} = 1.03 \times 10^7$ergs cm^{-1} K^{-1} s^{-1}. This level of conduction was chosen to allow us to resolve all modes of TI that are present (see Paper I). In our fiducial model, the initial state of the gas is constant density, constant pressure with conditions comparable to mean values in the solar neighborhood; $n = 1.0$ cm^{-3} and $P_0/k = 2000$ K cm^{-3}. The corresponding initial isother-

mal sound speed is $c_s = 3.6$ km s^{-1}. The initial magnetic field strength satisfies $\beta = P_{gas}/P_{mag} = 100$, corresponding to $B = 0.26$ μG in the vertical ($\hat{z}$) direction. This is our "standard" run. Additional simulations are performed with varying mean densities of $n = 0.25, 0.67, 1.5$ and 4.0 cm^{-3}, as well as one with lower magnetic field strength, $\beta = P_{gas}/P_{mag} = 1000$. We also performed an isothermal simulation with $c_s = 2.8$ km s^{-1} and $n = 1.0$ cm^{-3}. This value of c_s was chosen so that the initial thermal pressure matches the mean late-time pressure in our cooling models. Finally, we also performed a simulation with heating and cooling turned on that was initialized from the saturated-state, turbulent isothermal model. For all our models we adopt the galactic orbital period at the solar radius, 2.5×10^8 yr, to normalize the shear rate.

Since increasing or decreasing the mean density by a large factor relative to $n = 1$ cm^{-3} would initialize the gas in a thermally *stable* state, some of our simulations are initialized with a medium already in a two-phase state, rather than with a uniform density. For these models, spherical clouds of cold dense gas are inserted into a warm ambient medium at random locations. The number of clouds is adjusted so that the average density of the cloudy medium is at the desired level. A similar simulation was performed in Paper I, which allowed us to study the growth rates of the MRI in an initially quiescent cloudy medium. Since the 2D simulations of Paper I were axisymmetric there was no evolution of the model until MRI modes began to grow. This allowed us to compare directly the MRI growth rates of an adiabatic run with a two-phase run, illustrating the effect of cloud size and distribution on the growth rates. In the present 3D simulations, however, the evolution is rapid because the symmetry in the azimuthal direction is broken. Individual clouds are sheared out relatively quickly, and also begin to merge with nearby clouds. Nevertheless, because MRI-driven turbulence eventually dominates both the initially-thermally-

unstable and initially-two-phase models, at late times the two are indistinguishable.

On top of the initial conditions given above, we add pressure perturbations with a white noise spectrum at the 0.1% level to seed the TI and MRI. In the next section, we describe results from our standard run in detail, and comment on differences with the other runs as is appropriate.

3.3 Results

3.3.1 Overall Evolution

Figures 3.1 and 3.2 are volume renderings of the 3D density data cube, from our run with fiducial parameters, and resolution 256^3, at $t = 1.0$ and 9.0 orbits. The early development of both TI and MRI in the present set of 3D simulations is quite similar to the development previously described for 2D simulations in Paper I. Initially the gas is thermally unstable. The cooling time scale is much shorter than the orbital time scale, and the gas quickly separates into many small, cold clouds embedded in a warm ambient medium. This phase of the evolution lasts about 20 Myr, which is comparable to the 2D simulations of Paper I. The typical size scale of the clouds is about 5 pc, consistent with expectations for the fastest growing modes at the adopted level of conductivity. The size scale of the clouds is still fairly close to its initial distribution in Figure 3.1 at $t = 1.0$ orbits.

After the initial condensation phase of TI is complete, large scale galactic shear begins to drive the evolution. Already at $t = 2.0$ orbits, the clouds have become elongated in the $\hat{y}$ direction. During the first few orbits interactions take place between nearby clouds, which typically lead to mergers, increasing the typical size scale significantly. At about $t = 4.0$ orbits ($= 10^9$yrs) the modes of the MRI have grown significantly and now begin to dominate the evolution of the model. The

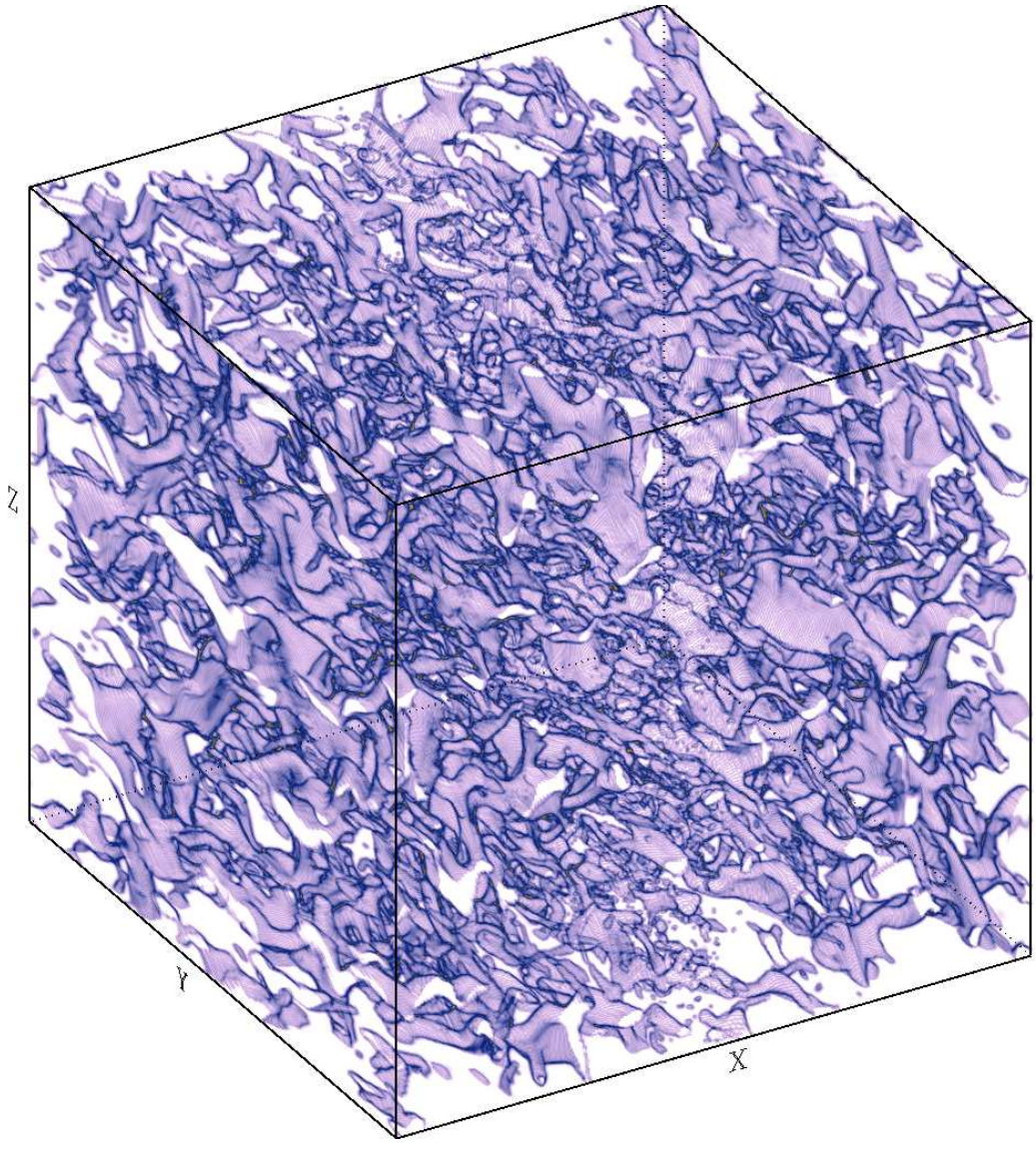

Figure 3.1: Volume rendering of density for the standard run at t=1.0 orbits. The "y" direction is azimuthal in this model, and the "x" direction is radial. Most of the mass is in the cold phase, while most of the volume is occupied by the warm phase.

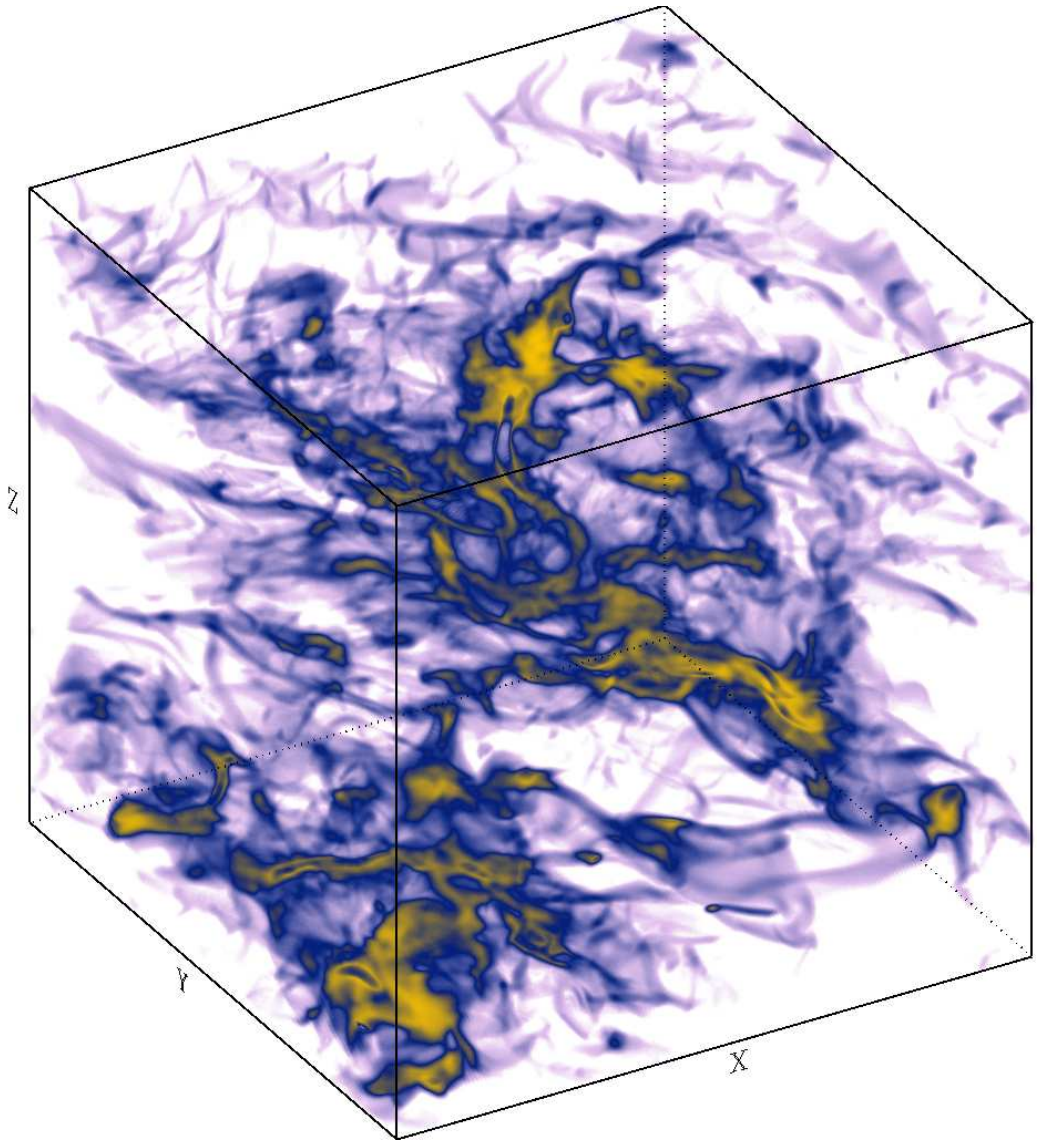

Figure 3.2: Volume rendering of density for the standard run at t=9.0 orbits. Turbulence due to the MRI has forced gas to higher densities, as well as increased the mass fraction of the unstable phase. Many filamentary structures are present.

simulation becomes fully turbulent, drastically altering the dynamics compared to the axisymmetric model of Paper I. Shear from the MRI with velocities in all directions, combined with galactic shear with velocities in the azimuthal direction, leads to repeated disruptive interactions and collisions between clouds. Clouds merge into an interconnected network, with individual entities existing for only short periods of time. It is difficult to convey the dynamical nature of the simulations to the reader using only snapshots in time; the animation associated with Figures 3.1-3.2 shows this much more clearly.

While the structure remains highly dynamic, a quasi-equilibrium saturated state is established by $t \sim 5$ orbits, and the statistical properties of the gas remain relatively constant throughout the latter half of the simulation (up to t=10 orbits). The approach to a quasi-steady turbulent state in these models is generally similar to the results for isothermal or adiabatic single phase models (e.g. HGB1, HGB2). In the remainder of §3, we discuss details of evolution and quasi-steady properties, similarities and differences from single-phase models, and dependencies on model parameters.

3.3.2 Density Structure

The density probability distribution functions (PDFs) from our standard run (at 128^3) are shown in Figure 3.3 at $t = 1, 2.5, 5.0$, and 9 orbits. We show both mass-weighted and volume-weighted density PDFs in Panels A-D, and compare the PDFs of the 128^3 and 256^3 runs in Panel D. Similar to our results in Paper I, we find that by mass, most of the gas is in the cold phase, while the warm phase occupies most of the volume. After the initial development of TI has completed, at $t = 1.0$ orbits, the mass fraction of gas in the warm (F), unstable (G), and cold (H) phases is 14%, 5%, and 80%, respectively. By volume, 83%, 9%, and 8% of the gas resides in the

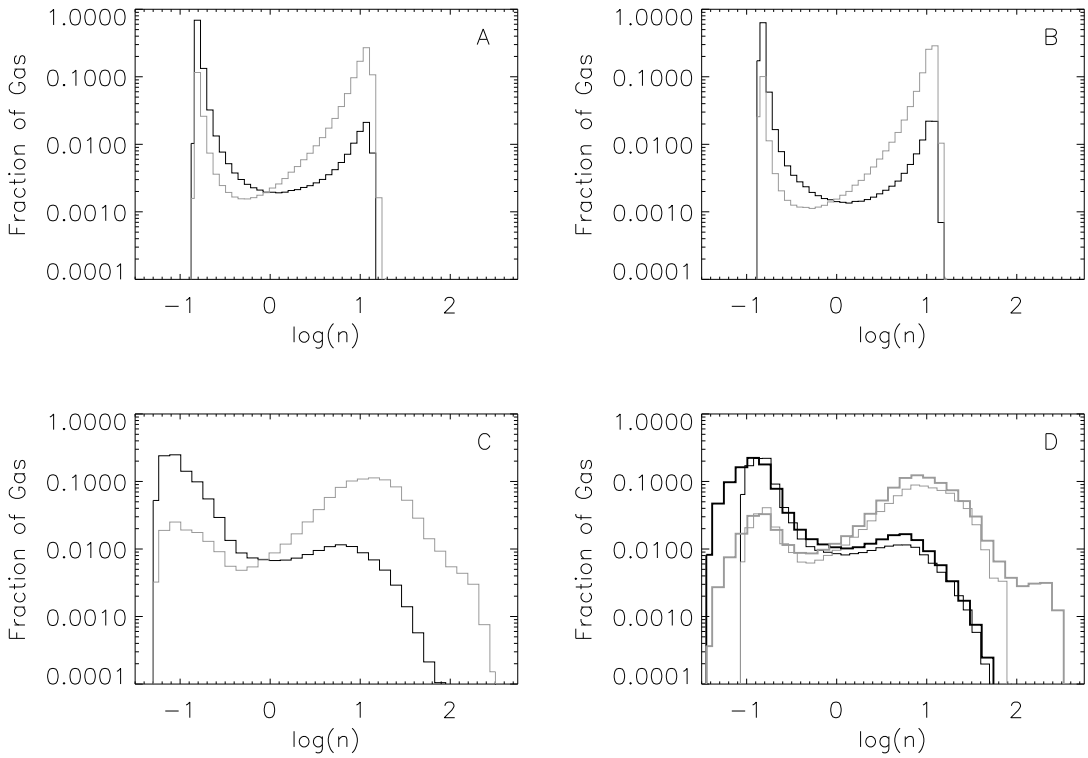

Figure 3.3: Volume (black line) and mass (grey line) weighted PDFs of density for the standard run at $t = 1, 2.5$, and 5.0 orbits (panels A-C, respectively). In Panel D we compare the PDFs for our two resolutions of 128^3 (thin lines) and 256^3 (thick lines) at $t = 9$ orbits. The PDF changes little between Panels A and B. In Panels C and D the development of the MRI increases the fraction of gas in the unstable phase, and forces gas to higher densities. In Panel D, the higher resolution run contains trace amounts of gas at more extreme densities.

warm, unstable, and cold phases. From $t = 1.0$ to $t = 2.5$ orbits (panels A and B of Figure 3.3) the evolution is driven mainly by galactic shear. The size distribution of the clouds shifts to larger masses through mergers, but the density PDFs over this interval vary little. The fraction of gas in each phase changes by only a few percent during this time period.

In contrast, between $t = 2.5$ and $t = 5.0$, Panels B and C of Figure 3.3, the evolution changes from being driven primarily by galactic shear, to being driven primarily by the MRI. The model becomes fully turbulent, and this has a significant

effect on the detailed shape of the density PDF. The fractions of gas in the warm, unstable, and cold phases at $t = 5.0$ are now 10%, 7%, and 83% by mass, and 84%, 8%, and 7% by volume. Near the end of the simulation, at $t = 9$, the gas fractions are 14%, 18%, and 67% percent by mass and 82%, 10%, and 6% percent by volume. From $t = 5$ to $t = 9$, (Panel D of Figure 3.3) the PDF remains very similar, indicating that the model has reached a quasi-steady state. At late times, gas is found at both lower and higher densities than was previously observed before the development of the MRI. Thus, the magnetized turbulence induces both strong compressions and significant rarefactions. Compared to the maximum ($\rho_{\rm max}$) and minimum ($\rho_{\rm min}$) densities before the onset of turbulence, $\rho_{\rm max}$ increases by an order of magnitude and $\rho_{\rm min}$ decreases by a factor of about 3. The fraction of gas in the intermediate density regime is a factor $2-3$ larger after the full development of MRI compared to early on. The proportion of thermally-unstable gas is never greater than 20% of the whole (for this set of parameters), but exceeds the proportion of thermally-stable warm gas during the turbulent stages of evolution.

To investigate properties of individual condensations in our model, we use an algorithm similar to that of CLUMPFIND (Williams et al. 1994). The algorithm was developed and applied by Gammie et al. (2003) to identify clumps in simulations of turbulent molecular clouds. Briefly, the algorithm first finds all local maximum values of density in the computational volume. All grid cells with a density higher than a chosen threshold density, n_t, are assigned to the nearest local maximum. This set of continuous zones defines a clump. The only other parameter needed is a smoothing length, applied to the initial density data cube (see Gammie et al. 2003); we set this to 1.5 grid zones. In Figure 3.4 we show the clump mass spectrum for two different choices of threshold density, $n_t = 8$ and 20 cm^{-3}. This mass spectrum is computed at $t = 6.5$ orbits. Mass spectra from other late times are similar. With

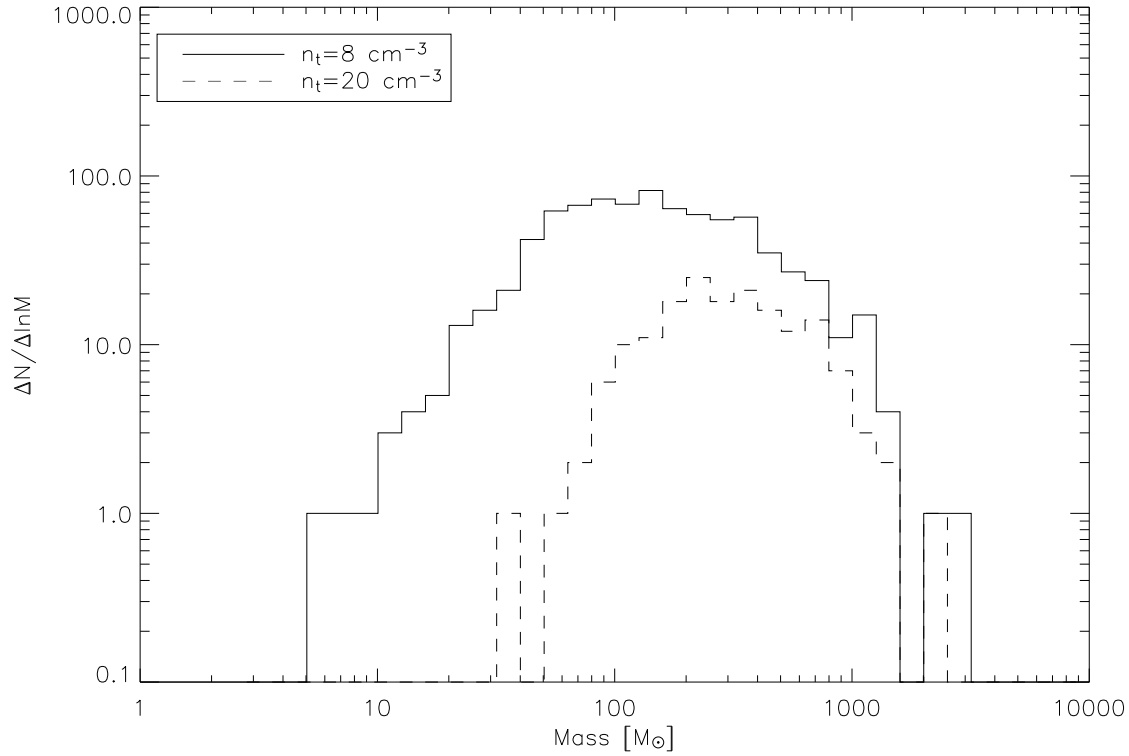

Figure 3.4: Mass spectrum of clumps from snapshot at $t = 6.5$ orbits, with threshold densities of 8 and 20 cm^{-3}.

$n_t = 8$ cm^{-3}, 812 clumps were found, with a minimum clump mass of 5.6 $M_\odot$, and a maximum mass of 2800 $M_\odot$. For reference, the total mass in the simulation is 2.51×10^5 $M_\odot$. Increasing the critical density to $n_t = 20$ cm^{-3}, we find 168 clumps, with a minimum mass of 35 $M_\odot$, and a maximum mass of 2200 $M_\odot$. For both cases, the peak of the mass spectrum is in the range $100 - 300$ $M_\odot$; the peak increases slightly for larger n_t.

To describe their shapes, we compute diagonalized moment of inertia tensors for each clump, following Gammie et al. (2003). Figure 3.5 plots the ratios, for each clump, of the smallest (c) and intermediate (b) axes to the largest (a) axis. Prolate-shaped clumps lie near the diagonal line, oblate clumps lie near the right side vertical axis, and triaxial clumps lie in the center. Using two dotted lines to

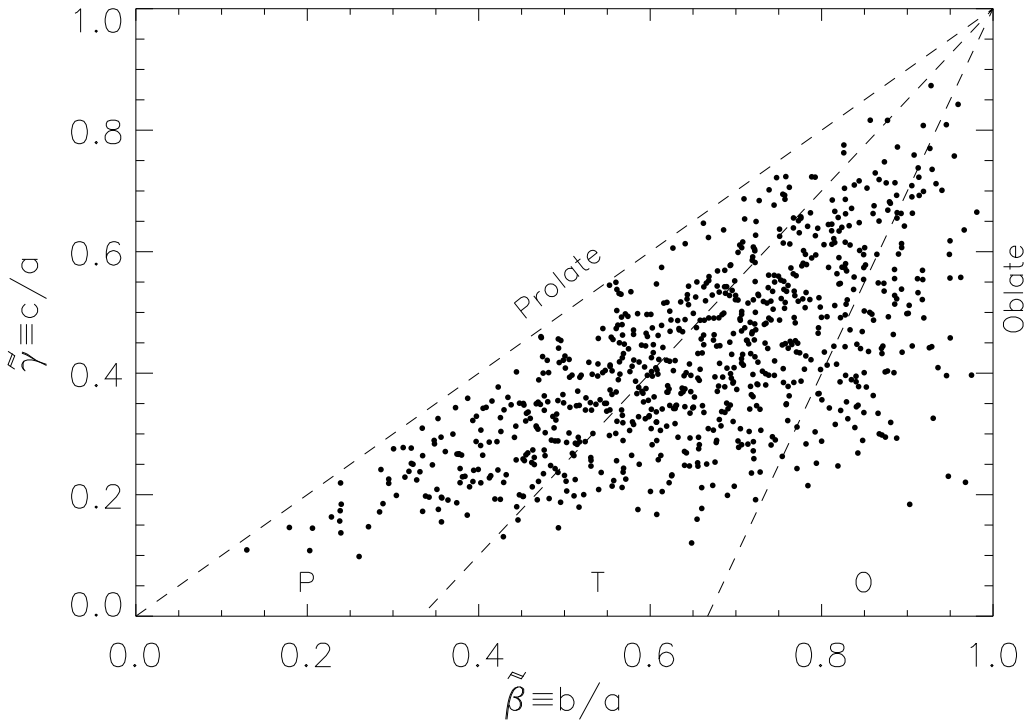

Figure 3.5: Axis ratios for clumps at $t = 6.5$ orbits, taking $n_t = 8$ cm^{-3}.

demarcate these groups, we find 38 % of the clumps are prolate, 49 % are triaxial, and 14% are oblate. Although clumps are certainly not round, typical minimum to maximum axis ratios are about 2:1. "Filaments", with c/a=0.1 are common, however, and these elongated structures are easy to pick out in Figure 3.2.

3.3.3 Pressure and Temperature Structure

The pressure PDFs at $t = 1, 2.5, 5$, and 9 orbits are presented in Figure 3.6. At $t = 1$, most of the gas falls within a narrow range of pressures, P/k=900-1300 K cm^{-3}. This is lower than P/k=2000 K cm^{-3} in the initial conditions, due to systematic cooling in the thermally unstable stage of evolution. The pressure PDF changes little from $t = 1$ to $t = 2.5$ orbits, shown in panels A and B of Figure 3.6. With the development of MRI, however, gas is driven to both higher and lower

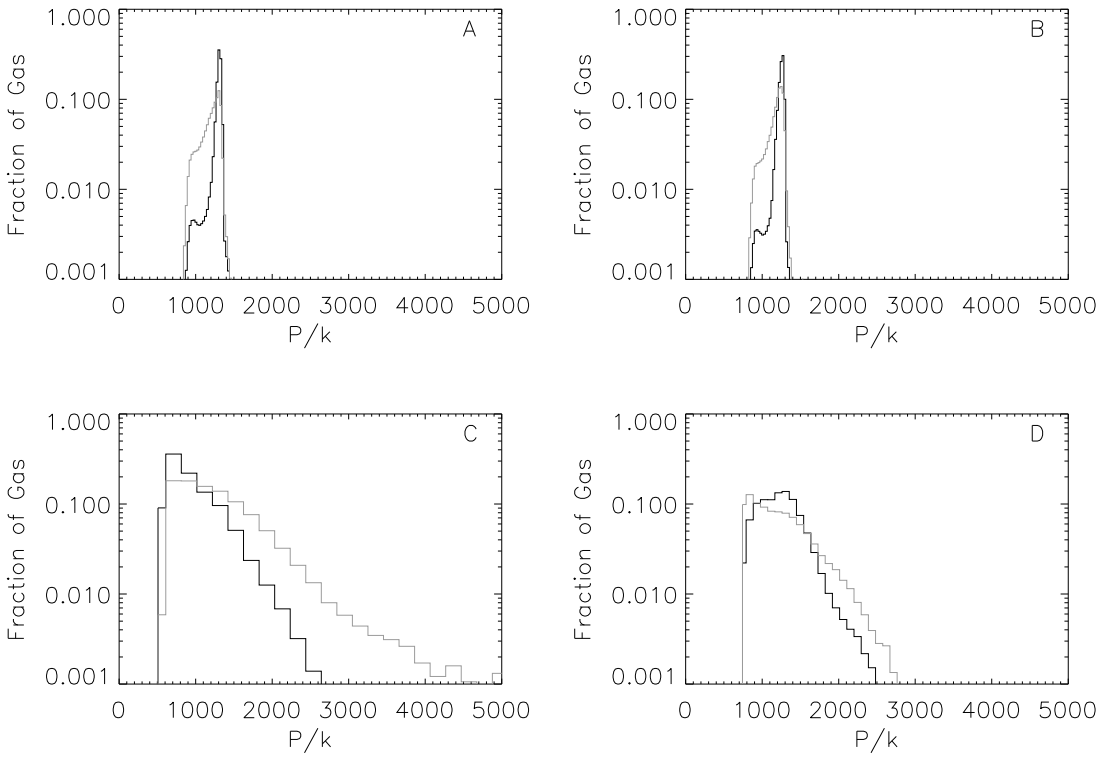

Figure 3.6: Volume (black line) and mass (grey line) PDFs of pressure for the standard run at $t = 1, 2.5, 5.0$, and 9 orbits (panels A-D, respectively). Early in the simulation most of the gas is found in the range of P/k=900-1300 K cm^{-3}. The MRI has drastically altered the pressure distribution in Panels C and D.

pressures, as can be seen in Panels C and D, at $t = 5$ to $t = 9$ orbits. The mean volume-weighted pressure at the end of the simulation is slightly lower than that after TI has developed, about P/k=1200 K cm^{-3}. The pressures in the cold and warm phases are approximately equal in the latter half of the simulation, while the pressure in the intermediate phase is slightly higher, about P/k=1300 K cm^{-3}. The dispersion in pressure early in the simulation is about δP/k $\sim$ 60 K cm^{-3}, while late in the simulation this increases to as much as δP/k $\sim$ 400K cm^{-3}.

In Figure 3.7 we show scatter plots of pressure against density overlayed on our model cooling curve at $t = 1, 2.5, 5$, and 9 orbits. We also show contours of constant temperature to indicate the transitions between different phases of gas. Only a

fraction of the zones are included because of the large number of cells contained in our 3D simulations. Early in the simulation (Panels A and B), the gas is close to pressure equilibrium, although high density gas lies closer to the thermal equilibrium curve. Later in the simulation (Panels C and D), strong interactions between clouds can drive gas far from pressure equilibrium. At low densities where the cooling time scale is longer than the dynamical time, gas can be found at pressures as high as P/k=3200 K cm^{-3} and as low as 800 K cm^{-3}, a range of a factor four. Much of the low-density gas is not in thermal equilibrium. In high density regions there is also a wide range of pressures observed (P/k=800-4000 K cm^{-3}), but because the cooling time is very short ($\sim 10^4$ yr) this gas maintains thermal equilibrium. At early times, distributions of density and pressure are quite similar to the corresponding results from our 2D models (Paper I) after the nonlinear development of TI. At late times, however, these 3D turbulent models show much broader pressure distributions than our 2D models. Overall, the mean pressure averaged over orbits 6-10 is 1206 K cm^{-3}. By phase the mean pressure is P/k = 1187, 1324, and 1195 K cm^{-3} in the warm, intermediate and cold phases.

Also of interest are the temperature PDFs, shown in Figure 3.8 at the same times as in Figure 3.3. In Panels C and D, the fraction of gas in the intermediate temperature phase has increased, and gas is also found at colder temperatures than are present earlier in the simulation. The minimum temperature is 80K, and respectively 60% and 68% of the gas mass is found between 80-120K at $t = 1$ and 2.5 orbits. At $t = 5$ and 9 orbits, on the other hand, respectively 30% and 18% of the gas is found at temperatures below 80K, while respectively another 32% and 31% of gas is at T=80-120 K. The range of temperatures in which the majority of cold gas is found increases by about a factor of two. The upper limit on temperature increases slightly throughout the run, but in addition, the dispersion of temperatures in the

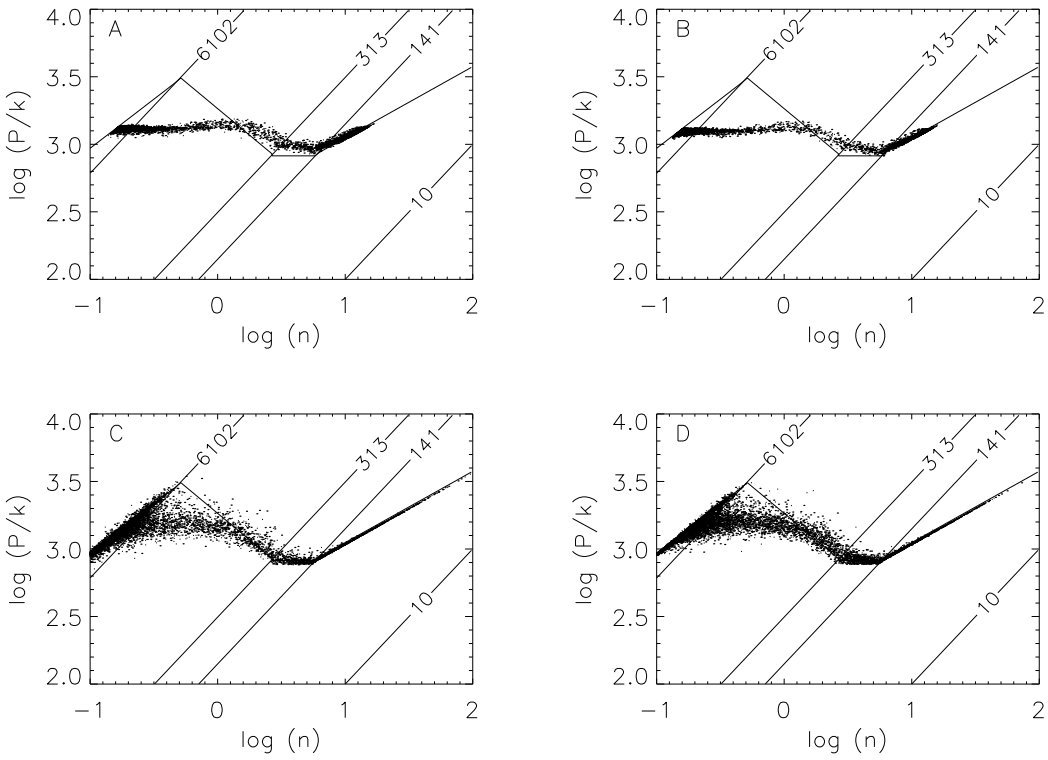

Figure 3.7: Scatter plot of n and P/k for the standard run, at $t = 1, 2.5, 5.0$, and 9 orbits (panels A-D, respectively). The equilibrium cooling curve is plotted for comparison, along with temperature contours corresponding to the transitions between the warm, unstable, and cold phases of gas.

warm medium increases. At early times, ∼80% of the warm gas is in the range T=6600-8600K, whereas at late times, 80% is evenly distributed over twice as large a spread in temperatures.

Figure 3.9 compares the volume-weighted temperature PDFs of four runs of different mean density. These four runs have average densities of $\bar{n} = 4.0, 1.5, 1.0$, and $0.67\,\mathrm{cm}^{-3}$ and, as we shall discuss in §3.3.4, the mean velocity dispersion increases by an order of magnitude from the highest to lowest mean density models. The PDFs in Figure 3.9 represent averages from 6.0-6.5 orbits. At intermediate and high temperatures, the PDFs for these runs are quite similar. Most of the warm gas is at T=6000-8000 K, with $\mathrm{T_{max}} \approx 10000$ K. Most of the cold phase is at temperatures

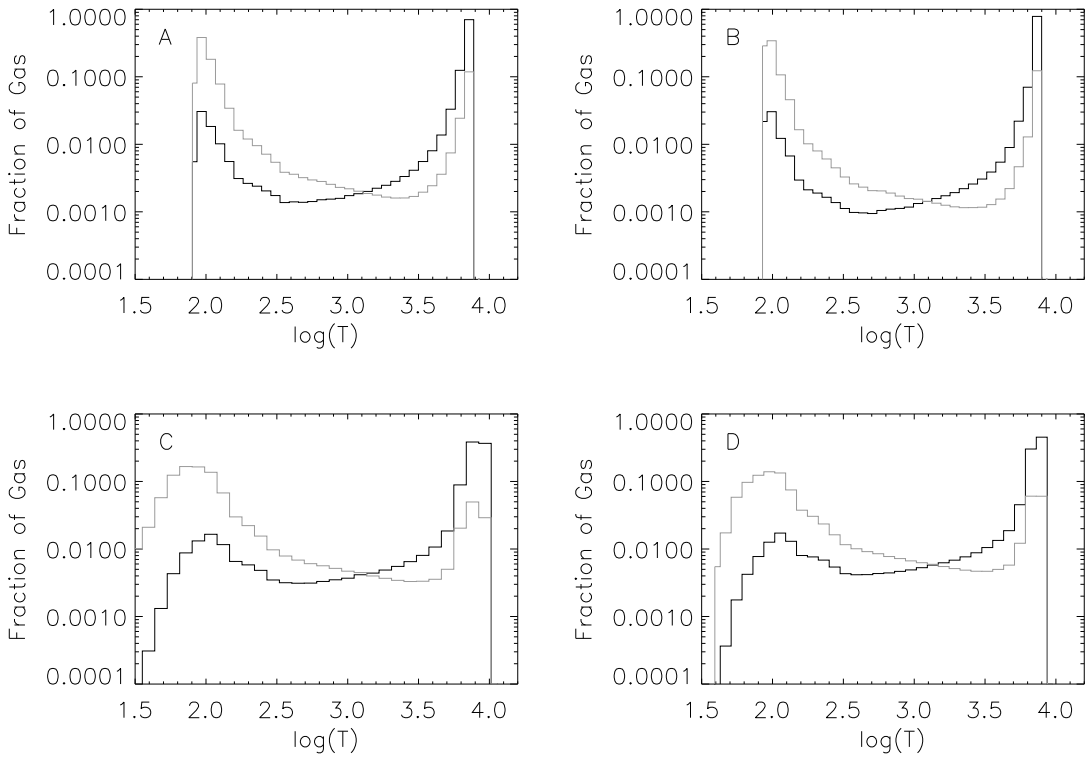

Figure 3.8: Volume (black line) and mass (grey line) weighted temperature PDFs for the standard run at $t = 1, 2.5, 5.0$, and 9 orbits (panels A-D). As for the density PDF, the temperature PDF changes little between Panels A and B. In Panels C and D the development of the MRI forces gas to higher density, which results in the lower temperatures seen in Panels C and D. In addition, the ranges of temperatures for the warm and cold gas peaks also increase.

near 100 K, possibly showing a slight trend towards higher mean temperature as $\bar{n}$ is decreased. Overall there is less gas at lower temperature when $\bar{n}$ is reduced, because the total mass available for cold clouds is lower. In addition to having similar warm and cold gas temperatures, the models with various $\bar{n}$ are similar in that the fractions of gas in the intermediate- and warm-temperature regimes are always quite close. These results are illustrated in Figure 3.10, which plots the mass fractions in the various regimes as a function of $\bar{n}$ (also including the $\bar{n} = 0.25$ model).

Overplotted in Figure 3.10 are curves indicating the warm and cold gas mass fractions that a pure two-phase medium would have. The mass fraction of cold

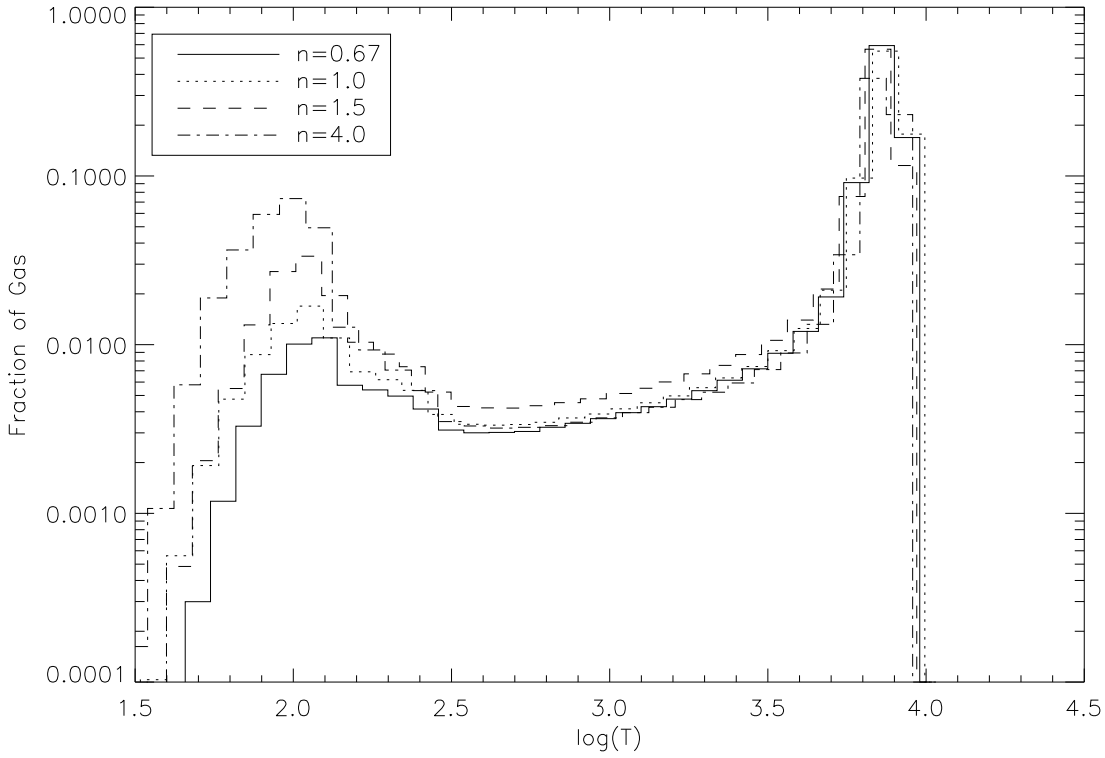

Figure 3.9: Comparison of volume-weighted temperature PDFs for runs with $n = 0.67, 1.0, 1.5$, and $4.0\ \mathrm{cm}^{-3}$, as indicated. The PDFs are averaged over $t = 6.0-6.5$ orbits. The temperature structure is essentially the same, but as the average density is decreased, the cold gas occupies a smaller total volume, lowering the PDF at low temperature.

gas in a perfect two-phase medium in thermal and pressure equilibrium is $f_c = (1 - n_w/\bar{n})/(1 - n_w/n_c) \approx 1 - n_w/\bar{n}$, where n_c is the cold density, n_w is the warm density, and $\bar{n}$ is the mean density. The mass fraction of warm gas is then $f_w \approx n_w/\bar{n}$. The density of warm gas in our simulations is typically $n_w = 0.25$, which we use to compute the theoretical curves in Figure 3.10.

The possibility exists that our choice of initial conditions in the standard run, a uniform medium at the average density, may have some effect on the amount of gas in the intermediate phase at late times. Due to TI, initially most of the gas collects into small , dense cold clouds, and only a small proportion of the gas remains in

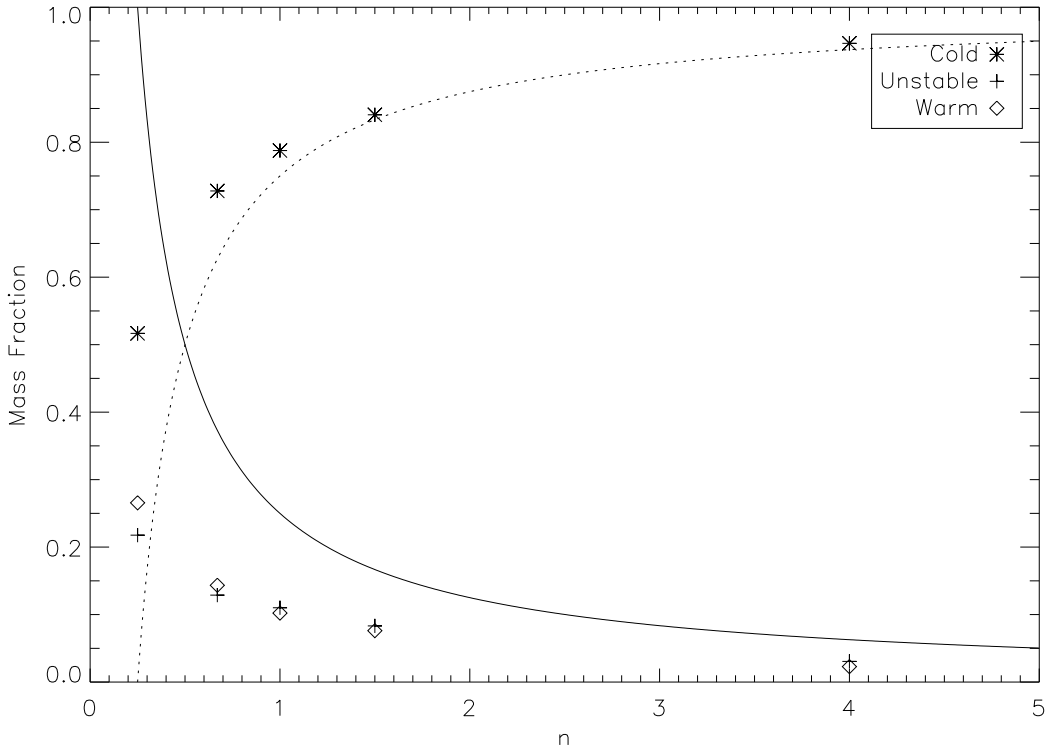

Figure 3.10: Mass fractions for the cold, unstable, and warm phases as a function of mean simulation density, $\bar{n}$. The dotted and solid lines represent the theoretical mass fractions of the cold and warm phases, respectively, for a perfect two-phase medium in pressure equilibrium, assuming the density of the warm medium is $n_w = 0.25$ cm^{-3}, which is typical for our simulations.

the thermally unstable regime. Later in the simulation, the MRI drives a larger fraction of gas into the unstable phase. It is possible that if we had *begun* with a turbulent medium, this fraction would be even larger, from increased shock heating of moderate density clouds with larger collision cross sections. To investigate this, we initialized a simulation with the same mean density and magnetic field as our standard run, but evolved it with an isothermal equation of state. The sound speed was set so that the initial P/k matches late time averages from our standard run. After the isothermal evolution has proceeded for 10 orbits and reached a saturated turbulent state, heating and cooling are enabled. After a quasi-steady state is

reestablished, we measure the mass fractions in the warm, intermediate, and cold regimes. The result is respective proportions of about 11%, 14%, and 75%, which is similar to our results from standard run. Thus, we conclude that the long-term thermal history does not strongly affect the present state of the gas.

3.3.4 Turbulent Velocities

In Figure 3.11 we plot the mass-weighted Mach number $\mathcal{M} \equiv \delta v / c_s$ of the gas in each thermal phase (warm, intermediate, cold) as a function of time for the duration of the simulation. We also include, for comparison, the mass-weighted Mach number of the cold medium for the high resolution run at 256^3. The isothermal sound speed $c_s = (\mathrm{kT}/\mu)^{1/2}$ is computed individually for all grid zones, and the galactic shear is subtracted from the azimuthal (v_y) velocity before computing $\delta v^2 = v_x^2 + (\delta v_y)^2 + v_z^2$. Initially, motions in all three phases of the gas are subsonic, $\mathcal{M} < 0.3$, and remain so until the MRI begins to develop at about 800 Myr ($\sim$ 3 orbits). Once the MRI saturates (at $t \sim 5$ orbits), the typical Mach numbers of the warm, intermediate and cold phases of the gas are 0.4, 1.8, and 2.9. The peak value of $\mathcal{M}$ for the cold phase is about 3.2. The mean late time velocity dispersion for all three phases of the gas is similar, approximately 2.7 km s^{-1}. At late times, the individual velocity dispersions in the radial, azimuthal, and vertical directions are 1.9, 1.7, and 0.7 km s^{-1}, respectively.

To explore the dependence of saturated state turbulence on system parameters, for our five simulations of varying mean density $\bar{n}$ we have computed the average Mach number over $t = 5 - 10$ orbits. We plot the results, separating the three thermal phases, as a function of $\bar{n}$ in Figure 3.12. The relationships between $\mathcal{M}$ and $\bar{n}$ clearly follow power laws. The slopes for the warm, intermediate and cold phases are $d \ln \mathcal{M} / d \ln \bar{n} = -0.67, -0.68$ and -0.77. Since the cold component dominates the

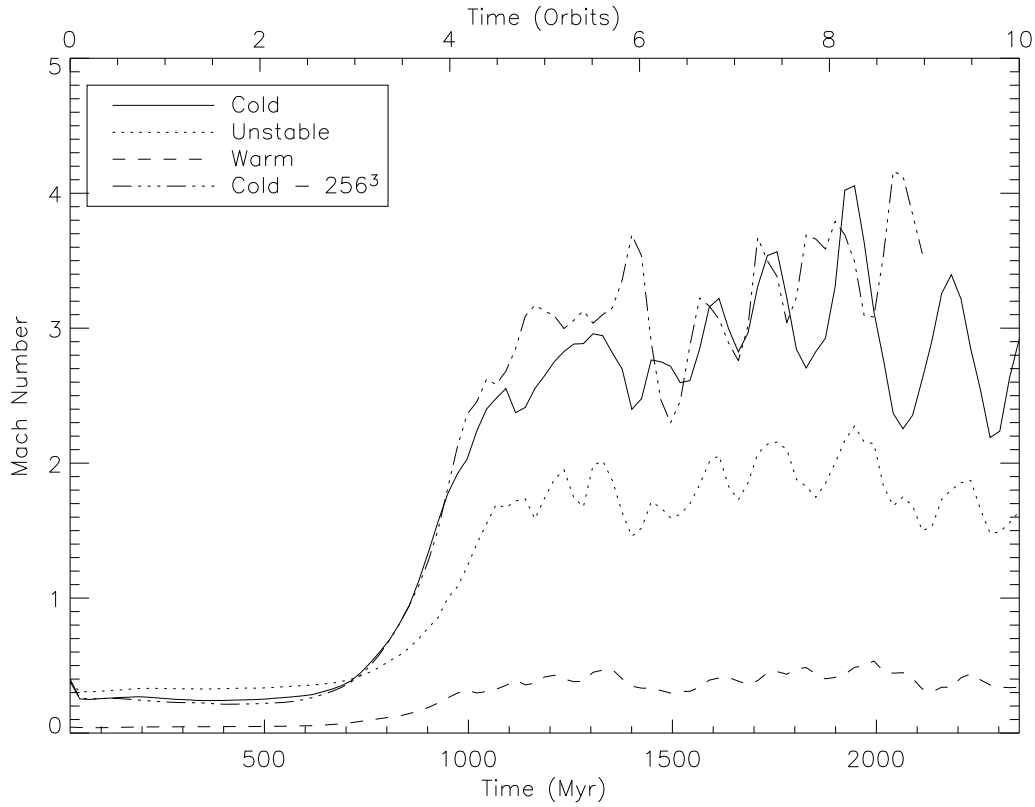

Figure 3.11: Mass weighted Mach number for the three phases of gas in the standard model. The average Mach number for the second half of the simulation is 0.4, 1.8, and 2.9 for the warm, unstable, and cold phases. For comparison we also plot the mass weighted Mach number of the cold medium for the high resolution 256^3 run.

mass, this implies $(\delta v) \propto (\bar{n})^{-0.77}$ overall. For our $\beta = 1000$ model at $\bar{n} = 1$ cm^{-3}, the saturated state Mach numbers are 0.3, 1.1, and 1.6 for the warm, intermediate, and cold phases. Our results are thus consistent with general findings from previous MRI simulations that saturated-state turbulent amplitudes increase with increasing mean Alfvén speed. The detailed scalings, however, show interesting differences, which we shall discuss in §3.4.

We have found that the turbulence is quite insensitive to particularities of structure in initial conditions. Thus, our model which began with a two phase "cloudy" medium, with the same initial mean density as our standard run, saturates with

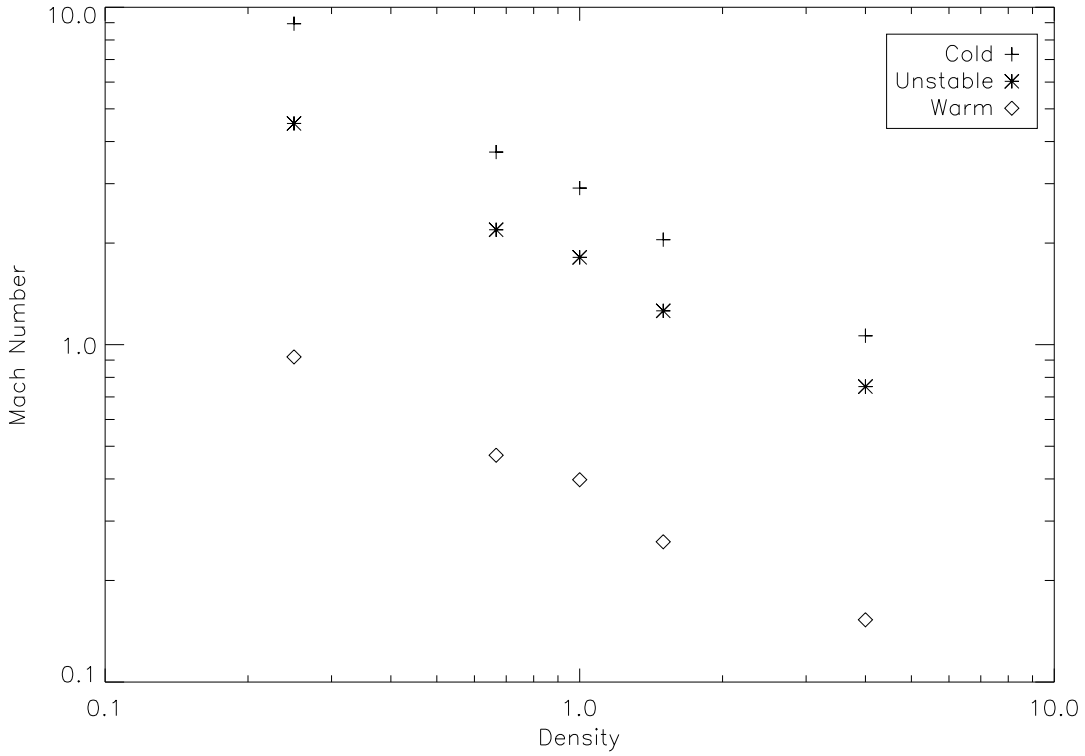

Figure 3.12: Mach number, separated by phase, plotted against the average density in the box for five different simulations. Mean densities of models are $\bar{n} = 0.25, 0.67, 1.0, 1.5$ and 4.0 cm^{-3}. Linear fits to the results give power law slopes of -0.67, -0.68 and -0.77 for the warm, unstable, and cold phases, respectively.

nearly the same velocity amplitude as the standard run. The initially-isothermal run which was restarted with cooling also yielded similar results to the standard run, with Mach numbers of 0.4, 1.7, and 2.8 for the warm, intermediate and cold phases. The saturated state of the isothermal simulation itself has a Mach number of 1.4, corresponding to mean velocity dispersion 4.0 km s^{-1}, somewhat larger than for our cooling models at this fiducial mean density. Differences between isothermal and multiphase models are likely to depend on $\bar{n}$, however.

The average Reynolds stress, $\langle \rho v_x \delta v_y \rangle / P_0$, from $t = 5 - 10$ orbits is plotted against the mean density for $\bar{n} = 4.0, 1.5, 1.0, 0.67$, and 0.25 cm^{-3} in Figure 3.13.

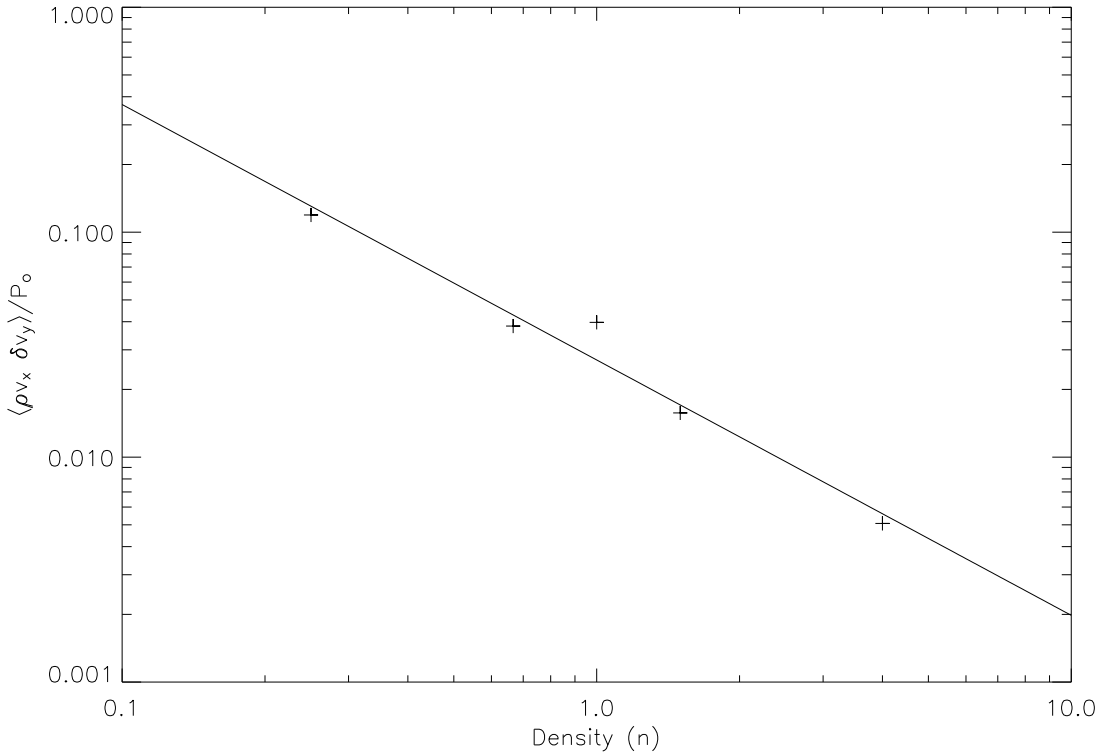

Figure 3.13: Reynolds stress plotted against the mean density for five different simulations with $\bar{n} = 0.25, 0.67, 1.0, 1.5$ and 4.0 cm^{-3}. A fit gives a power law slope of -1.1.

The relationship again follows a power law, with a slope of -1.1.

The velocity power spectra are generally consistent with previous simulations of the MRI (Hawley, Gammie, & Balbus 1995; Kim, Ostriker, & Stone 2003). The largest scales dominate the simulation, generally following a Kolmogorov-like spectrum, $\sim k^{-11/3}$. Our quoted values for the velocity dispersions therefore correspond to the largest scales in the simulations. On smaller scales, such as an individual cloud, the velocity dispersion would be smaller. We have tested the relation between linewidth and size directly, using the "ROC" analysis approach described in Ostriker, Stone, & Gammie (2001). Both for the cold component alone, and for the whole medium, we find that the velocity dispersion increases with the size of clouds, or sub-boxes of the computational volume.

3.3.5 Magnetic Fields

Similarly to the (random) kinetic energy, the magnetic energy increases as the MRI develops. In Figure 3.14 we plot the magnetic field strength as a function of time for each of the three phases of gas. In the initial conditions, $B = B_z = 0.26$ μG. After TI develops, the field strength is 0.25 μG for the warm phase, and about 0.5 μG for the (denser) unstable and cold phases. As the MRI develops, after $t = 5$ orbits, the field strength grows to range over $2 - 3$ μG for all three phases, reaching as high as 4.1 μG in the cold phase. The late time component magnetic field strengths, $\langle B_x^2 \rangle^{1/2}, \langle B_y^2 \rangle^{1/2}$, and $\langle B_z^2 \rangle^{1/2}$ are 1.3, 1.9, and 0.51 μG, averaged over $t = 6 - 10$ orbits. Thus, the MRI enhances the magnetic field by an order of magnitude over its initial value. We note that if overdense clouds were to form by isotropic contraction of the ambient medium, then one would expect $\langle B^2 \rangle^{1/2} \propto \rho^{2/3}$. With a cold medium density two orders of magnitude larger than that of the warm medium, the respective mean field strengths would differ by a factor 20. Since this is not the case, condensation evidently proceeds preferentially along field lines.

To explore dependence on mean properties, in Figure 3.15 the late time magnetic field strength, averaged over five orbits, is plotted against the mean density in the box for five simulations with $\bar{n} = 4.0, 1.5, 1.0$, and 0.67 cm^{-3}. Unlike the turbulent velocity dispersions, the B field strength does not show any significant trend with $\bar{n}$, saturating between 2 and 3 μG. The field strength also does not differ significantly between the cold, intermediate, and warm phases for any of the models. As a marginal effect, the field strength in the warm medium decreases as $\bar{n}$ increases.

Unlike the magnetic energy density, the Maxwell stress does show dependence on $\bar{n}$. This stress, $\langle -B_x B_y / 4\pi \rangle / P_0$, is averaged over $t = 5 - 10$ orbits and plotted against the mean density for five simulations with $\bar{n} = 4.0, 1.5, 1.0, 0.67$ and 0.25

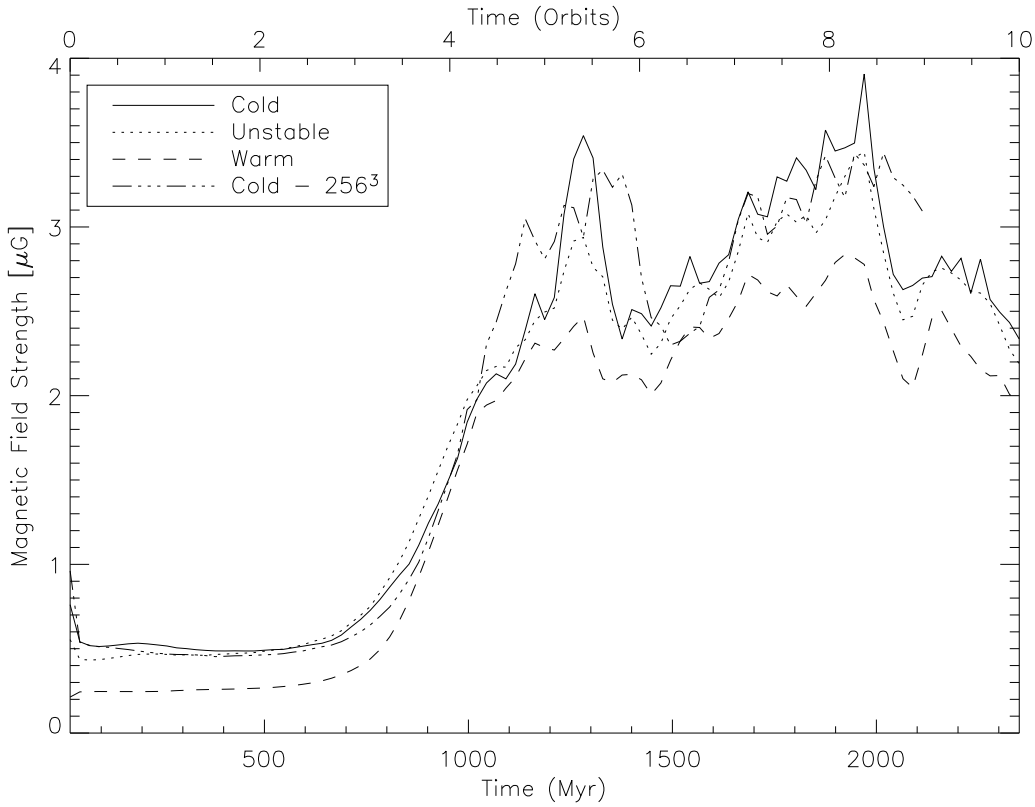

Figure 3.14: Magnetic field strength plotted against time for the standard run (with initial $\beta = 100$, i.e. $(B_z)_{init} = 0.26$ μG). The typical saturated state field strength is $2 - 3$ μG, with little difference between the three phases. For comparison we also plot the field strength in the cold medium for the high resolution 256^3 run.

cm^{-3} in Figure 3.16. For the data shown, a power law fit yields slope -0.42. Previous single-phase MRI simulations show somewhat different scalings of Maxwell stresses and magnetic energies, as we shall discuss in §3.4.

The power spectra of the magnetic field, like the velocity power spectra, is consistent with previous simulations of the MRI (Hawley, Gammie, & Balbus 1995; Kim, Ostriker, & Stone 2003), dominated by the largest scales and generally following a Kolmogorov-like spectrum.

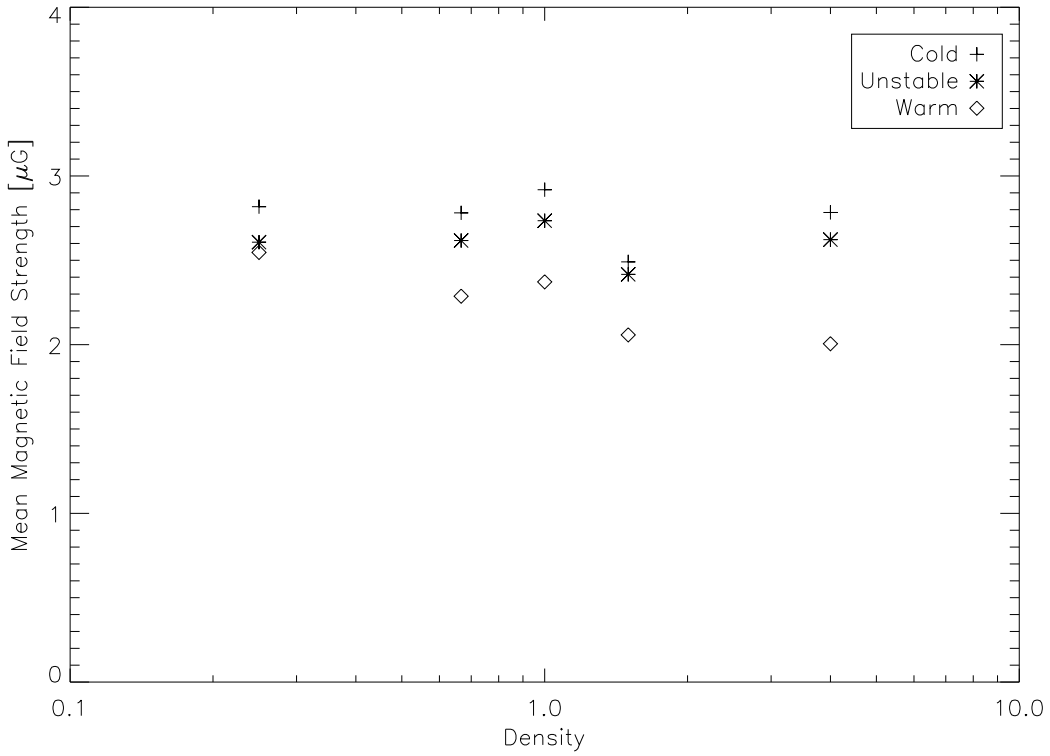

Figure 3.15: Late time magnetic field strength as a function of density for five runs with $\bar{n} = 0.25, 0.67, 1.0, 1.5$ and 4.0 cm^{-3}.

3.3.6 Energetics

Tracking the changes in various energies is key to understanding the interrelationships between dynamics and thermodynamics in turbulent flows. For the models we have performed, the ultimate energy source is the shear flow, which drives the MRI. In turn, turbulent dissipation can convert kinetic and magnetic energy to thermal energy, which can subsequently be lost to radiation. More formally, following HGB1, we consider the average over the box of the total energy per unit volume,

$$\langle \mathcal{H} \rangle = \left\langle \rho \left(\frac{1}{2} v^2 + \frac{\mathcal{E}}{\rho} - \frac{q\Omega^2 x^2}{2} \right) + \frac{B^2}{8\pi} \right\rangle . \tag{3.5}$$

Changes to this energy can occur due to losses or gains from radiation, and from fluxes through and stresses on the surface of the computational volume. With

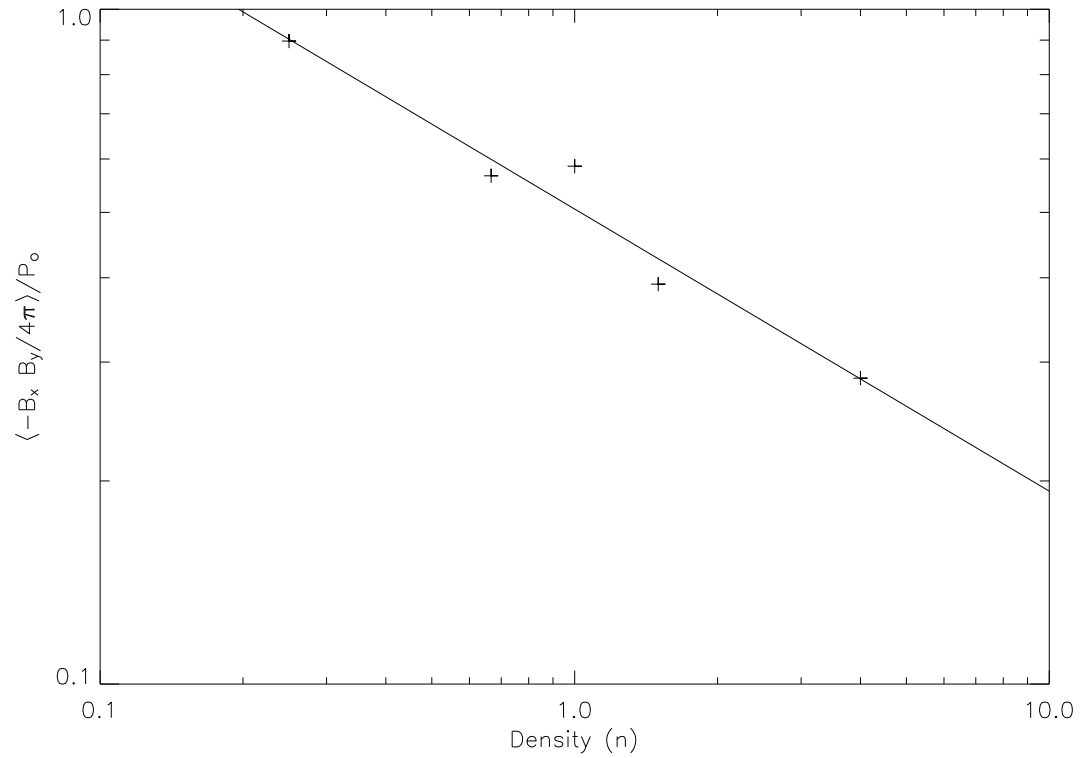

Figure 3.16: Maxwell stress as a function of mean density for five runs with $\bar{n} = 0.25, 0.67, 1.0, 1.5$ and 4.0 cm^{-3}. A fit gives a power-law slope of -0.42.

shearing-periodic boundary conditions, the net rate of change should ideally obey

$$\frac{d}{dt}\langle \mathcal{H} \rangle = q\Omega \left\langle \rho v_x \delta v_y - \frac{B_x B_y}{4\pi} \right\rangle + \langle -\rho \mathcal{L} \rangle. \tag{3.6}$$

Thus, if quasi-steady state is reached, we would then expect $d\langle \mathcal{H} \rangle / dt = 0$, and the sum of stresses times $q\Omega$ to equal the cooling rate. In steady state, from equation (3) the total rate of work done by the combination of compressions and shocks, $\langle -P\nabla \cdot \mathbf{v} \rangle + \langle \left(\frac{\partial \mathcal{E}}{\partial t}\right)_{shocks} \rangle$, plus any other dissipation, should also be balanced by the net cooling, $\langle \rho \mathcal{L} \rangle$.

In the upper panel of Figure 3.17 we plot (for our another realization of our standard run) the rate of work done by Reynolds and Maxwell stresses per unit volume. The late-time volume-averaged energy inputs from Maxwell and Reynolds stresses are 3.7 and 0.6 (in units of $P_0\Omega/2\pi$). The Maxwell stress dominates the

Reynolds stress, which is typical in simulations of the MRI. In the lower panel of Figure 3.17 we plot the volume averaged shock heating, radiative heating - cooling rates, $-\langle\rho\mathcal{L}\rangle$, and pressure work, $-\langle P\nabla\cdot v\rangle$, as a function of time. The sum of these three terms is approximately zero during the first few orbits of the simulation. Later in the simulation there is typically either net heating or cooling at any particular time, but the late time averages - individually, 1.0, -0.7, and -0.3 (in units of $P_0\Omega/2\pi$) for shock, radiation, and pressure terms - sum to zero. Thus, on average, radiative losses exceed radiative gains, cooling by rarefactions exceeds heating by compressions, and together these net loss terms balance gains in shocks. The mean energy density typically varies by 10% during the latter half of the simulation.

If total energy were perfectly conserved, as noted above, the energy inputs from Maxwell and Reynolds stresses would be balanced by net cooling. The energy source for this radiative cooling would, in turn, be provided by compressive work and dissipation of turbulence. The present simulation, however, in fact captures only part of the turbulent dissipation – that in shock heating, as mediated by artificial viscosity. In addition, both magnetic and kinetic turbulent energy are lost at the grid scale. Oppositely-directed magnetic fields and shear flows, when advected into a single zone, are averaged to zero. Since ZEUS evolves a (non-conservative) internal energy equation rather than a total energy equation, the associated energy from those small-scale sheared $\mathbf{v}$ and $\mathbf{B}$ fields is lost. In principle, these dissipation terms could be captured if explicit resistivity and shear viscosity were included.

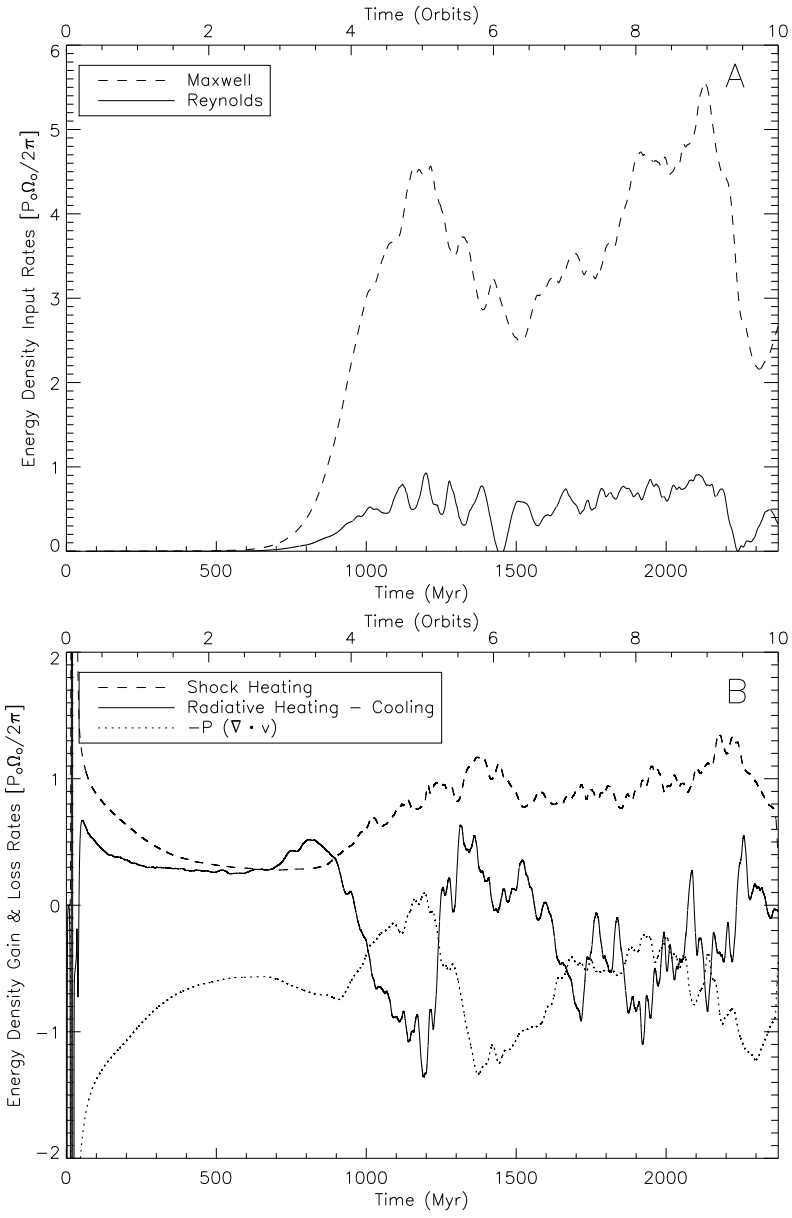

Figure 3.17: In Panel A (upper) we show volume averaged energy input rates from Maxwell and Reynolds stresses plotted against time for a run with standard parameters. In Panel B (lower) we plot the volume averaged energy density gain and loss rates of shock heating, radiative heating - cooling, and $-P(\nabla \cdot v)$ work, plotted against time, for the same run.

3.3.7 Synthetic Line Profiles

Although the present simulations are highly idealized in many ways (e.g. they are vertically periodic rather than stratified), it is interesting to explore model properties that bear a close relation to observables. The profiles of 21 cm HI absorption directly trace the density, temperature, and turbulent velocities of the atomic ISM via a line-of-sight convolution. Using our simulated "data," we can generate analogous maps of line profiles projected in any direction through the computational volume. Figures 3.18, 3.19, and 3.20 show synthetic emission profile maps for our standard model along the x, y, and z directions. We also present, paired with each line-of-sight velocity profile, the corresponding distribution of total emission with line-of-sight position. Each of the 8×8 windows on the map represents a volume of $32 \times 32 \times 256$ zones, integrated over the projected area. For each zone, the contribution to emission is proportional to the density, with a Gaussian velocity distribution centered on the flow velocity, and dispersion $= \sqrt{\mathrm{kT}/\mu}$. Strong lines indicate more total mass along a given line of sight, and weak lines indicate less mass. Since most of the mass in our standard model is in the cold phase, a strong line indicates the presence of cold, dense gas.

For Figures 3.18, 3.19, and 3.20 the mean line widths of the velocity profiles are 1.8, 1.9, and 1.7 km s^{-1}. Without thermal broadening the line widths are reduced to 1.0, 1.3, and 0.7 km s^{-1}, which is consistent with the time-averaged velocity dispersions in the radial, azimuthal, and vertical directions reported in §3.3.4. Most of the velocity profiles are single-peaked, and would likely be interpreted as arising from one to three emitting components if a standard Gaussian fitting procedure were applied. However, our results show that in many cases several spatially-separated components are distinctly evident in the line-of-sight mass distributions. Velocity

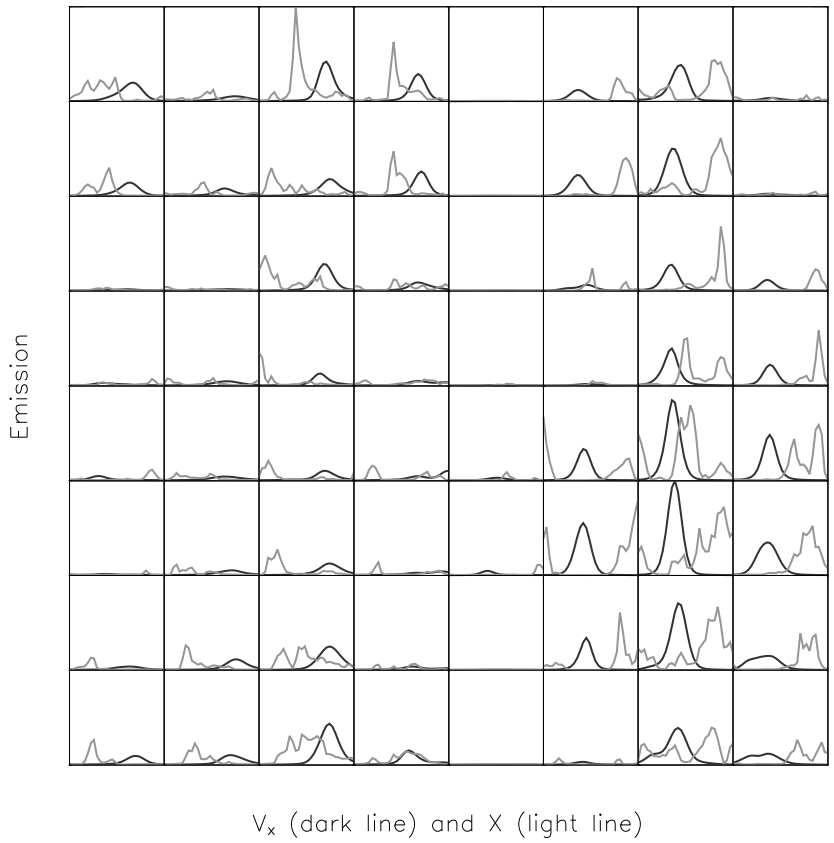

Figure 3.18: Position and velocity profile map in Y-Z plane, for standard run projected along $\hat{x}$. Dark lines show integrated emission profiles as a function of v_x along the line-of-sight direction. Light lines show profiles of emission as a function of x integrated over line-of-sight velocity.

profile broadening and skewness statistically give evidence that more than one component is present, but we find no correlation between increased spatial coherence and increased velocity profile symmetry in any given direction. We do not observe any structure which shows two distinct lines. The absence of velocity profiles with two distinct peaks owes in part to the thermal broadening, which smears out smaller scale features. However, the primary reason that profiles are single-peaked is that velocity modes at a large range of wavenumbers are present in saturated state MRI-driven turbulence. Since there is no single dominant wavelength along the line-of-sight, the range of velocities is smoothly filled.

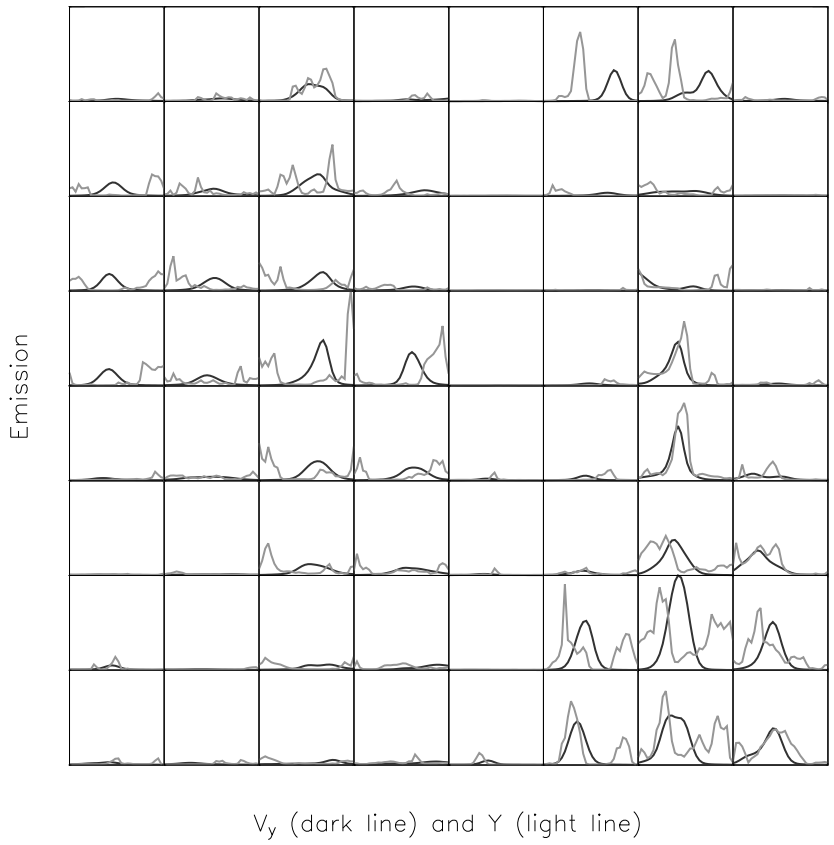

Figure 3.19: Same as Figure 3.18, for X-Z map projected along $\hat{y}$.

The spatial resolution of the synthetic observations was doubled to determine if the structure of the velocity profiles would be affected. Generally, the line profiles remain single-peaked, whether or not well-separated spatial components are present. In Figure 3.21 we show velocity profiles for the warm gas only, and do not include thermal broadening. The line-of-sight position profile (also in Figure 3.21) shows that the warm gas is spatially much more uniformly distributed than the cold gas, which dominates the profiles in Figures 3.18 - 3.20. Interestingly, however, the intermediate-temperature gas is always associated with cold condensations. This is clearly seen in Figure 3.22, which shows slices through the volume both before and after the onset of strong turbulence.

The line profiles for runs with different mean density are very similar to the

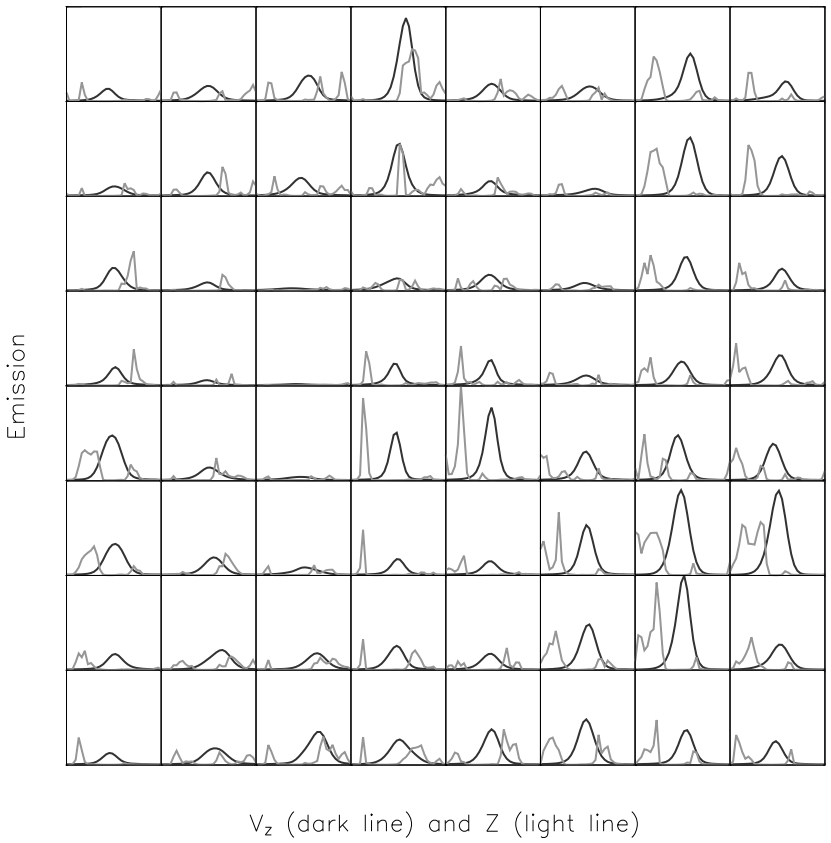

Figure 3.20: Same as Figure 3.18, for X-Y map projected along $\hat{z}$.

standard run. They typically show a single component with occasional evidence for a weaker second component. As the mean density is decreased to n = 0.67 and 0.25 cm^{-3}, the line widths increase to 2.0, 2.2, and 1.9 km s^{-1}, and 4.8, 4.7, and 4.5 km s^{-1}, respectively. Without thermal broadening the line widths are reduced to 1.1, 1.5, and 0.74 km s^{-1}, and 2.2, 2.2, and 1.1 km s^{-1}, respectively. A similar trend of decreasing line width with increasing mean density is also observed.

Figure 3.21: Same as Figure 3.18, for warm gas only, without thermal broadening.

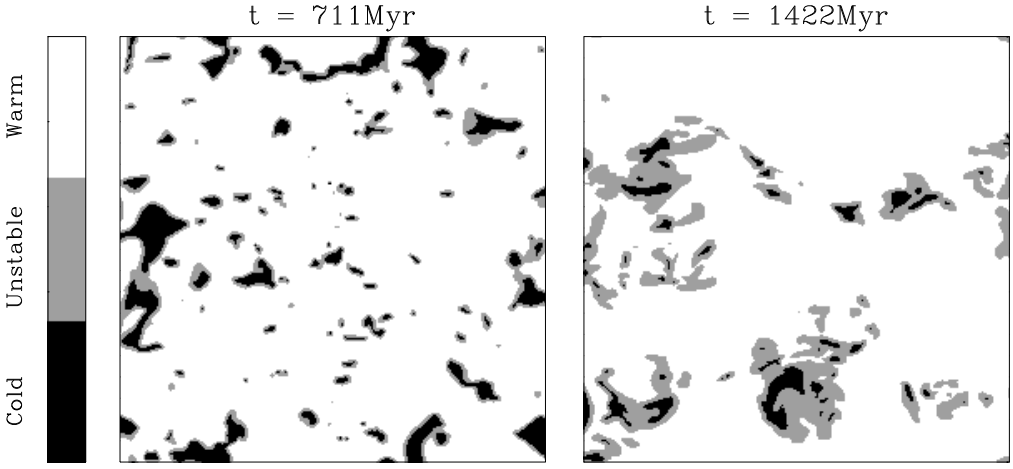

Figure 3.22: A slice at y=constant through the data cube showing the distribution of cold, unstable, and warm gas, before and after the MRI has begun to dominate th e dynamics.

3.4 Summary and Discussion

In this paper, we present results from a set of numerical MHD simulations that focus on the interrelationship between turbulence and thermal structure. The models we have performed are three dimensional, and include sheared galactic rotation and magnetic fields. Turbulence therefore is generated by the magnetorotational instability. We also include a radiative cooling function that, in pressure equilibrium, would yield a two-phase medium. The two fundamental issues we have addressed are (1) how cloudy structure alters the saturated-state properties and scalings of MRI-driven turbulence, compared to single-phase MRI models, and (2) how turbulence that is *not* driven by direct (stellar) thermal energy inputs affects the thermal balance and phase structure in the warm/cold atomic medium.

3.4.1 Summary of Model Results

Our primary findings are as follows:

1. *Evolution and physical structure:* A two-phase cloudy medium with many small clouds develops in the first 20 Myr of our simulations. Over time, due initially to galactic shear, and later ($t > 5$ orbits) to MRI-driven turbulence, these clouds undergo a continual series of mergers and disruptions, leading to a late-time state in which the mass function of condensations peaks at a few hundred $M_{\odot}$. The dense condensations are triaxial, and typically have max:min axis ratios of 2:1. They consist of cold gas lumps surrounded by envelopes of thermally-unstable gas; filling all of the remaining volume is thermally-stable warm gas.

2. *Density and temperature distributions:* For the range of parameters we have explored, in late stages of evolution most of the gas mass is in the cold phase, while most of the volume is occupied by the warm phase. While the proportion of

thermally-unstable intermediate-temperature gas in a given model increases after the advent of MRI, at all stages the density and temperature PDFs show distinct warm and cold phases, with a varying amount of material in the "non-equilibrium" valley between these peaks. The peaks, near $T = 100$ K and $T = 8000$ K, also broaden as the turbulence develops. The relative proportions in each phase depend on the mean density, varying from 95% cold gas when the mean density $\bar{n} = 4.0$ cm^{-3}, to 50% cold gas when $\bar{n} = 0.25$ cm^{-3}. The fractions of thermally-unstable gas and warm gas are always comparable to each other. Increasing levels of turbulence yield increasing proportions of thermally-unstable gas. Relative to the proportions predicted for a two-phase, quiescent medium in thermal and pressure equilibrium, increasing turbulence also tends to *increase* the fraction of cold gas, while decreasing the fraction of warm stable gas.

3. *Pressure:* We initialize our models at $P/k = 2000$ K cm^{-3}, but secular cooling in the stages before MRI develops leaves the gas in approximate pressure equilibrium ($\Delta P/\bar{P} < 0.1$) at a lower mean pressure of $P/k = 1300$ K cm^{-3}, near the minimum for which two stable gas phases can be present. After MRI develops, pressures cover a much wider range of values ($\Delta P/\bar{P} \sim 0.5$), with a maximum at $P/k \sim 4000$ K cm^{-3}, but relatively unchanged mean value ($\bar{P}/k = 1200$ K cm^{-3}).

4. *Turbulent velocities:* After the MRI saturates at ~ 5 orbits, the turbulent velocity dispersion reaches a quasi-steady plateau – albeit with fluctuations of $\sim 30\%$ in amplitude. For our fiducial model with $\bar{n} = 1$ cm^{-3}, the mean late time (3D) velocity dispersion is $\delta v \equiv \langle v_x^2 + (\delta v_y)^2 + v_z^2 \rangle^{1/2} \approx 2.7$ km s^{-1} for all three components. This velocity corresponds to mean Mach numbers of 0.4, 1.8 and 2.9 in the warm, intermediate, and cold phases. We examined the effect of mean density on the velocity dispersion, and found that $\delta v \propto \bar{n}^{-0.77}$ overall, with slightly shallower slope for the warm gas alone. Our results show, additionally, that the Reynolds stress,

$\langle \rho v_x \delta v_y \rangle$, varies with mean density $\propto \bar{n}^{-1.1}$. We find that the in-plane components of the velocity dispersion exceed the component perpendicular to the disk by about a factor of two.

5. *Magnetic fields:* For the present set of models, we have adopted initial conditions with a uniform vertical magnetic field of strength 0.26 μG. The MRI enhances the field by an order of magnitude, so that $\langle B^2 \rangle^{1/2}$ is typically $2-3$ μG late in the simulation. The field strength is similar (within $\sim 20\%$) in all three phases of gas, and there is no significant trend of field strength with mean simulation density $\bar{n}$. However, we find that the Maxwell stress, $\langle -B_x B_y/(4\pi) \rangle$, varies with mean density $\propto \bar{n}^{-0.4}$.

6. *Synthetic line profiles:* As a demonstration of the potential for employing simulations to interpret observational diagnostics, we have computed maps of synthetic line profiles from sample data cubes. We find that the line profiles are generally single-peaked (although in some cases would require two or three components if a standard Gaussian fitting scheme were performed). In no case did we identify two distinct velocity components, even though there are distinct cloud structures present along many lines of sight. Because turbulence has a smooth power spectrum, this kind of overlap in velocity space is inevitable.

Our results have several interesting implications for interpreting ISM observations, and it is also interesting to compare with recent numerical and theoretical work on the ISM and on MRI dynamics. We conclude by discussing these connections.

3.4.2 The Multiphase MRI and Saturated-State Turbulence

High levels of turbulence are observed both in the atomic gas of the Milky Way, and in that of external spiral galaxies, and it has been suggested that the MRI could be an important contributor to this turbulence, especially in the outer parts of galaxies where there is little star formation. Our models are the first (to our knowledge) to address this issue directly with an appropriate physical model – namely, one that admits two stable thermal phases, such that the MRI must develop in a cloudy medium with density contrasts of 100 between clumps and diffuse gas. While the turbulent velocity that develops in our fiducial model with mean density $\bar{n} = 1$ cm^{-3} is relatively modest, the scaling of the turbulent amplitude with $\bar{n}$ is quite steep, such that $\delta v \sim 8$ km s^{-1} is predicted when $\bar{n} = 0.2$ cm^{-3}.

The scaling of turbulent velocity dispersion with mean density indicates that MRI may play a significant role in the outer regions of the galaxy. Beyond the point in the Milky Way where the stellar surface density drops, the gas scale height rapidly increases, and the volume density correspondingly decreases; this sort of disk flaring is also seen in external galaxies. In the Wolfire et al. (2003) Milky Way model, for example, $\bar{n}$ falls below 0.2 cm^{-3} at $R = 15$ kpc. The outer-galaxy pressure in the Wolfire et al. (2003) model is nevertheless high enough for cold-phase gas to be present, so that if it were *not* turbulent, then a thin gravitationally unstable layer would develop.[1] Our results suggest that the MRI could be maintaining high-amplitude turbulence, and hence suppressing star formation, in the far outer Milky

[1]For a cold layer without turbulence, the value of the Toomre Q is < 1.5 (the threshold for instability) for $R\Sigma > 12$ kpc $\times 1 M_\odot$ pc^{-2}, where Σ is the gas surface density. Wolfire et al. (2003) show that cold gas is expected to be present at all radii out to 18 kpc. Since Σ is estimated to exceed $3 M_\odot$ pc^{-2} inside this radius, even if only 20% of the gas is in the cold component, the layer would be gravitationally unstable.

Way and other spiral galaxies. We note that the increase in scale height is necessary for this to hold; since the minimum MRI wavelength $\propto \bar{n}^{-1}$, MRI-driven turbulence can only be sustained in a sufficiently thick disk.

Even in the inner disk, our results suggest that MRI may be a significant contributor to turbulence in the ISM. At a mean inner-Galaxy (R < 10 kpc) midplane density of $\bar{n} = 0.6$ cm^{-3} (Dickey & Lockman 1990; Wolfire et al. 2003), our results would predict $\delta v \approx 4$ km s^{-1}. Away from the midplane where the density drops, the turbulent amplitudes would increase. The mean inner-disk vertical magnetic field strength may also be somewhat larger than the fiducial value we have adopted (Han, Manchester, & Qiao (1999) obtained $\langle B_z \rangle = 0.37$ μG from pulsar observations), which would tend to increase the amplitude of the turbulence. A more extensive parameter survey – allowing for disk stratification, varying scale height, and differing initial field strengths and distributions – is needed to quantify more fully the expected contribution from MRI to turbulent amplitudes in the ISM. Another important question is whether MRI development could be quantitatively altered by interaction with large-scale perturbations driven by supernovae or spiral shocks. We defer consideration of this interesting issue to future work.

Direct comparisons between simulations and observations regarding levels of turbulence and magnetic field strength as a function of local parameters would be very useful. Unfortunately, observations at this time do not permit such comparisons to be made. HI velocity dispersions in the Milky Way can only be measured within $\sim$ 1 kpc of the Sun (e.g. Lockman & Gehman (1991); Heiles & Troland (2003)). In external near-face-on galaxies, observed (vertical) velocity dispersions combine both turbulent and thermal contributions, and these values do not vary secularly with galactic radii (although dispersions are significant) even well beyond the optical disk (see §1). Magnetic field strengths in the Milky Way beyond ~ 10 kpc have not been

measured directly (i.e. with Faraday rotation; see e.g. Han, Ferriere, & Manchester (2004)). For both the Milky Way and external galaxies, one may use synchrotron emission (Beck 2004) to obtain the product of the magnetic and cosmic ray energy densities as a function of galactic radius, but since the equipartition assumption need not be satisfied everywhere, this does not yield a B-field strength except locally, where electron cosmic-ray and gamma-ray observations can be made. Milky Way outer-galaxy field strengths of 2-3 μ G are consistent with synchrotron/cosmic ray models of Strong, Moskalenko, & Reimer (2000).

The scalings we find for MRI amplitudes show interesting differences from those obtained with single-phase gaseous media, in previous adiabatic and isothermal simulations. In the shearing-box models of HGB1, HGB2, and Sano et al. (2004), all of the measures of turbulence scale together – i.e. $\langle B^2 \rangle \propto \langle -B_x B_y \rangle \propto \langle \rho (\delta v)^2 \rangle \propto \langle \rho v_x \delta v_y \rangle$. For simulations with net vertical magnetic flux, HGB1 further reported that these stresses and energy densities scale $\propto L_z \Omega v_{A,z}/c_s^2$, where $v_{A,z}$ and c_s are the initial Alfvén speed and sound speed, respectively. Sano et al. (2004), on the other hand, identify a scaling of stresses $\propto v_{A,z}^{3/2}$ in the mean Alfvén speed, and also demonstrate that the pressure dependence of the saturated-state stresses are very weak.

While we have not surveyed cases with differing magnetic field strengths, our models at varying mean density have varying $v_{A,z}$. At fixed mean B_z, the single-phase medium simulations cited above would predict scalings $\propto \bar{n}^{-1/2}$ or $\propto \bar{n}^{-3/4}$ for $\langle B^2 \rangle$, $\langle \rho (\delta v)^2 \rangle$, and the stresses. For our cloudy-medium simulations, we in fact find that $\langle B^2 \rangle$ is nearly independent of $\bar{n}$, while other scalings in our models are either in the same range as the single-phase predictions (i.e. $\langle \rho (\delta v)^2 \rangle \propto \bar{n}^{-0.54}$ and $\langle -B_x B_y \rangle \propto \bar{n}^{-0.4}$), or slightly steeper ($\langle \rho v_x \delta v_y \rangle \propto \bar{n}^{-1.1}$). Interestingly, 3D MRI simulations in radiation-dominated disks (Turner et al. 2003), which like our models

contain strong density contrasts, also show a steep dependence of the stress $\propto v_{A,z}^2$.

The reason for the difference between single-phase and cloudy-medium results for saturated-state $\langle B^2 \rangle$ scalings is not yet clear, but the lack of dependence on $\bar{n}$ in our models suggests that local, rather than global, properties of the gas determine the field strength that develops. The densities in the diffuse phase and in the dense phase are similar for all our models; only the filling factor of cold clouds differs appreciably. If the saturated-state field strength depends on the reconnection rate, and this depends on local gas densities and field geometry, then the fact that these properties are the same in all our two-phase models might explain the lack of dependence of $\langle B^2 \rangle$ on $\bar{n}$. Our isothermal model, which has less-kinked magnetic field, and typical (log) densities midway between $\log(n_{warm}) \sim -1$ and $\log(n_{cold}) \sim 1$, indeed has saturated-state values of the RMS field strength 20-50% higher than the standard run (3.5 μG in the isothermal model, compared to 2.4, 2.7, and 2.9 μG in the F, G, and H phases for the standard run). Further study, with particular focus on the rate and spatial distribution of reconnection, is needed to clarify this issue.

While the saturated-state magnetic field strength depends on a balance between MRI-driven amplification and (numerical or true resistive) dissipation, the saturated-state velocity dispersion depends on a balance between MRI driving and losses in shocks, compressions, and (numerical or true viscous) shear dissipation. Since turbulent velocities are similar in all the gas components, while the mass is concentrated in the cold clouds, in Paper I we proposed that the cloud collision time may be a good proxy for the kinetic energy dissipation time. The kinetic energy dissipated per unit time per unit mass is then $\dot{\mathcal{E}}_{diss} \sim (\delta v)^3 \bar{\rho}/(r_{cl}\rho_{cl})$, where r_{cl} is a cloud size and $\rho_{cl} \approx \rho_{cold}$ is the gas density within clouds. The kinetic energy input rate per unit mass due to MRI is an order-unity constant times $\Omega\langle -B_x B_y \rangle/(4\pi\bar{\rho})$. Balancing inputs with dissipation, and using $\langle -B_x B_y \rangle \propto \bar{\rho}^{-0.4}$ from our simulations,

this predicts a scaling for the saturated-state velocity dispersion $\delta v \propto \bar{\rho}^{-0.8}$. This prediction indeed agrees well with the velocity dispersion scaling measured directly from our simulations, $\delta v \propto \bar{\rho}^{-0.77}$. Of course, this scaling cannot continue to arbitrarily low density, because the MRI becomes stabilized if the wavelength ($\propto 1/\sqrt{\rho}$) exceeds the height of the disk.

In previous analytic work on magnetized cloud-cloud collisions Clifford & Elmegreen (1983) argued that effective cloud cross sections should vary $\propto (\bar{\rho}\delta v)^{-2/3}$. Although we do not measure this effect directly, it would not be expected to change our results significantly. Taking this into account for r_{cl} in the above analysis, the predicted power-law scaling exponent for δv with $\bar{\rho}$ changes by only 0.02.

3.4.3 Structure and Thermodynamics of the Atomic ISM

As noted above, our results show only minor differences between typical magnetic field strengths in gas of different phases, with the cold medium having slightly higher B. If flux were frozen to the gas, and cold clouds contracted isotropically out of the warm ISM due to TI, then the field strengths would differ by a factor 20 between diffuse and dense phases. Evidently, however, this is not the case: observationally, Heiles (2004) reports the B-fields in cold atomic clouds are no stronger than in the diffuse ISM overall. Our models are consistent with this result, in part because clouds in fact do not condense isotropically (but instead preferentially gather material along field lines), and in part because field lines can diffuse relative to matter (in our models, this is purely numerical, but turbulent diffusion is likely to play the same physical role).

Synthetic line profiles of the sort we have computed are potentially of great value in interpreting observations of the ISM, and in particular, the emission and absorption profiles of the 21 cm hydrogen line. Ensemble properties of the atomic

ISM, including the turbulent velocity dispersion for the cold gas separately, can be unambiguously obtained from observed position-velocity data cubes. Our results illustrate the difficulty, however, in discerning detailed (local) structural properties of the ISM directly from line profiles, due to overlapping in velocity space (cf. Ostriker, Stone, & Gammie 2001). Fortunately, recent work has demonstrated that analysis techniques calibrated using simulations can be used to extract fundamental statistical properties such as power spectra from CO observations of turbulent molecular clouds (e.g. Brunt et al. (2003); Heyer & Brunt (2004)), and it will be interesting to test whether the same holds true for HI gas.

What do we conclude regarding the dynamics/thermodynamics connection in the turbulent atomic ISM? As alluded to in §1, recent observations (Heiles & Troland 2003) have suggested that at least 30% of the HI gas at high latitudes (where blending due to galactic rotation is minimized) is in the thermally-unstable regime ($T = 500 - 5000$ K). Another 30% of the HI mass at high latitudes is estimated to be warm, thermally-stable gas.[2] Interestingly, we find that in our simulations, the warm and thermally-unstable gas mass fractions are also always very similar. In our models, the warm+unstable mass fraction only approaches 50% for the lowest-$\bar{n}$ case; at $\bar{n} = 0.67\mathrm{cm}^{-3}$, the warm+unstable gas comprises 30% of the total mass. However, except at the lowest $\bar{n}$, the turbulent amplitudes in our models are also somewhat lower than in the real ISM, so in part the lower warm+unstable fractions we find may owe to lower rates of turbulent dissipation. In addition, as discussed in §3.6, because our numerical method is non-conservative, a significant fraction of the input turbulent energy from the MRI is lost without being thermalized. Our

[2]At low latitudes, however, there is a very strong peak in the total gas column at $T \approx 8000 - 9000$K in the Heiles & Troland (2003) data, suggesting that midplane gas may be much more likely to be in thermal equilibrium.

method therefore underestimates the heating rate. This may be especially true in high density regions where the magnetic field curvature is large, so that the current density $\mathbf{J} = \nabla \times \mathbf{B}$ is large, and the resistive heating $\propto |\mathbf{J}|^2$ should also be large. We intend to explore this issue in future work incorporating explicit resistivity, also comparing with results using a conservative algorithm to update the energy equation.

Overall, our results are consistent with the recent work of Audit & Hennebelle (2005), who performed high resolution 2D simulations of a converging flow in which turbulence develops, using a cooling function very similar to ours. The temperature and density PDFs from their models are qualitatively similar to ours, in particular showing evidence for the existence of a two-phase medium even in the most turbulent case. Similar to our results, they found that the proportion of thermally-unstable gas increases with the amplitude of turbulence. For their least turbulent model, about 10% of the gas was thermally unstable, while this fraction increased to 30% in models with larger turbulent amplitudes.

Other recent work, based on simulations that include modeled effects of star formation via prescriptions for OB star heating (e.g. Vázquez-Semadeni, Gazol, & Scalo (2000); Gazol et al. (2001); Vázquez-Semadeni et al. (2003)) and supernovae (e.g. Rosen & Bregman (1995); Korpi et al. (1999); de Avillez (2000); Wada, Spaans, & Kim (2000); Wada & Norman (2001a); Wada (2001b); Balsara et al. (2004); Mac Low et al. (2005)), have found significant fractions of gas in the unstable phase, and many have advocated for a shift away from the classical two- or three-phase medium concept towards more of a "phase continuum" description. However, the former set of models have energy inputs from "star formation" in cold atomic gas (rather than in self-gravitating molecular clouds), which likely leads to overestimating the amount of thermally-unstable gas. The latter models have not included

low-temperature cooling, so no cold phase can form. Thus, it is not yet clear whether realistic models incorporating turbulence driven by star formation would indeed produce an extended, featureless continuum of temperatures, or whether they would yield bimodal distributions similar to those we have found with solely MRI-driven turbulence.

We believe that, given the observed turbulent amplitudes ($\sigma_v \sim 10$ km s^{-1}) and characteristic spatial scales (the disk thickness $H \sim 100$ pc) for the atomic ISM, quasi-two-phase distributions are inevitable. The heating time $\sim H/\sigma_v = 10^7$ yr is a factor of a few longer than the cooling time in gas at densities $\lesssim 1\mathrm{cm}^{-3}$ (see eq. [5] of Paper I or eq. [4] of Wolfire et al. (2003)), so that moderate but not extreme departures from thermal equilibrium can be expected in diffuse gas. In dense gas, cooling times are very short, so thermal equilibrium must hold, but typical order-unity variations in pressure from sonic-level turbulence can lead to moderate local density and temperature variations. Future work will be able to determine whether, with realistic turbulent amplitudes and fully-captured energy dissipation, thermal distributions from models can indeed match those from HI observations, or whether additional heat sources are required.

Acknowledgments

We are grateful to Charles Gammie, Woong-Tae Kim, Jim Stone, and Mark Wolfire for valuable discussions, and Yen-Ting Lin and Jonathan McKinney for helpful technical advice. The manuscript has also benefited from a thoughtful and detailed report prepared by an anonymous referee. This work was supported in part by grants NAG 59167 (NASA) and AST 0205972 (NSF). Some of the computations were performed on the Tungsten cluster at NCSA, and others were performed on the CTC cluster in the UMD Department of Astronomy.

Chapter 4

Models of Vertically Stratified Two-Phase ISM Disks with MRI-driven Turbulence

Abstract

We have performed vertically stratified simulations of the ISM, which account for galactic shear and magnetic fields, as well as a radiative cooling function which admits two thermally stable phases of gas. This allows us to study the magnetorotational instability (MRI) in the presence of a two phase medium, in a stratified disk. With these simulations we can begin to address the issue of why the ISM has the vertical distribution that is observed, and how this distribution is affected by turbulence driven by the MRI. We generally find that the cold component of the ISM sinks quickly to the mid-plane of the disk, increasing the local density to approximately 3 cm^{-3}. The turbulent velocity amplitudes of the cold medium are around $1.0 - 1.5$ km s^{-1}, while turbulent magnetic fields are $2 - 3$ μG. There are significant amounts of unstable gas, but the impact of the cooling function on

the thermal structure of the gas can not be ignored. There are two distinct peaks representing high density cold clouds, and a low density, warm ambient medium, in the density and pressure PDFs. The inner, primarily cold disk is magnetically supported. The support of the warm medium at high z is primarily by thermal or magnetic pressure, and the regions in which one of theses dominates over the other is dependent on the strength of gravity.

4.1 Introduction

The classical picture of the ISM began to take shape with Field's work on thermal instability (1965), and subsequently the realization that the ISM could exist in two distinct stable phases in pressure equilibrium (Field, Goldsmith, & Habing 1969). McKee & Ostriker (1977) argued that supernovae (SNE) are the main agent of destiny in the ISM, allowing for variations in pressure, driven turbulence, and a hot component formed by SNE blast waves which overrun a significant fraction of the volume. The validity of this model is still being scrutinized today by both observers and theoreticians. For understanding the ISM's thermodynamics, perhaps the most important development in more recent years is that both observations and simulations have found large fractions of gas to exist at temperatures which are thought to be thermally unstable. This calls into question whether or not a two or three phase model of the ISM is valid, and more generally how thermal and dynamical processes interact in the ISM.

Surveys of the HI 21cm line have shown that the ISM is very turbulent. Typical turbulent velocities are found to be approximately 7 km s^{-1} (Heiles & Troland 2003; Mohan, Dwarakanath, & Srinivasan 2004). As mentioned above, in the traditional picture of the ISM the source of turbulence is attributed to SNE (McKee & Ostriker

1977). Many simulations have been performed which explore the effects of SNE on the ISM, and the methods used for including star formation can be quite complex (e.g. de Avillez & Breitschwerdt (2004, 2005)). Most simulations have looked only at SNE rates equal to or above what is thought to be typical of the Milky Way. However, Dib, Bell & Burkert (2005) find that for SNE rates lower than half of the mean Galactic rate, the velocity dispersions fall short by a factor of 2-3 compared to typical observed values. Since low turbulence disks containing cold gas are susceptible to violent gravitational instabilities, this suggests another source of turbulence may be needed to self-consistently explain ISM conditions in the outer Milky Way where SNE are rare.

Various extragalactic observations have also implied that sources of turbulence other than SNE may be present. The ISM is found to be turbulent regardless of whether an active star forming region is nearby, (e.g. spiral arm/interarm regions have indistinguishable HI velocity dispersions in the galaxy NGC 1058 (Dickey et al. 1990)), and in particular turbulence levels in outer galaxies appear comparable to inner galaxies, even though star formation rates drop off steeply (van Zee & Bryant 1999).

These results have led us to explore another of the physical mechanisms which has potential to drive turbulence in the ISM. Perhaps the most viable in the outer parts of galaxies (where self-gravity is weak) is the magneto-rotational instability (MRI). The MRI may also contribute significantly in inner galaxy regions. In the past decade the MRI has been studied extensively in the context of accretion disks surrounding compact objects and protostars. The MRI generates turbulence in magnetized, shearing, disk systems, which leads to the transport of angular momentum outward through the disk allowing matter to accrete on to the central object. Galactic disks also meet the basic requirements for the MRI to be present: a weak

magnetic field and decreasing angular velocity with increasing radius. Sellwood & Balbus (1999) suggested that the observed turbulence in the outer disk may be driven by the MRI.

We have addressed this issue with direct numerical simulations, beginning with Piontek & Ostriker (2004) (hereafter Paper I; see Ch. 2), in which we performed 2D computations in the radial-vertical plane. These models were local, utilized a linear galactic shear profile and shearing-periodic boundary conditions, a radiative cooling function which allowed for a two phase medium, and magnetic fields. This combination permits us to study the MRI in the presence of a two phase medium. Our 2D models were extended to 3D in Piontek & Ostriker (2005) (hereafter Paper II; See Ch. 3), allowing us to study the late time evolution of the models, as 2D simulations do not (and cannot) yield saturated state turbulence, ending in the formation of the 'channel' solution. We found that at low densities the saturated state velocities can reach as high as 8 km s^{-1} in simulations with a mean density which is comparable to that found in the outer galaxy. Turbulent amplitudes were found to scale with density as $\delta v \propto \bar{n}^{-0.77}$.

In this paper we have extended the simulations of Paper II to include vertical gravity, thus allowing for stratification of the disk to develop. In these simulations the cold, high density clouds form and sink to the mid-plane, increasing the local mean density. Above the mid-plane the warm medium dominates, and turbulence driven by the MRI is very strong. We address a number of issues, some of which were not possible with the models presented in Paper II. What fraction of the ISM is found to exist in the unstable phase when turbulence is driven by the MRI? What is the vertical profile in a self-consistent turbulent system? We compare the turbulent amplitudes of stratified and non-stratified simulations, as well as the volume and mass fractions contained in the warm, unstable, and cold phases. We

address the issue of vertical support of the ISM, and answer the question of whether or not turbulence driven by the MRI can provide the necessary effective pressure to reproduce the observed scale height of the galactic disk. To explore dependence on parameters, we address these questions by performing three simulations which differ in the strength of gravity by a factor of sixteen.

In §4.2, we describe our numerical method and the parameters of our models. In §4.3 we present our results and analysis. In the final section we discuss the implications of our results, make comparisons, and present concluding remarks.

4.2 Numerical Methods and Model Parameters

We solve the equations of MHD in a local model representing sheared rotating flows, with additional terms for radiative heating and cooling, heat conduction, and gravity in the vertical direction:

$$\frac{\partial \rho}{\partial t} + \boldsymbol{\nabla} \cdot (\rho \mathbf{v}) = 0 \tag{4.1}$$

$$\frac{\partial \mathbf{v}}{\partial t} + \mathbf{v} \cdot \boldsymbol{\nabla} \mathbf{v} = -\frac{\boldsymbol{\nabla} P}{\rho} + \frac{1}{4\pi\rho}(\boldsymbol{\nabla} \times \mathbf{B}) \times \mathbf{B} + 2q\Omega^2 x \hat{x} - 2\boldsymbol{\Omega} \times \mathbf{v} + \mathbf{g}_{ext} \tag{4.2}$$

$$\frac{\partial \mathcal{E}}{\partial t} + \mathbf{v} \cdot \boldsymbol{\nabla} \mathcal{E} = -(\mathcal{E} + P)\boldsymbol{\nabla} \cdot \mathbf{v} - \rho\mathcal{L} + \boldsymbol{\nabla} \cdot (\mathcal{K} \boldsymbol{\nabla} T) \tag{4.3}$$

$$\frac{\partial \mathbf{B}}{\partial t} = \boldsymbol{\nabla} \times (\mathbf{v} \times \mathbf{B}) \tag{4.4}$$

All symbols have their usual meanings. The cooling function, $\mathcal{L} = \rho\Lambda(\rho, T) - \Gamma$, is adopted from Sánchez-Salcedo, Vázquez-Semadeni, & Gazol (2002), and is a piecewise power-law fit to the data of Wolfire et al. (1995). The heating rate,

$\Gamma = 0.015$ ergs s^{-1}, is spatially constant, modeling heating due primarily to the photo-electric effect of UV starlight on small grains and PAHs. This cooling function allows for two stable phases of gas, warm and cold, to coexist in pressure equilibrium. For the adopted cooling curve parameters, the minimum and maximum pressure for two stable phases of gas to exist in equilibrium in this model are about $P_{min}/k = 800$ K cm^{-3} and $P_{max}/k = 3100$ K cm^{-3}, respectively. Shear is described in terms of the dimensionless shear parameter $q \equiv -d\ln\Omega/d\ln R$, and q is set to one to model a flat galactic rotation curve. The conduction coefficient is set so that we can resolve the appropriate length scales of thermal instability, $\mathcal{K} = 1.03 \times 10^7$ergs cm^{-1} K^{-1} s^{-1}, not to represent the actual level of conduction in the ISM. Without conduction TI would be most unstable at the grid scale (see Paper I). We model the gravitational force $\mathbf{g}_{ext}$ as a linear function of height (assuming the gas scale height is smaller than most of the total mass), $\mathbf{g}_{ext} = -\tilde{\mathbf{g}} z \hat{z}$.

We use a modified version of the ZEUS MHD code (Stone & Norman 1992a,b) to integrate Equations (4.1) - (4.4) in time. ZEUS is a finite difference, operator split, time-explicit method for solving the equations of MHD. Shocks are captured via an artificial viscosity. Paper I gives a complete description of our numerical implementation of heating, cooling, and conduction, as well as code tests. The same basic methods were used in Paper II, for a version of the code parallelized with MPI. The primary difference between the models presented here and those of Paper II is the addition of the gravity term in Equation 4.2. We have made use of a density floor in order to prevent the time step from becoming prohibitively short, as well as the Alfvén limiter of Miller & Stone (2000). The density floor was set to 0.004 cm^{-3} , and $c_{lim} = 8$. The effect of the Alfvén limiter is essentially to limit the speed of MHD waves in a low density environment. The majority of the simulations presented here were run on the Thunderhead cluster at Goddard

Space Flight Center, while others were performed at the Center for Theory and Computation at the University of Maryland.

Shearing-periodic boundary conditions are used in the radial direction (Hawley & Balbus 1992; Hawley, Gammie, & Balbus 1995; Stone et al. 1996), while periodic boundary conditions are used in the azimuthal and vertical directions. Though the use of periodic boundary conditions in the vertical direction is not ideal, it offers some advantages compared to outflow boundary conditions, which we also explored. Depending on the implementation of outflow boundary conditions, they may or may not maintain the divergence free constraint of the magnetic field. Outflow boundaries can also create strong magnetic forces as magnetic flux is advected through the boundary and field lines are "cut" (Stone et al. 1996). Our simulations with outflow boundaries also lost significant amounts of mass over the course of the simulations.

The simulations are initialized with an isothermal disk in vertical gravitational equilibrium; thus the initial profiles are Gaussian. For our standard model, the initial temperature of the disk is 2500 K, the mid-plane density is 0.85 cm^{-3}, and the scale height, H, is 150 pc. The total gas surface density is therefore $\Sigma = 10\ M_{\odot}\ \mathrm{pc}^{-2}$. To explore the effect of gravity we also performed a high temperature, high gravity model, as well as a low temperature, low gravity model. The initial disk temperature in these two models was $10,000\ K$ and $600\ K$, respectively, with the same initial mid-plane density and scale height as the standard model [1], and hence the same value of Σ. We adopt $P_0/k = 2000\ K\ \mathrm{cm}^{-3}$ as the unit of pressure in the code; we use this value of P_0 to normalize the pressure in a number of the Figures. The values of the gravity constant are $\tilde{\mathbf{g}} = 1.8 \times 10^{-31}\mathrm{s}^{-2}$, $7.3 \times 10^{-31}\mathrm{s}^{-2}$, and $2.9 \times 10^{-30}\mathrm{s}^{-2}$. The central density and scale height were chosen to be generally consistent with

[1] After cooling is initialized at $t = 4$ orbits the temperatures and pressures in these three models evolve to be roughly the same.

estimated ranges near the Solar radius in the Galaxy. The two larger values of $\tilde{\mathbf{g}}$ bracket estimates near the Solar radius using $\tilde{\mathbf{g}} = 4\pi G\rho_{tot}$, for ρ_{tot} the combined (stars + gas) mid-plane density (Binney & Merrifield 1998). The smallest gravity model can be thought of as representative of the outer galaxy. The magnetic field is initially vertical, with a plasma beta parameter, $\beta = P_{gas}/P_{mag} = 100$. Random white noise perturbations are added at the 1% level to seed the MRI. Cooling is not turned on until t=4.0 orbits, just as the MRI modes begin to become non-linear. Most simulations last approximately 10 orbits, with one orbit equal to 240 Myrs. The size of the computational volume is $2H \times 2H \times 6H$, with $128 \times 128 \times 384$ grid zones, giving a resolution of about 2 pc.

In order to address the question of what supports the gas vertically in our disk models, and how much of each phase is present, we need a baseline for comparison. For this comparison we have performed (2D) simulations which do not include magnetic fields, and therefore are not turbulent. Cooling is initialized at t=0, and the gas quickly separates into two stable phases. The cold component settles to the mid-plane, with the warm gas found above and below the cold gas in pressure equilibrium with gravity. The warm and cold components are separated by a thin layer of unstable gas, and there is little mixing between the two stable phases. We performed a set of three non-turbulent simulations, varying the initial temperature of the disk and $\mathbf{g}_{ext}$, as in the turbulent models; all initial conditions other than β are the same as adopted in the turbulent models.

4.3 Results

4.3.1 Evolution

From t=0 to approximately t=4 orbits the disk is in pressure and gravitational equilibrium, and both heating and cooling are disabled until this time. This method of initialization prevents the creation of a very thin cold disk, as would occur if the cooling function were initialized at t=0. During these first few orbits the modes of the MRI begin to grow and strengthen from the small amplitude perturbations imposed in the initial conditions. At around t=4 orbits the modes of the MRI begin to saturate due to nonlinear interactions, at which point the cooling function is enabled. The disk then quickly evolves into a two-phase medium which is no longer in gravitational equilibrium. The heavier cold clouds quickly sink towards the mid-plane, but turbulence driven by the MRI serves to thicken the disk. Some of the largest turbulent amplitudes are seen during this stage as the channel flow forms, then quickly dissipates. A quasi-steady state is soon established, after which time the averaged mass fractions, turbulent velocities, magnetic field strengths, and other quantities are fluctuating, but remain roughly constant. In Figure 4.1 we show a volume rendering of density late in the simulation for our standard model at $t = 8$ orbits, and in Figure 4.2 we show slices through the computational volume of the field variables: density, pressure, velocity, and magnetic field. The MRI continues to drive turbulence throughout the duration of the simulation. Though these simulations are stratified, the overall character of these models appears to be quite similar to those presented in Paper II.

In the following sections we analyze the turbulent velocities, magnetic fields, pressure, and thermal structure of the gas. We discuss the time history of averaged

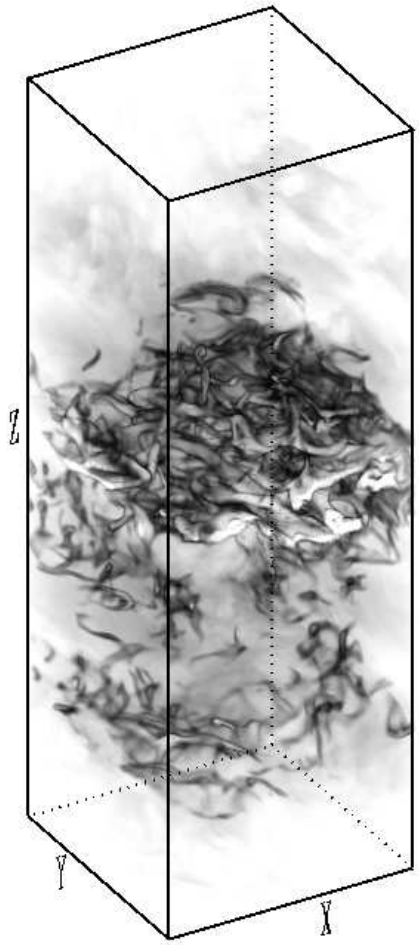

Figure 4.1: Volume rendering of density for the standard gravity run, at t=8 orbits.

quantities, as well as presenting probability distribution functions of thermal and magnetic pressure, temperature, and density. In addition, we analyze the vertical structure of our models, considering the question of how material is vertically supported. Throughout, we make comparisons among results of models with varying $\mathbf{g}_{ext}$.

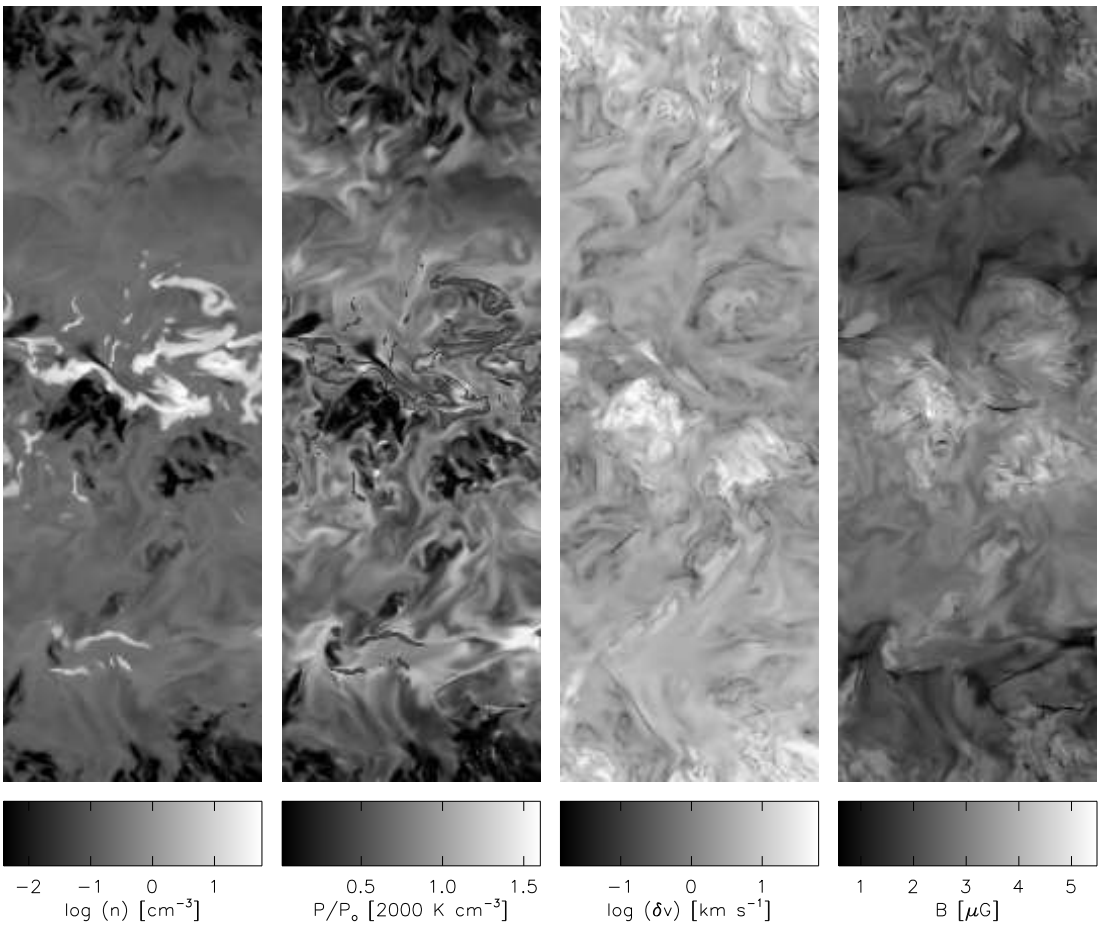

Figure 4.2: Slices through the computational volume of the field variables, at $t = 8$ orbits. From left to right: Log(ρ), Log($\mathcal{E}$), δv, and B.

4.3.2 Turbulent velocities

The mass weighted Mach numbers are plotted in Figure 4.3, from t=4-10 orbits for the standard run, as there is no interesting development prior to $t = 4$ orbits. The sound speed is computed individually for each grid point, and the galactic shear component is subtracted, so that the velocity is computed as $\delta v = \sqrt{v_x^2 + (\delta v_y)^2 + v_z^2}$. The saturated state Mach numbers for the warm, intermediate and cold phases of gas, averaged over orbits 7-10, are 0.5, 1.4 and 2.0. In Figure 4.4 we plot the corresponding mass weighted velocity dispersions for each of the three components; the

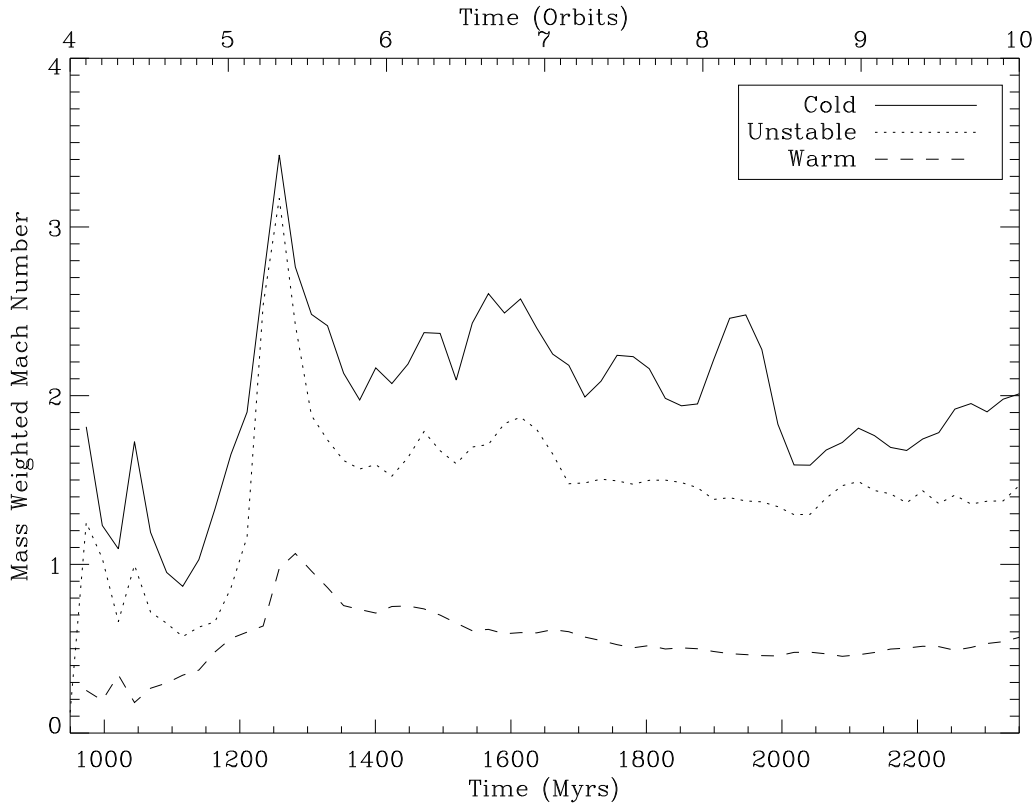

Figure 4.3: Volume weighted Mach numbers for the cold, unstable, and warm phases of gas, plotted against time from t=4-10 orbits. The time averaged Mach numbers over orbits 7-10 are 2.0, 1.4, and 0.5.

time averaged values are 3.7, 2.3, and 1.4 km s^{-1}, averaged over the same interval. As the MRI initially begins to develop, the channel solution is strong, and the largest velocities are observed. The peak volume averaged velocity dispersion is around 9 km s^{-1} in the warm medium. In the high gravity model, the mass weighted velocity dispersions are 5.1, 2.3, and 1.2 km s^{-1}, for the warm, intermediate, and cold phases, and in the low gravity model, 4.0, 2.5, and 1.4 km s^{-1}. There is therefore little difference in the velocity dispersions between the three models. For the standard model, Figure 4.5 shows the mass-weighted velocity dispersion profile in z for the warm, unstable, and cold components separately (i.e. $(\sum \rho \delta v^2 / \sum \rho)^{1/2}$ as a function of z), as well as for the combined medium. For the warm medium, δv generally increases with height, and reaches nearly 12 km s^{-1} near the boundary of

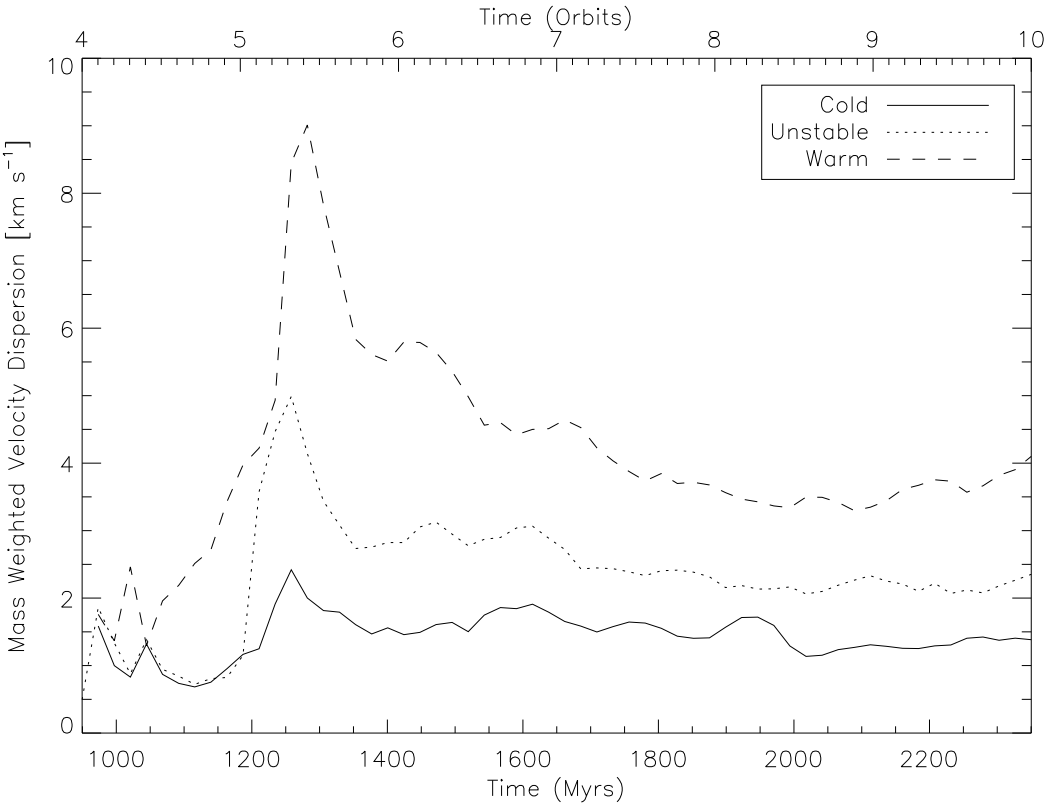

Figure 4.4: Mass weighted velocity dispersion for the cold, unstable, and warm phases. The late time averaged values for the warm, unstable, and cold phases are 3.7, 2.3, and 1.4 km s^{-1}.

the simulation domain.

We can compare the velocity dispersions of the stratified models to those of the unstratified models from Paper II. The total mass weighted velocity dispersions of the low, middle and high gravity models are 2.9, 2.7, and 3.0 km s^{-1}, and the mass weighted mean densities are 1.2, 2.1, and 5.5 cm^{-3}, respectively. From Paper II we found that the velocity dispersion should follow the relationship $\delta v \propto \bar{n}^{-0.77}$. So, based on the non-stratified model scaling, the velocity dispersion at the corresponding mean densities would vary from 2.3 km s^{-1} in the low gravity model, to 1.5 km s^{-1} in the standard model, to 0.72 km s^{-1} in the high gravity model. The values we find are roughly consistent with the results from the unstratified models, given the large range in mean density with z. However, in more detail we do not observe

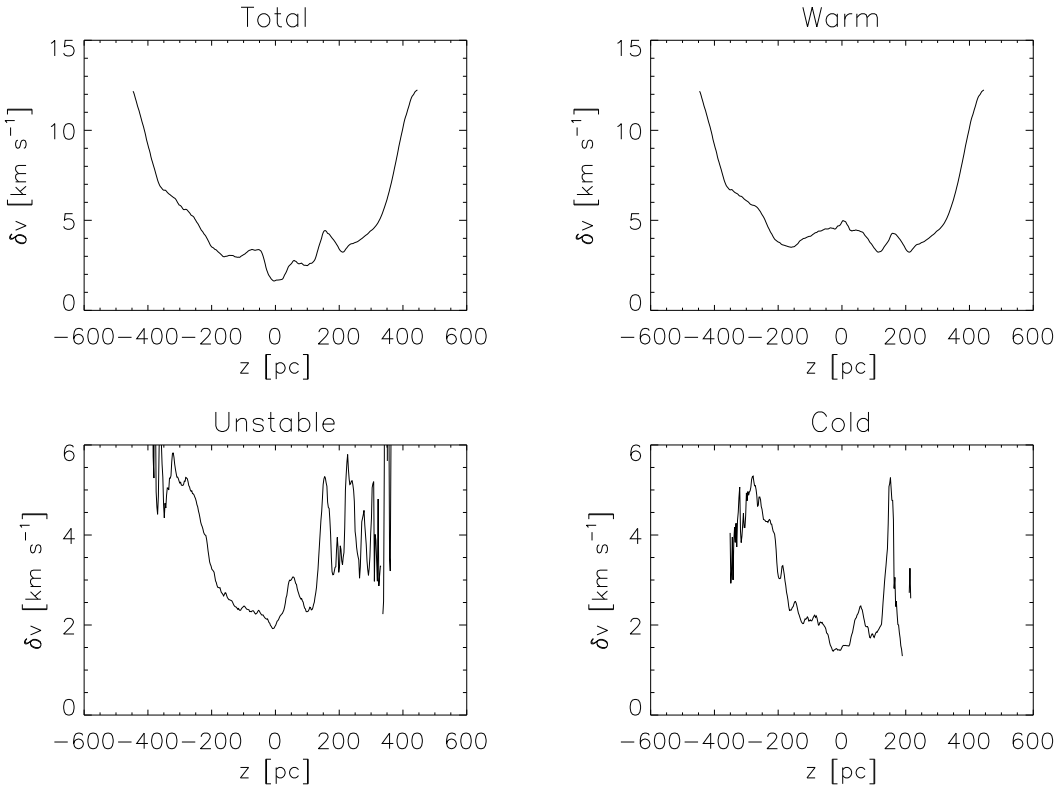

Figure 4.5: Profile of δv for the standard run, for the total as well as each thermal component.

any significant trends in velocity dispersion with the mean mass weighted density, or when comparing the velocity dispersions of the individual components. At high z, as pointed out in Paper II, it is expected that the velocity dispersion/density relationship will turn over at velocities comparable to the thermal speed in the warm gas. Thus, we do not expect velocity dispersions to significantly exceed 8 km s^{-1}, and based on Figure 4.5 this is the case.

The numbers presented here serve to illustrate the primary difference between these simulations and those of Paper II. In the non-stratified models of Paper II the three phases of the ISM were well mixed within the simulation domain, which lead to the result that the three phases of gas were found to have essentially the same turbulent velocities. In the current stratified simulations cold gas is only found

near the mid-plane, with the low density warm medium dominating the dynamics at higher latitude. Turbulent velocities are significantly higher in the low density high latitude gas, but this gas does not serve to drive comparably high turbulence levels near the mid-plane, where most of the cold medium is found.

4.3.3 Magnetic Fields

The initial field strength is 0.26 μG, and is vertical. The mass weighted magnetic field strength, $B = (B_x^2 + B_y^2 + B_z^2)^{1/2}$ is plotted in Figure 4.6, as a function of time. The MRI amplifies the initial field by a factor of about 10. The saturated state field strength is typically 3 μG, slightly higher in the cold medium, and slightly lower in the warm medium. Averaged over orbits 7-10, the mean field strengths in the warm, unstable, and cold phases are 2.4, 3.1, and 3.2 μG. In the low gravity model the field strength values are 2.7, 3.0, and 3.1 μG, and in the high gravity model we find slightly larger means of 2.7, 3.5, and 3.6 μG, respectively.

In Figure 4.7 we compute the PDF of the magnetic field strength at t = 4.5, 5.0, 7.5 and 10.0 orbits. The amplitude and breadth of the PDF grow with time. The maximum field strength increases to approximately 8 μG by the end of the simulation.

4.3.4 Distributions of Density, Temperature, and Pressure

In Figure 4.8 we plot the mass fractions of the three phases as a function of time, from t=4-10 orbits. By mass the cold medium is 59% of the total, with the unstable and warm media occupying 17% and 23% of the mass, averaged over orbits 7-10. By volume the warm phase occupies 91%, with the unstable phase about 7% and the cold phase about 2%. For comparison, in the high and low gravity models, the mass fractions of warm, unstable, and cold gas are (17,11,73)% and (22,17,60)%, re-

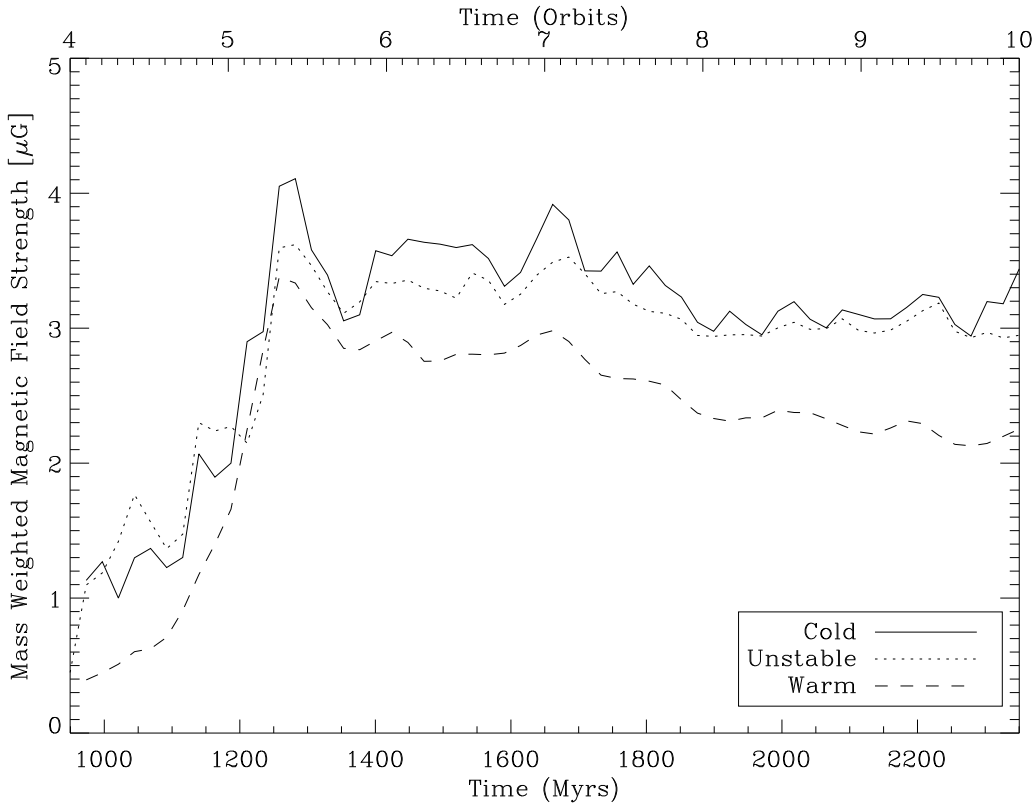

Figure 4.6: Mass weighted magnetic field strength as a function of time for t=4-10 orbits. Average over $t = 7 - 10$ orbits, the mean field strengths in the warm, unstable, and cold phases are 2.4, 3.1, and 3.2 μG.

spectively. The corresponding volume fractions are (94,4,2)% and (91,6,2)%. Thus, the proportions of mass in different phases appears fairly insensitive to $\mathbf{g}_{ext}$. We can contrast this with the results of the non-turbulent comparison models. For those models, the cold fraction was 81%, 86%, and 92% for the low, medium, and high gravity models, with the warm fraction making up the balance. Thus, turbulence considerably lowers the fraction of gas found in the cold regime.

In Figure 4.9 we plot the density PDF at $t = 4.5$, 5.0, 7.5, and 10.0 orbits for the standard model. These PDFs would seem to indicate the presence of two distinct phases of gas, as there is certainly a peak in both the volume and mass PDF at around $n = 0.1$ and $n = 10$ cm^{-3}. The minimum density reaches the artificial density floor of 0.004 cm^{-3}, while the maximum density can extend upwards of 400

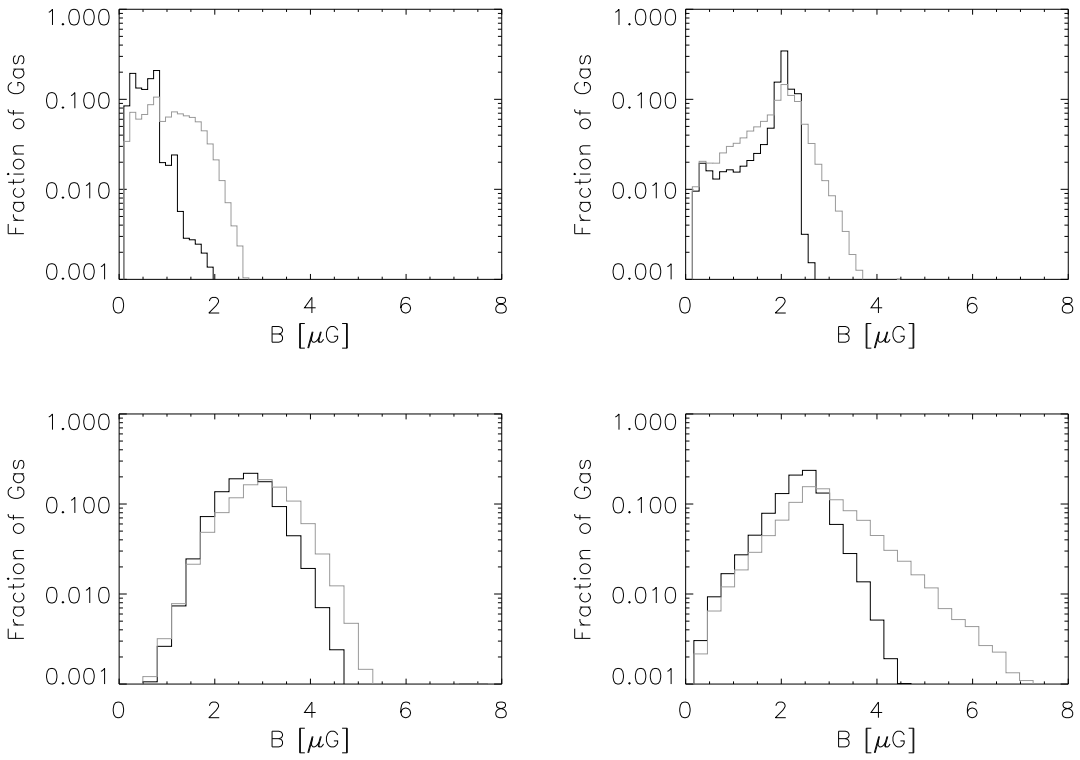

Figure 4.7: Volume weighted (dark line) and mass weighted (grey line) magnetic field PDFs for the standard run, at t=4.5, 5.0, 7.5 and 10.0 orbits.

cm^{-3}. There are some similarities and some differences of these PDFs as compared to those of the non-stratified models of Paper II. Except for the tail extending to low densities (due to gravitationally-imposed stratification), the PDFs are fairly similar. They both show a well defined peak at the location of the low density warm medium, and a broader peak at the high density cold medium.

In Figure 4.10 we plot the temperature PDFs at the same times as those presented in Figure 4.9. The high temperature peak is fairly well defined, especially at early times. This feature is broadened later in the simulation, and a small fraction of the gas exists at higher temperatures by about an order of magnitude as compared to the PDFs from Paper II. The minimum temperature is near 20 K, while the maximum extends as high as 125,000 K.

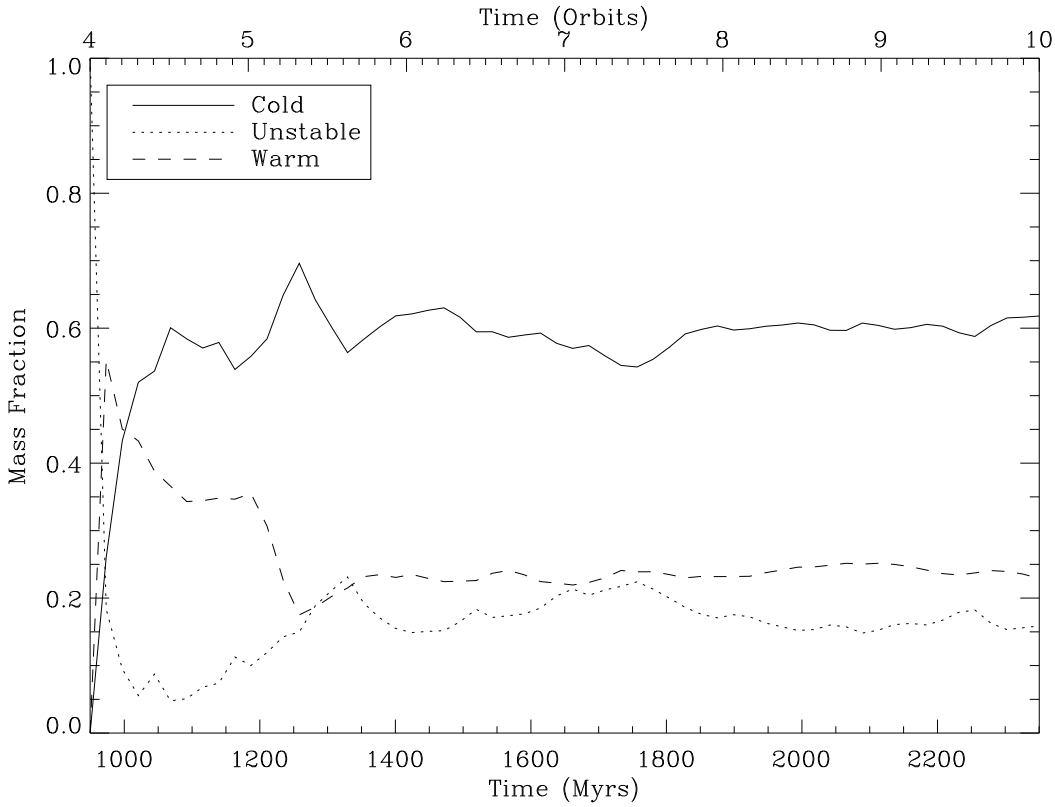

Figure 4.8: Mass fractions of the three phases of gas. Averaged over orbits 7-10, the warm, unstable, and cold phases contain 23%, 17% and 59% of the mass, respectively.

The pressure PDFs are shown in Figure 4.11, again at $t = 4.5$, 5.0, 7.5, and 10.0 orbits. The pressure PDFs extend to very low values in the saturated state, as low as $P/k = 10$ K cm^{-3}, and the maximum pressure is approximately $P/k = 8000$ K cm^{-3}, but only a very small fraction of mass exists at pressures this high. The maximum pressure for which a two-phase medium can co-exist in pressure equilibrium is $P_{max}/k = 3100$ K cm^{-3}; this is where the volume weighted PDF cuts off. Also, the mass weighted fraction of gas drops sharply below $P_{min}/k = 800$ K cm^{-3}, the lowest pressure for which a two phase medium can exist. The mass weighted pressures in the warm, cold, and unstable phases are shown in Figure 4.12. The mean mass weighted pressures, averaged over orbits 7-10, for the warm, unstable, and cold phases are $P/k = 1600, 1100$, and 1700 K cm^{-3}. So, although

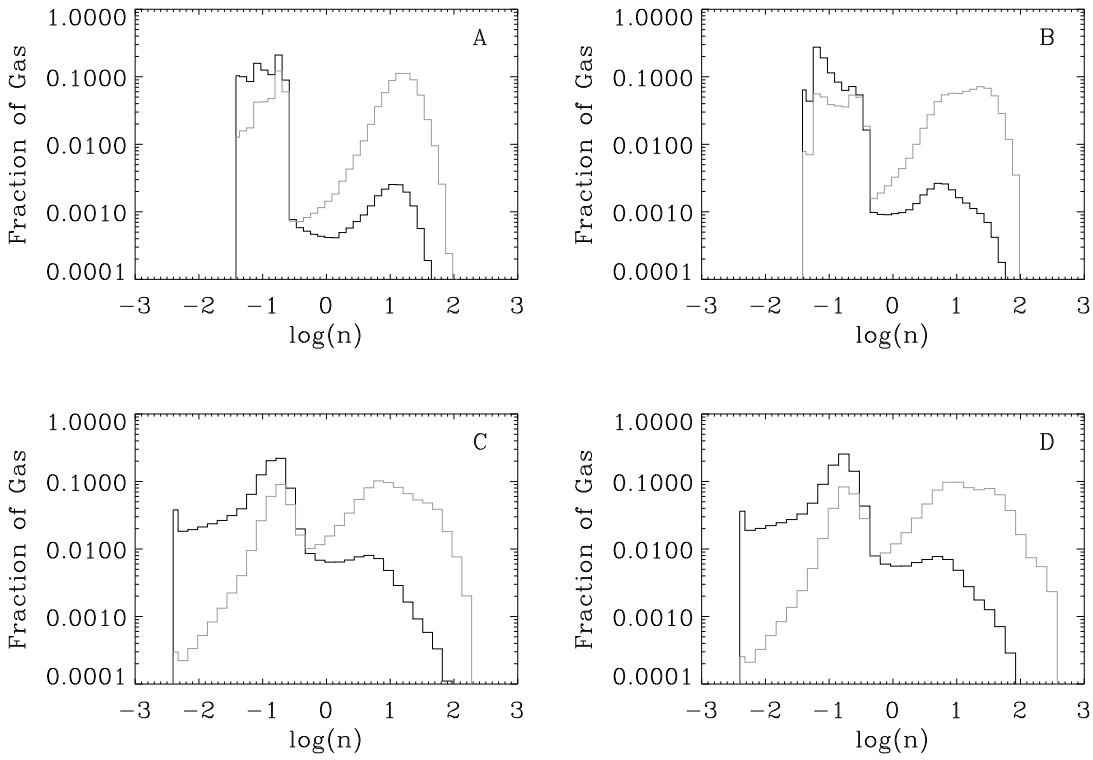

Figure 4.9: Volume weighted (dark line) and mass weighted (grey line) density PDFs for the standard run, at $t = 4.5$, 5.0, 7.5 and 10.0 orbits.

the overall pressure distribution is quite broad, the mean pressure in the warm and cold phases are approximately equal. In the high gravity run this is not quite the case. The mean warm, unstable, and cold pressures are $P/k = 1700, 1100$, and 2100 K cm^{-3}, and in the low gravity case $P/k = 1500, 1100$, and 1500 K cm^{-3}.

Scatter plots of density vs pressure are shown in Figure 4.13. The solid line is the equilibrium cooling curve, and contours of constant temperature are plotted at the transitions between different temperature regimes in the cooling function. Cold gas is defined to be below 141 K, warm gas above 6102 K, and unstable gas between these two temperatures. Gas at low temperatures cools relatively quickly, and is found to be very close to the thermal equilibrium curve. For the first orbit after the cooling function is enabled, during which turbulent amplitudes are relatively low,

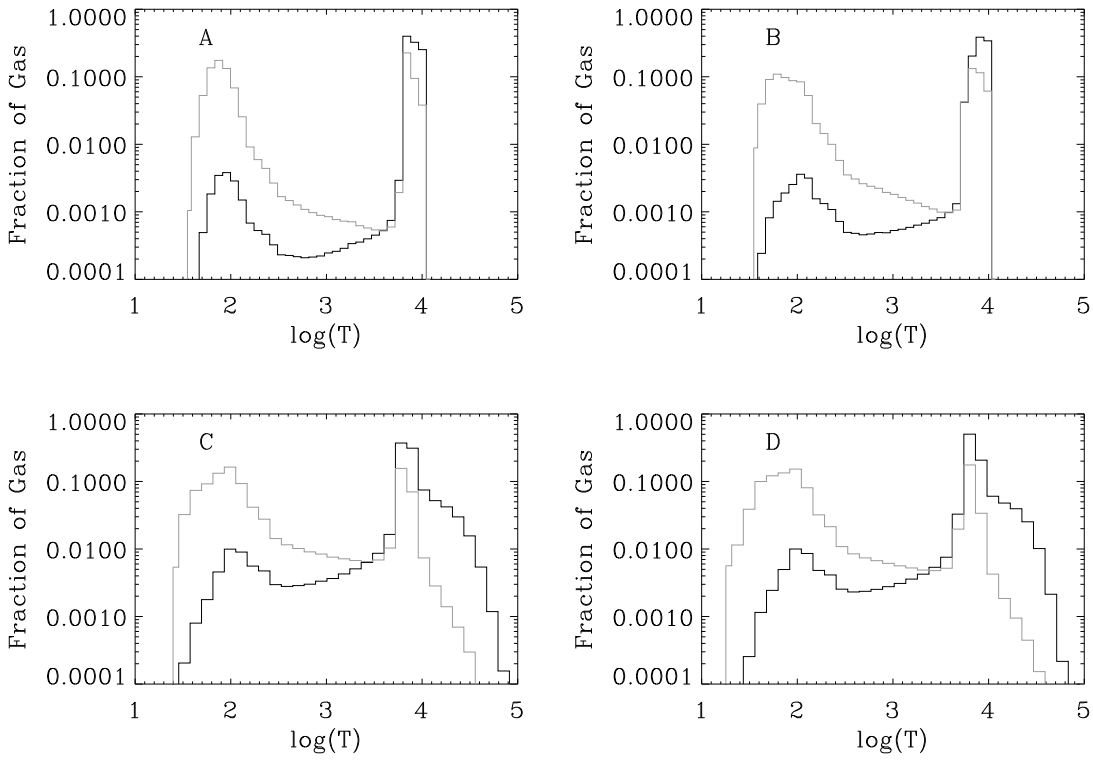

Figure 4.10: Volume weighted (dark line) and mass weighted (grey line) temperature PDFs for the standard run, at $t = 4.5$, 5.0, 7.5 and 10.0 orbits.

most of the gas is in thermal equilibrium in both the warm and cold phases. Later on turbulence drives significant fractions of gas out of thermal equilibrium. Gas at higher temperatures takes longer to cool and is typically out of equilibrium (but roughly follows the shape of the equilibrium curve).

4.3.5 Stratification of Density & Pressure; What supports gas vertically?

To address the issue of vertical support of the ISM, we first summarize results from our non-turbulent models that do not include MRI driven turbulence. Once the gas has settled, we can evaluate the total mass fractions and mass distributions of each phase. We find that for the low, middle and high gravity models, the cold

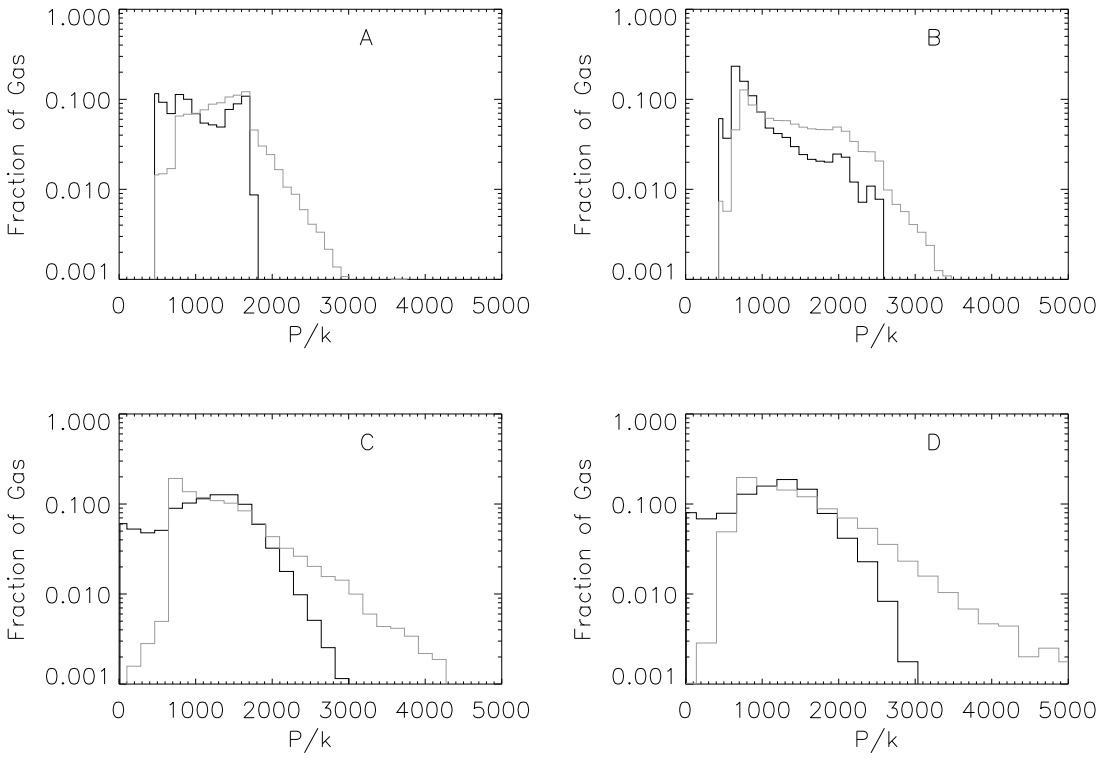

Figure 4.11: Volume weighted (dark line) and mass weighted (grey line) pressure PDFs for the standard run, at t=4.5, 5.0, 7.5 and 10.0 orbits.

mass fractions are 81%, 86%, and 92%, and warm mass fractions are 19%, 14%, and 7%. These fractions are consistent with what is expected for the minimum amount of warm gas in a two-layer hydrostatic equilibrium for a given total Σ and $\mathbf{g}_{ext}$ (see §4.4). The profile of the cold medium is approximately a truncated Gaussian, and the truncation occurs where the transition is made to the unstable and then warm phases. While the cold mass fraction is higher when gravity is larger, the cold disk thickness is smaller; the scale height decreases from 15 pc to 10 pc from the low to high gravity case. The transition between phases typically occurs at $P/k = 1200$ K cm^{-3}, i.e close to the minimum pressure for which cold and warm gas can coexist. The warm disk closely approximates a Gaussian, and has a scale height of 460, 240, and 120 pc in the low, mid, and high gravity models, respectively.

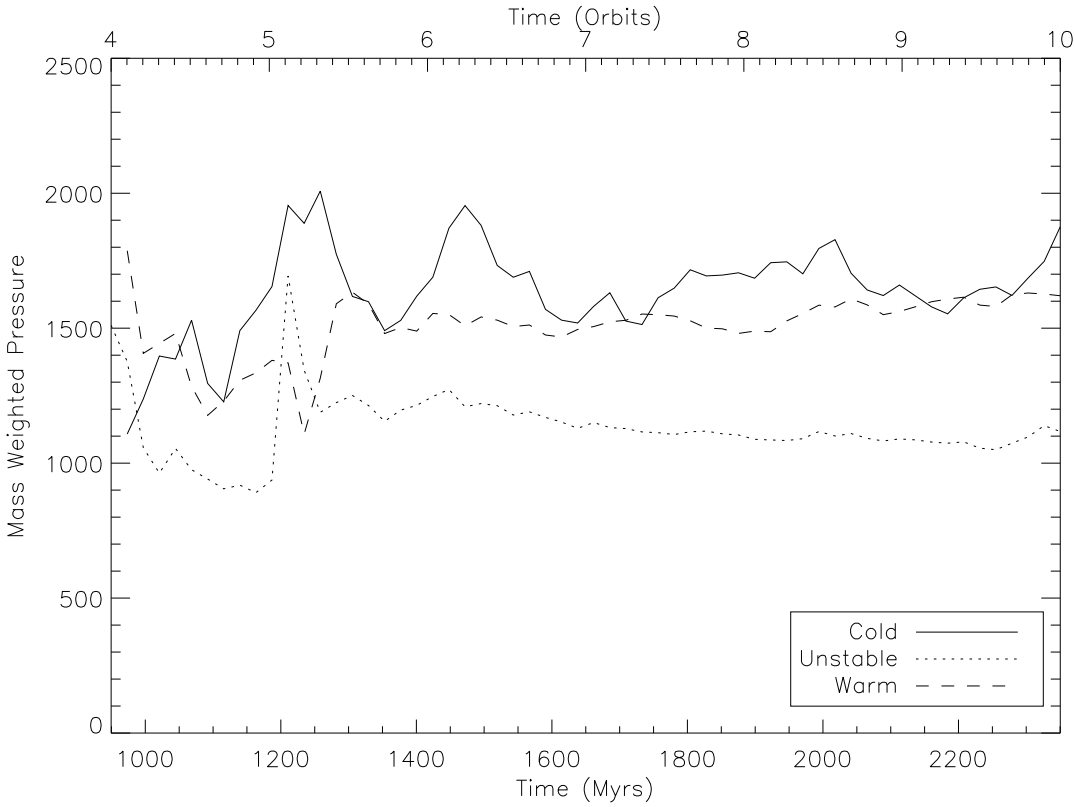

Figure 4.12: Volume weighted pressure as a function of time for the standard run.

These successive factors of 2 in the scale height are expected based on the successive factors of 4 from low to moderate to high gravity, since for an isothermal pressure-supported disk, $H = c_s/\sqrt{\tilde{\mathbf{g}}}$, where $\mathbf{g}_{ext} \equiv -\tilde{\mathbf{g}}z$. We can compare the scale heights of these non-turbulent models to those which include MRI driven turbulence.

Mass profiles for the three phases of gas as well as the total are shown in Figure 4.14 for our standard turbulent model. These profiles are computed by integrating the density in each component in x and y, as a function of z, dividing by the total number of zones in the x and y directions, and averaging over the last two orbits of the simulation. In the turbulent models, the scale height of the CNM is 40, 20, and 15 pc from low to high gravity. Turbulence from the MRI therefore increases the scale height of the cold medium by approximately 50-100% depending on the model.

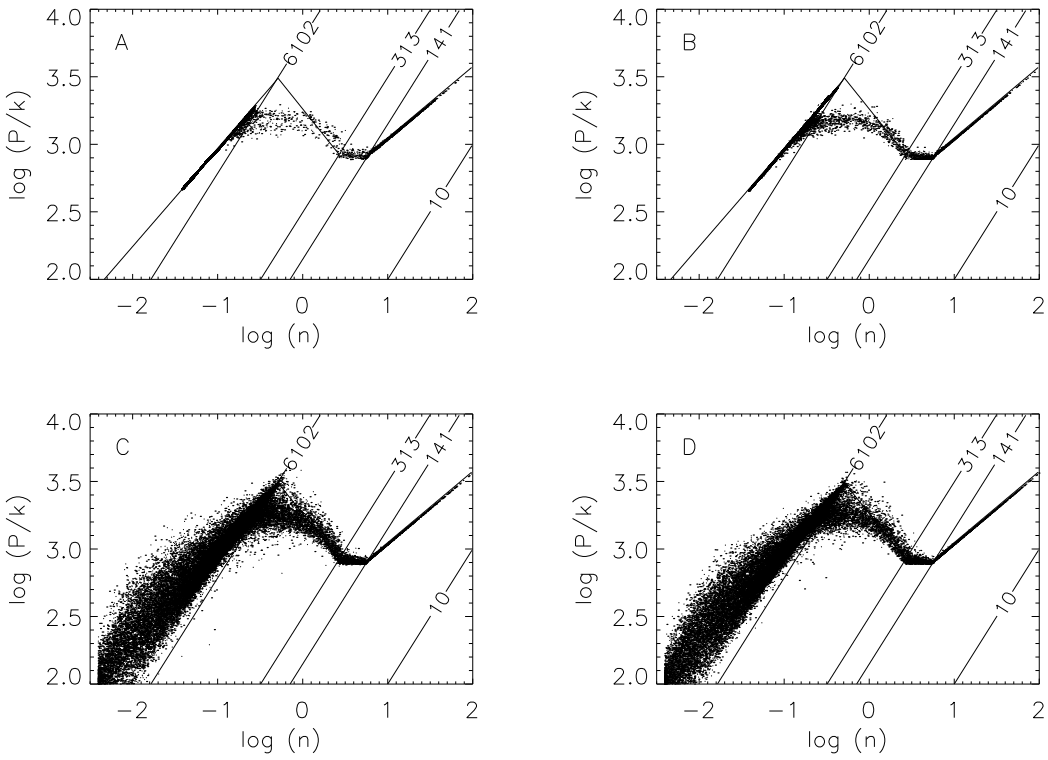

Figure 4.13: Scatter plots of density vs pressure for the standard run, at $t = 4.5, 5.0, 7.5$ and 9.9 orbits, Panels A, B, C, & D, respectively.

The profiles are not Gaussian, however, so these estimates are rough approximations only. The profile of the unstable gas is also non-Gaussian, but we estimate a scale height of the centrally peaked gas to be 90, 44, and 30 pc from the low to high gravity models. These values are roughly twice as large as the cold layer thickness. There is significant unstable gas at high latitude. For the low gravity case the warm medium is more or less evenly distributed vertically through the box, so we do not estimate a scale height. In the standard gravity model the WNM is also very far from Gaussian, but we can fit an approximate Gaussian with $H \sim 250$ pc to the profile at high latitude, which appears to be in equilibrium. For the high gravity case the scale height is again roughly 240 pc, and is more centrally peaked than the other models, but still non-Gaussian.

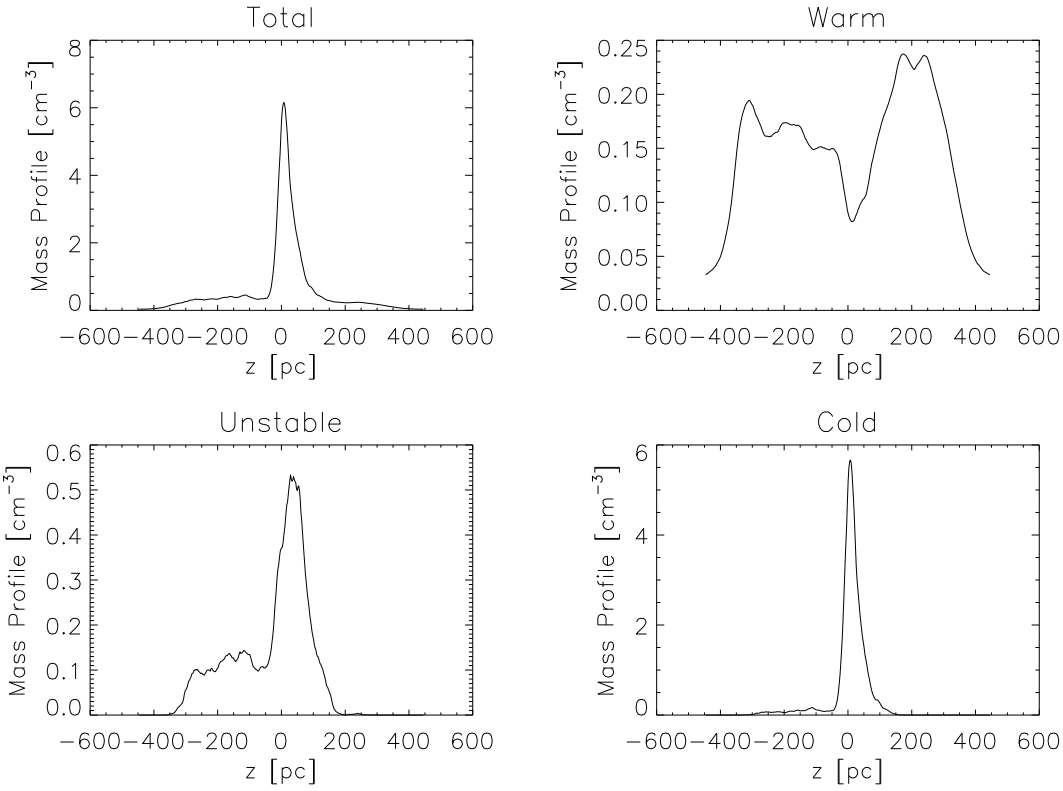

Figure 4.14: Volume weighted mass profiles for the standard run.

In Figure 4.15 we plot the typical density of the total mass, as well as the three components as a function of z for the standard run. The component typical densities are just the mean values in each phase at any z. The typical density in the warm medium is approximately $0.2 - 0.25$ cm^{-3}, and this decreases at higher z. In the unstable phase the typical density is around $1.5 - 2.0$, increasing somewhat towards the mid-plane and decreasing at higher z. For the cold medium the average density reaches as high as about 20 in the mid-plane, sharply decreasing to around 10 at higher latitudes. This is near the minimum possible density at which cold gas can be in thermal equilibrium (at P_{min}). There is about a factor of 100 separating the typical density in the warm and cold phases.

We next turn to what, physically, is responsible for these vertical mass profiles. By averaging the z component of the momentum equation in horizontal planes, and

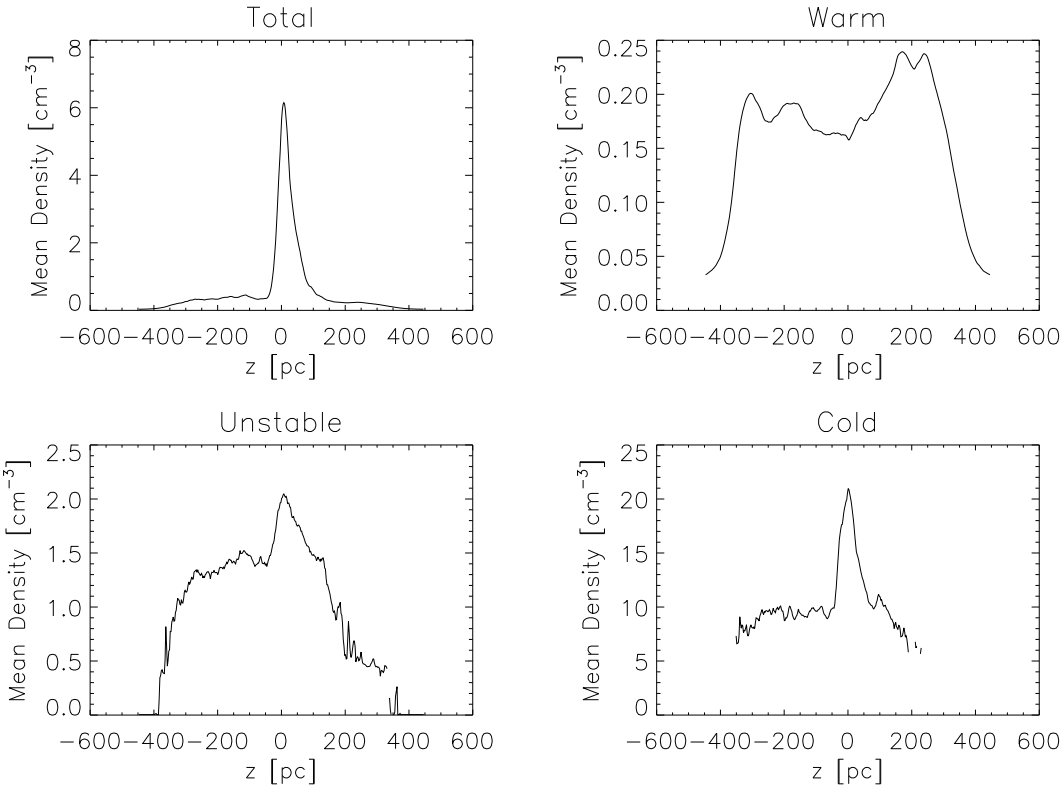

Figure 4.15: Profiles of the typical density at each height of each gas phase in the standard run.

making use of shearing periodic boundary conditions, we obtain

$$\left\langle \frac{\partial}{\partial t}\left(\rho v_z\right)\right\rangle = -\frac{\partial}{\partial z}\left\langle \rho v_z^2\right\rangle - \frac{\partial}{\partial z}\left\langle P\right\rangle - \frac{\partial}{\partial z}\left\langle \frac{B^2}{8\pi}\right\rangle + \frac{\partial}{\partial z}\left\langle \frac{B_z^2}{4\pi}\right\rangle - \left\langle \mathbf{g}_{ext}\rho\right\rangle \qquad (4.5)$$

In addressing the issue of the vertical distribution of the ISM, and the relative importance of thermal, kinetic, and magnetic terms in the above equation, we concentrate our analysis on the high gravity run. The pressure gradient terms in the high gravity run, averaged over the last two orbits, are in approximate balance with gravity. That is, the time derivative term is small. As the gravitational constant is reduced in the middle and low gravity models, a local quasi-equilibrium is less evident than in the high gravity case. To draw quantitative conclusions from these models, longer temporal baselines and larger simulation domains appear necessary.

The contributions to thermal, kinetic (i.e. ρv_z^2), and magnetic pressures for the

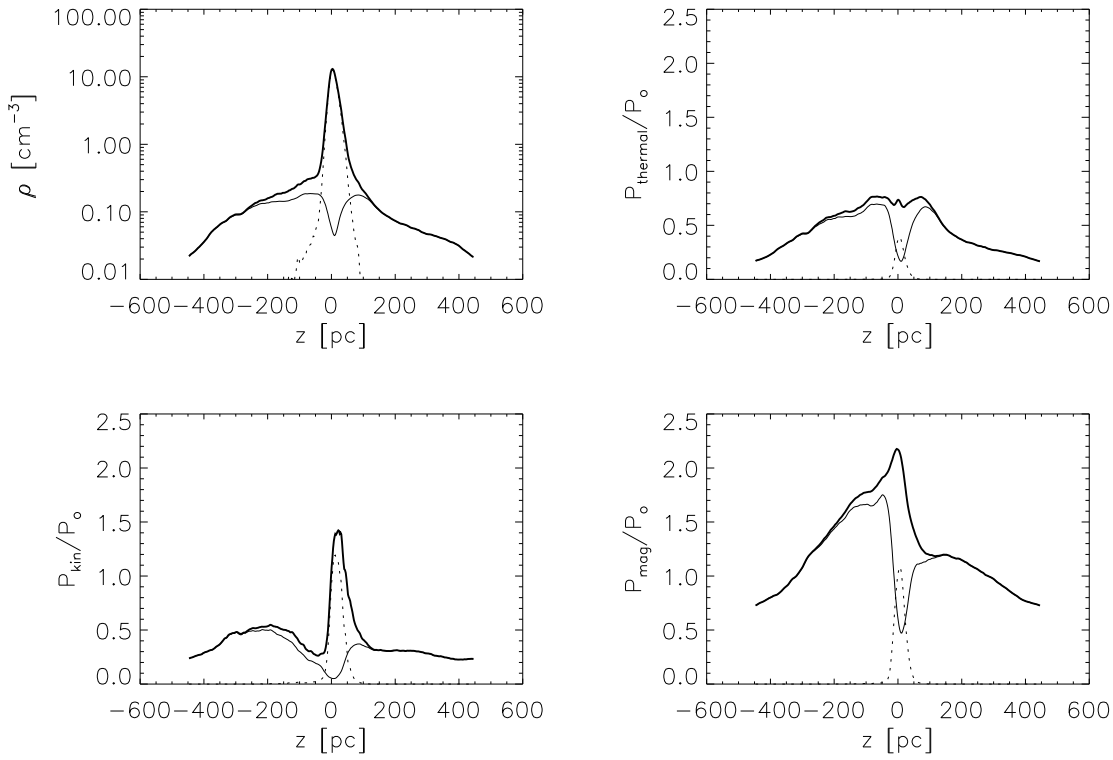

Figure 4.16: Density and pressure contributions from warm and cold phases for the high gravity run. The warm phase corresponds to the solid line, while the cold phase is shown as the dotted line. The thick solid line shows the total for the warm, unstable, and cold components combined.

high gravity run are plotted in Figure 4.16 for the warm and cold phases, along with the density profile. At each height, the contribution from each phase consists of the sum over zones in that phase, divided by the total number of zones. The warm medium dominates the mass profile at high z, and the cold medium dominates in the mid-plane. For the warm medium, the magnetic pressure is the largest of the three pressures, followed by thermal, and kinetic pressures, respectively. In the cold medium, the kinetic and magnetic pressures are approximately equal, while the thermal pressure is smaller by a factor of two or three. In Figure 4.17, we show the typical values of the same quantities as shown in Figure 4.16, again for the high gravity model. Similar to the standard gravity run, the typical density of the cold

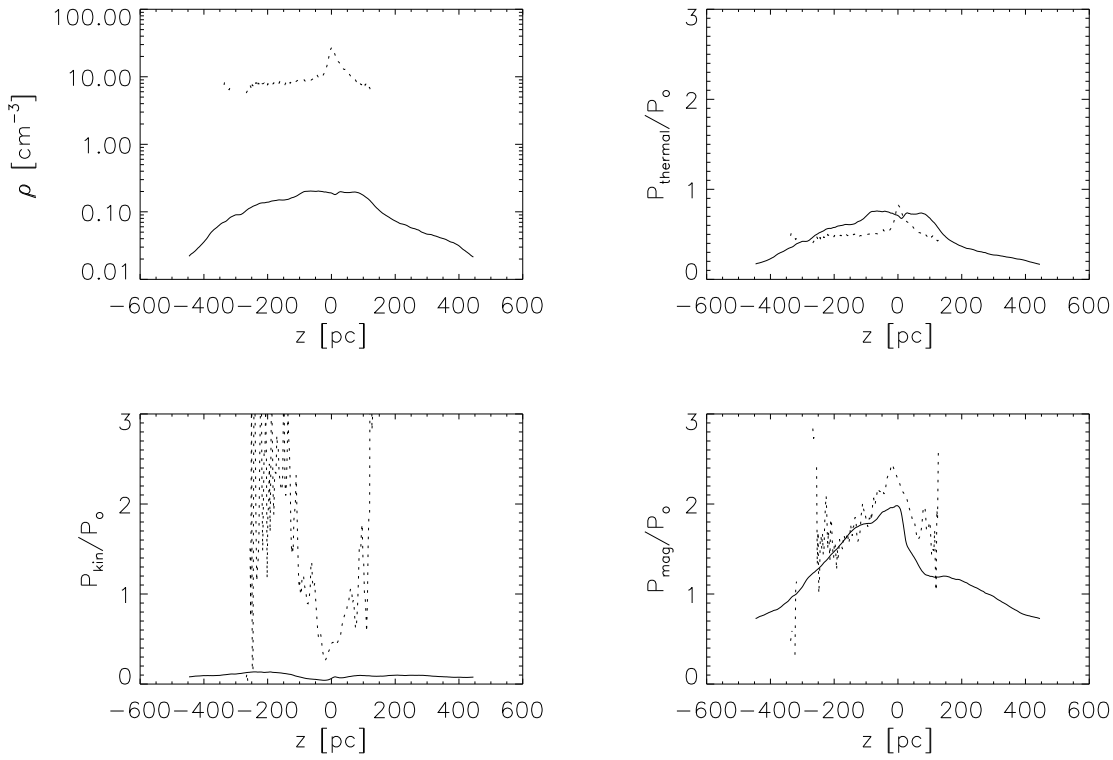

Figure 4.17: Typical density and pressure for the high gravity model. The warm phase corresponds to the solid line, while the cold phase is shown as the dotted line.

medium is around 10 cm^{-3}, increasing significantly towards the mid-plane. The typical density of the warm medium is around 0.1 cm^{-3}, also increasing towards the mid-plane, but the distribution is much more broad. The typical kinetic pressure of the cold medium can be very large, but this is only at high z where little CNM is actually present. The kinetic pressure is large here as the cold medium is driven to approximately the same velocity as the warm medium, but has a much higher density than the warm medium. The kinetic pressure in the warm gas varies much less in z than any other pressure, but is only half of the mid-plane thermal value. The kinetic pressure of cold gas everywhere exceeds its thermal pressure. The typical magnetic pressure of the warm and cold phases have similar magnitudes and profiles. The thermal pressures of the warm and cold phases are approximately equal near

the mid-plane. The thermal pressure decreases quickly for the cold medium away from the mid-plane, while tapering off more slowly in the warm medium. Generally, the same trends and behaviors are seen in the standard gravity run.

Since it is the derivatives of the pressures, rather than the magnitude, which actually counterbalance the force of gravity, we plot $(dP/dz)/(\rho \mathbf{g}_{ext})$ for the thermal, kinetic and magnetic pressures, also including the B_z^2 term separately. The combined results from the high gravity run are shown in Figure 4.18. These profiles have all been smoothed with a boxcar average. The ratio of the total pressure to $\rho \mathbf{g}_{ext}$ (thick solid line) is roughly one, indicating that the disk is in approximate pressure equilibrium with gravity. The magnetic pressure is the dominant contributor to the support of the disk. Kinetic support is fairly minimal overall, but in the mid-plane where most of the cold medium is present, there is a noticeable increase in the kinetic contribution. The thermal term is also significant throughout most of the disk, but decreases somewhat near the mid-plane, and at around 150 pc is larger than the magnetic term.

We plot the same quantities for the standard model in Figure 4.19. The magnetic pressure is again primarily the dominant term. At high latitude, however, the magnetic pressure decreases at about the same height that thermal pressure increases. The ratio of the total pressure to $\rho \mathbf{g}_{ext}$ deviates significantly from one, an indication that this model is out of equilibrium. The total pressure follows the magnetic pressure fairly closely, as the other terms are either small or have approximately the same amplitude, but differing sign, and so cancel each other out. The disk in the low gravity model is even further out of equilibrium; the pressure derivatives are shown in Figure 4.20. It is difficult to draw conclusions from plots such as these. Longer temporal and spatial baselines are needed to improve the statistics. One interesting behavior to note, however, is that in the standard and low gravity models

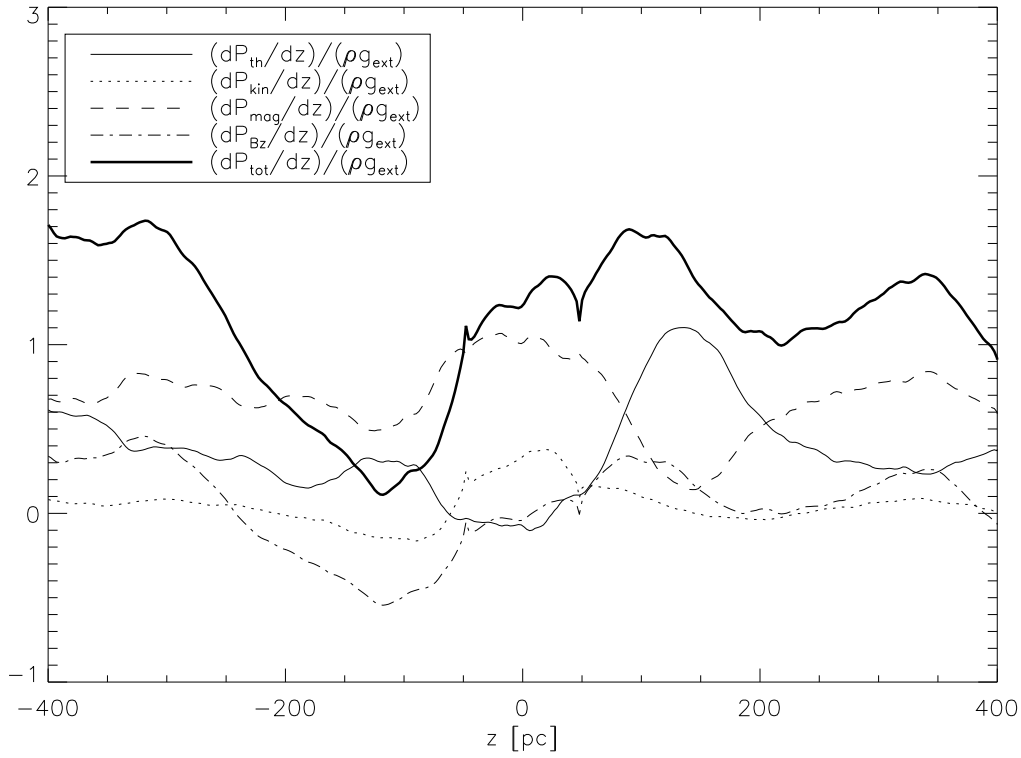

Figure 4.18: Pressure gradient profiles compared to $\rho \mathbf{g}_{ext}$ for the combined medium, for the high gravity model.

the magnetic pressure is anti-correlated with the thermal pressure. If the magnetic pressure is high, the thermal pressure is low, and vice versa.

4.4 Summary and Discussion

We have performed simulations of the ISM which include a two-phase model of the ISM, galactic shear, magnetic fields and vertical gravity. This allows us to study the MRI in the presence of a two phase medium, where the vertical structure of the disk is determined self consistently.

The typical turbulent velocities averaged over the last three orbits are 3.7, 2.3, and 1.4 km s^{-1} for the warm, unstable, and cold phases, for our standard gravity run. The velocity dispersions in the high and low gravity models are comparable.

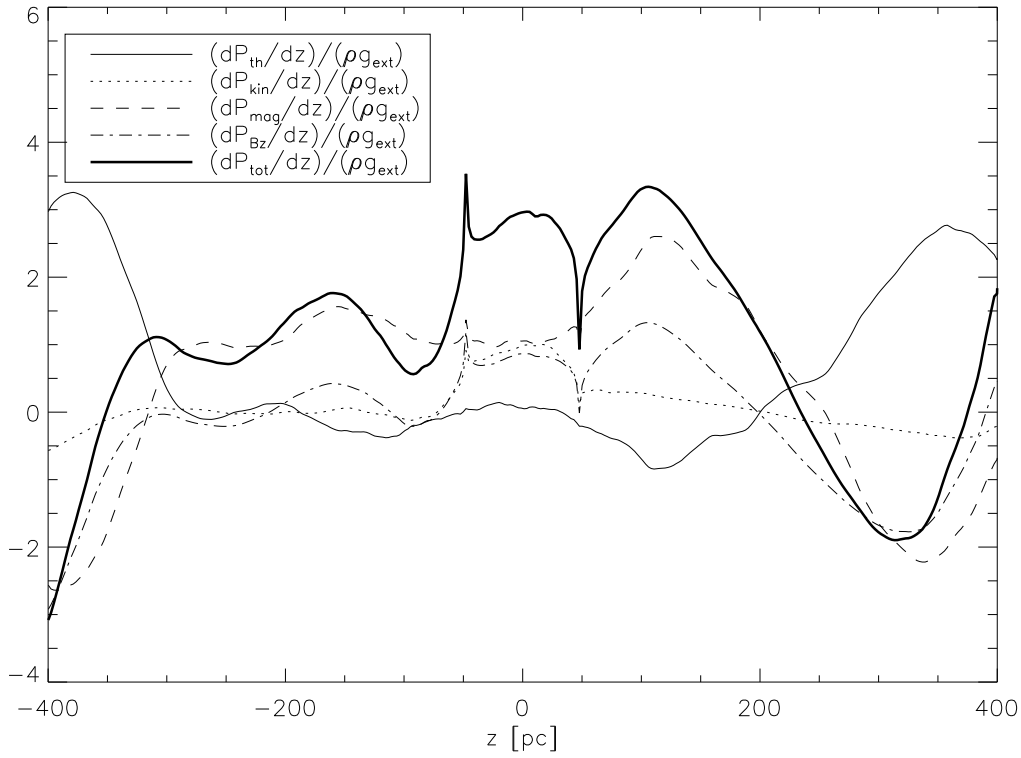

Figure 4.19: Pressure gradient profiles compared to $\rho \mathbf{g}_{ext}$ for the combined medium, for the standard gravity model.

This is significantly smaller than the 7 km s^{-1} observed by Heiles & Troland (2003). In the 3D models of Paper II, the warm and cold gas was well mixed, and had essentially the same velocity. In these stratified models, however, the cold gas is only found at the mid-plane, where the volume filling fraction of the warm gas is thus significantly smaller, and the mean density higher. If the mean density of the mid-plane gas was reduced, such as by pressure due to cosmic rays or SNE, the turbulent velocities of the cold gas as driven by the MRI would likely increase.

The MRI amplifies the initial magnetic field strength of 0.26 μG by more than a factor of ten. The saturated state field strength is around 3 μG in the cold and unstable phases, and 2 μG in the warm phase. These values are consistent with present day observational estimates of the turbulent field strength in the Milky Way,

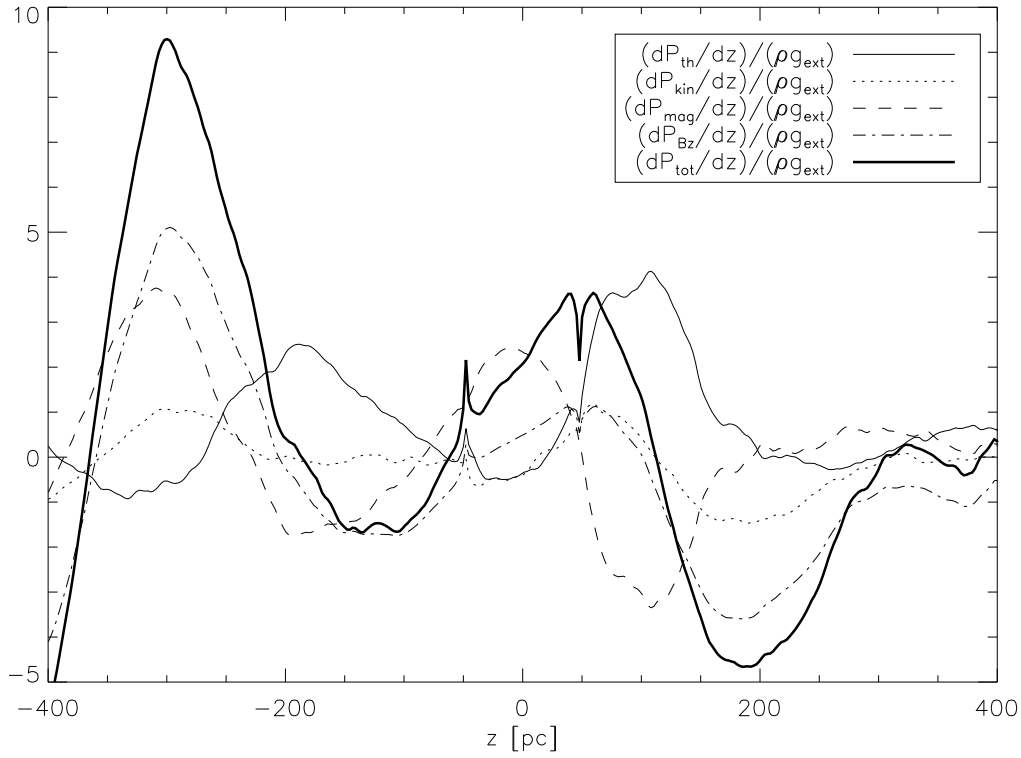

Figure 4.20: Pressure gradient profiles compared to $\rho \mathbf{g}_{ext}$ for the combined medium, for the low gravity model.

which represents approximately half of the total $|\mathbf{B}|$. The field strength weakens slightly in the low gravity model, and increases slightly in the high gravity model.

The mass fractions in the warm, unstable, and cold phases are also of particular interest. For the turbulent models, the cold mass fraction is (60,59,73)%, and the warm mass fraction is (22,23,17)%, from low to high gravity. The mass fraction in the unstable phase is (17,17,11)%. We can compare these results to those of the non-turbulent models, which for the cold medium are (81,86,92)% from low to high gravity. The mass fraction in the warm medium makes up the balance, (19,14,7)%, with very little mass found in the unstable phase. Generally, the same trends in the mass fractions are observed in the turbulent and non-turbulent models, although the turbulence significantly reduces the amount of cold gas. The mass fraction of the

cold medium increases with the strength of gravity, and the scale height of the cold medium decreases with increasing gravity, in both the turbulent and non-turbulent models. The mass fraction in the warm medium is decreasing with increasing gravity. In the turbulent case, the mass fraction in the unstable phase also decreases with gravity.

The mass weighted density PDFs do show the signature of a two-phase medium, though the peak at high density is quite broad. The distribution of gas extends to very high and low densities, spanning 5 orders of magnitude. The temperature PDFs also show two phases of gas to be present, though again the low temperature peak is fairly broad. The overall distribution in the pressure PDF would lead one to believe that rough pressure equilibrium is far from the case, though the mean pressures in the warm and cold phases are approximately equal, $P/k = 1600$ and 1700 K cm^{-3} for the standard gravity model.

We can compare the thickness of the cold component to $c_{eff}/\sqrt{\widetilde{\mathbf{g}}}$, where c_{eff} is taken to be the Alfvén speed, $v_A = B_0/(4\pi\rho_0)^{1/2}$. For our high gravity run, using values of the typical magnetic pressure and density in the mid-plane, give a thickness of about 30 pc, which is larger than our measured scale height of 15 pc.

How do our scale heights compare to observations? Turbulence from the MRI can thicken the disk of CNM as compared to our non-turbulent models, but not in a way that is consistent with local observations. Lockman & Gehman (1991) find that the vertical HI distribution is close to Gaussian, with a full width half max height of 300 pc, corresponding to an exponential scale height of 130 pc. This is consistent with the warm medium scale height for our non-turbulent model, but this is smaller than we have found for the warm medium in our turbulent model. In addition, the HI observations do not indicate two components with distinctly different values of H, as we have found for our warm and cold components. We therefore conclude

that other processes need to mix cold gas to higher z, in order to be consistent with observational estimates of the overall vertical profile.

It is still possible that the MRI may be a significant source of turbulence in the outer regions of the galaxy, but further simulations must be performed in order to explore the relevant parameter space. The surface density in the outer galaxy is approximately half of the value we've adopted in our simulations. It is possible that models with a smaller surface density will have thicker cold disks, with increased turbulent amplitudes.

Acknowledgments

We are grateful to Charles Gammie, Woong-Tae Kim, Jim Stone, and Mark Wolfire for valuable discussions. This work was supported in part by grants NAG 59167 (NASA) and AST 0205972 (NSF). Some of the computations were performed on the Tungsten cluster at NCSA, and others were performed on the CTC cluster in the UMD Department of Astronomy.

Chapter 5

Summary and Prospects

5.1 Summary

The ISM of spiral galaxies has long been a topic of great interest. The papers of Field (1965); Field, Goldsmith, & Habing (1969) paved the way for McKee & Ostriker (1977) to the develop what is today considered to be the classical picture of the ISM. In this picture, The diffuse matter of the ISM is composed of cold, high density clouds, enshrouded in a warm, low density ambient medium. The warm and cold components are in rough pressure equilibrium with each other, and little material is to be found in the thermally unstable regime. Turbulence in the ISM is primarily driven by SNE, also creating a hot component filling a large fraction of the volume.

This view of the ISM has been called into question in recent years, in part because both simulations and observations have found large amounts of gas to exist in what should be a thermally unstable state. The majority of these simulations include turbulence which is driven by SNE, but whether or not SNE are included correctly is a matter of debate. One major concern is that the SNE modeled in these simulations do not occur in high density gas with $n > 1000$ cm^{-3}, as is

realistic for type II SNE that explode within GMCs. Also, observations have shown that turbulence levels in regions of high and low star formation are similar, which is difficult to understand if turbulence is driven only by SNE. With this in mind, we have explored the MRI as a possible source of turbulence in the ISM.

We began this thesis with 2D simulations, presented in Chapter 2, that served to lay the groundwork for 3D simulations to come, developing the numerical foundation which allowed us to study thermal instability with the ZEUS MHD code. We adopted a piece-wise power law cooling function (Sánchez-Salcedo, Vázquez-Semadeni, & Gazol 2002), which is based on the work of Wolfire et al. (1995), and also included thermal conduction, which is necessary in order to numerically resolve the modes TI. Prior to this work simulations of the ISM which have included the MRI have had only modest (order-unity) contrasts in density. In the absence of turbulence, our cooling function yields a two phase medium with a density contrast of approximately 100 between the warm and cold phases of gas. In our 2D simulations we were able to study the initial development of the MRI, and its effect on the phase structure of the gas.

These simulations were extended to 3D in Chapter 3, which permitted us to study the saturated state of the MRI in the presence of a two-phase medium. Turbulence levels in the warm, unstable and cold phases were examined. PDFs of temperature and density generally showed that there remained two distinct phases of gas, warm and cold, though turbulence from the MRI was able to drive some gas into the unstable regime.

Our 3D simulations were extended to include vertical gravity in Chapter 4. With the inclusion of vertical gravity, the local density of the ISM, and the scale height of the warm and cold disks are determined self-consistently. Turbulence levels in the cold gas are generally consistent with the results presented in Chapter 3, at similar

mean density.

5.2 Conclusions

Our primary results are as follows:

MRI driven turbulence levels are typically ~ 3 km s^{-1} when the mean density of the ISM is approximately 1 cm^{-3}, and the magnetic field strength is $\sim 3\mu G$. This is significantly smaller than the 7 km s^{-1} observed in the ISM of the Milky Way. As the mean density of the ISM changes, the velocity dispersion varies as $\delta v \propto \bar{n}^{-0.77}$ in our unstratified models. Our vertically stratified models yield (mass-weighted) mean densities of 1 - 5 cm^{-3} and mean turbulent velocities of around 4, 2, and 1 km s^{-1} in the warm, unstable, and cold phases, which is roughly consistent with this scaling relationship. The density is higher, and the velocity dispersion lower, than values in the solar neighborhood. Thus, MRI is not more than a partial contributor to observed local turbulence. In the outer galaxy, it is uncertain exactly what the turbulence levels and scale heights are. Simulations with lower vertical gravity and gas surface density may yield smaller mean densities, thus increasing MRI driven turbulence levels and scale heights, but self consistent stratified simulations with appropriate parameters have yet to be performed.

We have generally found the signature of a two phase medium to be evident in the PDFs of temperature and density in all of our models. Mass weighted PDFs generally show two distinct peaks corresponding to low temperature, high density clouds, and a high temperature, low density ambient medium. The proportion of unstable gas found in our simulations is around 20-25%. We have found that the fraction of unstable gas, by mass, is about the same as the fraction of warm stable gas, with these fractions increasing with the level of turbulence. Even in our most

turbulent models which reproduce the observed velocity dispersion in the Milky Way, the signature of two phases is still evident.

We have addressed the issue of vertical support of the ISM. The scale height of our cold disk is smaller than has been found in our Galaxy, but the height of our warm disk is consistent with observations, around 250 pc. Our high gravity model was found to be in approximate equilibrium with gravity, and magnetic pressure contributes more than thermal and kinetic pressure to the support of the disk. It may be the case that SNE are required to increase the scale height of the cold disk. As the SNE rate is increased, the disk may thicken, at which point the contribution of the MRI to the turbulent amplitudes may increase as well.

How do the results from our simulations compare to the classical picture of the ISM? As have those before us, we have found that turbulence can drive material into the unstable phase. Higher levels of turbulence yield higher levels of unstable gas. Still, the PDFs from our simulations, even in the most turbulent case which yields velocity dispersions comparable to those observed, show two distinct phases of gas. The PDFs of pressure are generally quite broad, though the mean pressure in the warm and cold components are approximately equal. Our feeling is that the classical picture still broadly represents the physical state of the ISM. Turbulence may drive gas into the unstable regime, but this realization does not justify discarding the classical model in favor of a new paradigm. TI is still quite important, and the cloudy structure it yields must be accounted for in future models of the ISM. Rather, the presence of thermally unstable gas in the ISM should be considered an important development in our understanding of the impact of turbulent dynamics on thermodynamics of the ISM, as a modification of the classical model.

5.3 Future Work

There are several avenues of future study which one can pursue to further our understanding of MRI driven turbulence in the ISM. The cooling curves in Wolfire et al. (2003) at differing disk locations vary from those adopted in this work, with differing minimum and maximum allowable pressures for a two-phase medium. Our cooling function is generally consistent with what is expected for the outer disk, but some adjustments could be made. It would be worthwhile to perform simulations which more accurately model the cooling function in both the inner and outer disks.

Another important issue is the energy lost to diffusion of the sheared velocity and magnetic field noted in Chapter 3. This is a result of ZEUS solving a non-conservative form of the energy equation. In principle this could be captured if explicit resistivity and shear viscosity were included, or with a conservative MHD algorithm. This could have a significant effect on the fraction of gas in the unstable regime.

The parameters of our stratified models are consistent with observations of the inner disk of the Milky Way. Simulations which include a realistic $\tilde{\mathbf{g}}$ and Σ for the outer Galaxy should be performed. If the surface density is lower, it's unclear whether the cold disk will simply have a lower mass with similar velocity dispersion and scale height, or if possibly the decrease in mass will allow the cold medium to be pushed to higher z, where turbulent amplitudes are higher.

Finally, models with SNE and/or spiral arms should be performed as well. Their combination/interaction with the MRI may yield very interesting results.

Appendix A

Conductivity & Coupling of Ions and Neutrals in the ISM

A.1 Relative Contribution of Neutrals and Ions to Thermal Conduction

In this thesis we are primarily interested in the neutral hydrogen component of the ISM, which is a significant fraction of the total mass of the ISM. The neutral component is, however, partially ionized. Both the neutral and ionized hydrogen contribute to the total level of thermal conduction, and in this section we compare their relative contributions. The thermal conduction coefficient of neutral hydrogen is $\mathcal{K} = 2.5 \times 10^3\ T^{1/2}$erg cm^{-1} K^{-1} s^{-1} (Parker 1953), which at 7300 K, is $\mathcal{K} = 2.14{\times}10^5$ erg cm^{-1} K^{-1} s^{-1}. We can estimate the contribution of the ionized fraction by computing $\mathcal{K}$ for a fully ionized gas, and then scaling that result by the ionization fraction. From Lang (1974), for a fully ionized gas

$$\mathcal{K} = 2 \times 10^{-4} \frac{T^{5/2}}{Z^4 ln\Lambda} \text{ erg cm}^{-1} \text{ K}^{-1} \text{ s}^{-1}, \tag{A.1}$$

where T is the temperature, and Z is the atomic mass. Λ for an ionized gas is given by (Lang 1974)

$$\Lambda = 1.3 \times 10^4 \frac{T^{3/2}}{N_e^{1/2}}. \tag{A.2}$$

The ionization fraction in the standard model of Wolfire et al. (1995) is $n_e/n = 1.9 \times 10^{-2}$ for the warm component at 7300 K, and $n = 0.37$ cm^{-3}. The conduction coefficient, when weighted by the ionization fraction, is then $\mathcal{K} = 6.84 \times 10^2$ erg cm^{-1} K^{-1} s^{-1}. Thermal conduction by neutral hydrogen is therefore more efficient by approximately three orders of magnitude as compared to the ionized contribution. In the cold medium at 45 K, with an ionization fraction of $n_e/n = 3.3 \times 10^{-4}$, and a mean density of $n = 61$ cm^{-3} (Wolfire et al. 1995), the relative contribution of the ions compared to the neutrals is even smaller.

A.2 Coupling of Neutrals and Ions by Collisions

Finally, we address the issue of whether or not it is appropriate to apply MHD simulations to model the mostly neutral hydrogen of the ISM. Osterbrock (1961) found that the ion-neutral cross section in cold HI to be approximately $\sigma_{in} = 10^{-14}$ cm^2. The mean free path of a neutral for a collision with an ion is $l = (n_i \sigma_{in})^{-1}$, which for a neutral density of $n = 61$ cm^{-3}, and an ionization fraction of $n_e/n = 3.3 \times 10^{-4}$ (Wolfire et al. 1995), we find $l = 5 \times 10^{15}$ cm. We can adopt the thermal velocity of the particles (Lang 1974)

$$v_{Th} = \left(\frac{3kT}{m}\right)^{1/2} = 1 \times 10^5 \text{ cm s}^{-1} \tag{A.3}$$

to yield a typical interaction time of $l/v_{Th} = 5 \times 10^{10}$ s. To this we compare the typical time-scale of motion of the medium in our models. The resolution in our simulations is around 1 pc, and we adopt an upper estimate of the fluid velocity of 10 km s^{-1}, giving a time-scale of 3×10^{12} s, which is significantly longer than

the neutral-ion collision time. The neutral-ion collision time is shorter by a factor of five in the warm medium. The ions and neutrals are therefore well coupled, and the treatment of the mostly neutral atomic component of the ISM under the assumptions of MHD is acceptable.

Bibliography

Audit, E. & Hennebelle, P. 2005, A&A, 433, 1

Balbus, S. A. & Hawley, J.F. 1991, ApJ, 376, 214

Balbus, S. A. & Hawley, J.F. 1992, ApJ, 400, 610

Balsara, D.S., Kim, J., Mac Low, M., & Mathews, G.J. 2004, ApJ, 617, 339

Beck, R. 2004, Astrophys. & Sp. Sci., 289, 293

Bennet, J.O., Donahue, M., Schneider, N., & Voit, M. 2005, The Essential Cosmic Perspective, Third Edition (San Fracisco:Addison Wesley)

Binney, J. & Merrifield, M. 1998, Galactic Astronomy, (Princeton:Princeton University Press)

Brunt, C.M., Heyer, M.H., Vázquez-Semadeni, E., & Pichardo, B. 2003, ApJ, 595, 824

Burkert, A. & Lin, D.N.C 2000, ApJ, 537, 270

de Avillez, M.A. 2000, MNRAS, 315, 479

de Avillez, M.A. & Mac Low, M.-M. 2001a, ApJ, 551, L57

de Avillez, M.A. & Berry, D.L. 2001a, MNRAS, 328, 708

de Avillez, M.A. & Mac Low, M.-M. 2002, ApJ, 581, 1047

de Avillez, M.A. & Breitschwerdt, D. 2004, A&A, 425, 899

de Avillez, M.A. & Breitschwerdt, D. 2005, ApJ, 436, 585

Chiang, W.-H. & Bregman, J.N. 1988, ApJ, 328, 427

Clifford, P. & Elmegreen, B.G. 1983, MNRAS, 202, 629

Cox, D.P. & Smith, B.W. 1974, ApJ, 189, L105

Cox, D.P. 2005, ARA&A, 43, 337

Dalgarno, A. & McCray, R.A. 1972, ARA&A, 10, 375

Dib, S., Bell, E., & Burkert, A. 2005, astroph-0506339

Dickey, J.M., Hanson, M.M., & Helou, G. 1990, ApJ, 352, 522

Dickey, J.M. & Lockman, F.J. 1990 ARA&A, 28, 215

Dziourkevitch, N., Elstner, D., & Rüdiger, G. 2004, A&A, 423, 29

Elmegreen, B.G., Scalo, J. 2004, ARA&A, 42, 211

Hawley, J. F. & Evans, C.R. 1988 ApJ, 332, 659

Field, G.B. 1965 ApJ, 142, 531

Field, G.B., Goldsmith, D.W., & Habing, H.J. 1969, ApJ, 155, 149

Ferrara, A. & Shchekinov, Y. 1993, ApJ, 417, 595

Fitzpatrick, E.L., & Spitzer, L., Jr. 1997, ApJ, 475, 623

Gammie, C.F., Lin, T., Stone, J.M., & Ostriker, E.C. 2003, ApJ, 592, 203

Gammie, C.F., Shapiro, S.L., & McKinney, J.C. 2004, ApJ, 602, 312

Gazol, A., Vázquez-Semadeni, E., Sánchez-Salcedo, F.J., & Scalo, J. 2001, ApJ, 557, L121

Gazol, A., Vázquez-Semadeni & Kim, J. 2005, 630, 911

Goodman, J. & Xu, G. 1994 ApJ, 432, 213

Han, J.L., Ferriere, K., & Manchester, R.N. 2004, ApJ, 610, 820

Han, J.L., Manchester, R.N., & Qiao, G.J. 1999, MNRAS, 306, 371

Hawley, J.F. & Balbus, S.A. 1991, ApJ, 376, 223

Hawley, J.F. & Balbus, S.A. 1992, ApJ, 400, 595

Hawley, J.F., Gammie, C.F., & Balbus, S.A., ApJ, 440, 742 (HGB1)

Hawley, J.F., Gammie, C.F., & Balbus, S.A., ApJ, 464, 690 (HGB2)

Hawley, J.F., & Stone, J.M. 1995 Computer Physics Communications, 89, 127

Hawley, J.F., Balbus, S.A., & Stone, J.M. 2001, ApJ, 554, L49

Heiles, C. 2001, ApJ, 551, L105

Heiles, C. & Troland, T.H. 2003, ApJ, 586, 1067

Heiles, C. 2004, in Star Formation In the Interstellar Medium eds. D. Johnstone, F.C. Adams, D.N.C. Lin, D.A. Neufeld and E.C. Ostriker (ASP:San Francisco, p. 79)

Hennebelle, P. & Pérault, M. 1999, A&A, 351, 309

Hennebelle, P. & Pérault, M. 2000, A&A, 359, 1124

Heyer, M.H. & Brunt, C.M. 2004, ApJ, 615, L45

Jenkins, E.B. 2004, Astrophys. & Sp. Sci., 289, 215

Kalberla, P. M. W., Schwarz, U. J., & Goss, W. M. 1985, A&A, 144, 27

Kim, W. & Ostriker, E.C. 2000, ApJ, 540, 372

Kim, W. & Ostriker, E.C. 2001, ApJ, 559, 70

Kim, W., Ostriker, E.C., & Stone, J.M. 2002, ApJ, 581, 1080

Kim, W., Ostriker, E.C., & Stone, J.M. 2003, ApJ, 599, 1157

Korpi, M.J., Brandenburg, A., Shukurov, A., Tuominen, I., & Nordlund, Å. 1999, ApJ, 514, L99

Koyama, H. & Inutsuka, S. 2000, ApJ, 532, 980

Koyama, H. & Inutsuka, S. 2002, ApJ, 564, L97

Koyama, H. & Inutsuka, S. 2004, ApJ, 602, L25

Kritsuk, A.G. & Norman, M.L. 2002a, ApJ, 569, L127

Kritsuk, A.G. & Norman, M.L. 2002b, ApJ, 580, L51

Kritsuk, A.G. & Norman, M.L. 2004, ApJ, 601, L55

Lang, K.R. 1974, Astrophysical Formulae, (Berlin:Springer-Verlag)

Lockman, F.J. & Gehman, C.S. 1991, ApJ, 382, 182

Mac Low, M.-M., de Avillez, M.A., & Korpi, M.J. 2004 in How does the Galaxy work?, eds. Alfaro, E.J., Pérez, E., Franco, J., (Berlin:Springer)

Mac Low, M. & Klessen, R.S. 2004, RevModPhys, 76, 125

Mac Low, M., Balsara, D., Kim, J., & de Avillez, M.A. 2005, ApJ, 626, 864

McClure-Griffiths, N.M., Green, A.J., Dickey, J.M., Gaensler, B.M., Haynes, R.F., & Wieringa, M.H. 2001, ApJ, 551, 394

McKee, C.F. & Ostriker, J.P. 1977, ApJ, 218, 148

Miller, K.A. & Stone, J.M. 2000, ApJ, 534, 398

Mohan, R., Dwarakanath, K.S., & Srinivasan, G. 2004, J. of Astrophys. & Astron., 25, 185

Osterbrock, D.E. 1961, ApJ, 134, 270

Parker, E.M. 1953, ApJ, 117, 431

Ostriker, E.C., Stone, J.M., & Gammie, C.F. 2001, ApJ, 546, 980

Petric, A. & Rupen, M.P. 2001, in Gas and Galaxy Evolution eds. J.E. Hibbard, M.P. Rupen, & J.H. van Gorkom (ASP:San Francisco), p. 288

Piontek, R.A. & Ostriker, E.C. 2004, ApJ, 601, 905 (Paper I)

Piontek, R.A. & Ostriker, E.C. 2005, ApJ, 629, 849 (Paper II)

Press, W.H., Teukolsky, S.A., Vetterling, W.T., & Flannery, B.P. 1992, Numerical Recipes in C, Second Edition (Cambridge:Cambridge University Press)

Refield, S. & Linsky, J.L. 2004, ApJ, 613, 1004

Rosen, A. & Bregman, J.N. 1995, ApJ, 440, 634

Sánchez-Salcedo, F.J., Vázquez-Semadeni, E., & Gazol, A. 2002, ApJ, 577, 768

Sano, T., Inutsuka, S., Turner, N.J., & Stone, J.M. 2004, ApJ, 605, 321

Sellwood, J.A. & Balbus, S.A. 1999, ApJ, 511, 660

Shu, F.H, Adams, F.C., & Lizano, S. 1987, ARA&A, 25, 23

Slyz, A., Devriendt, J., Bryan, G., & Silk, J. 2005, MNRAS, 356, 737

Spitzer, L., Jr. 1978, Physical Processes in the Interstellar Medium (New York:Wiley)

Spitzer, L., Jr.& Fitzpatrick, E.L. 1995, ApJ, 445, 196

Stone, J.M., Hawley, J.F, Gammie, C.F, & Balbus, S.A. 1996, ApJ, 463, 656

Stone, J.M. & Norman, M.L. 1992a, ApJ, 80, 753

Stone, J.M. & Norman, M.L. 1992b, ApJ, 80, 791

Strong, A.W., Moskalenko, I.V., & Reimer, O. 2000, ApJ, 537, 763

Taylor, A.R., et al. 2003, AJ, 125, 3145

Truelove, J.K., Klein, R.I., McKee, C.F., Holliman, J.H., II, Howell, L.H., & Greenough, J.A. 1997, ApJ, 489, L179

Turner, N.J., Stone, J.M., Krolik, J.H., & Sano, T. 2003, ApJ, 593, 992

van Zee, Liese, & Bryant, J. 1999, AJ, 118, 2172

Vázquez-Semadeni, E., Gazol, A., & Scalo, J. 2000, ApJ, 540, 271

Vázquez-Semadeni, E., Gazol, A., Passot, T., Sánchez-Salcedo, J. 2003, in Turbulence and Magnetic Fields in Astrophysics, eds. E. Falgarone and T. Passot, (Berlin:Springer-Verlag) p. 213

Verschuur, G.L., & Magnani, L. 1994, AJ, 107, 287

Wada, K. & Norman, C.A. 1999, ApJ, 516, L13

Wada, K., Spaans, M., & Kim, S. 2000, ApJ, 540, 797

Wada, K. & Norman, C.A. 2001a, ApJ, 547, 172

Wada, K. 2001b, ApJ, 559, L41

Wada, K. & Koda, J. 2001c, PASJ, 53, 1163

Wada, K., Meurer, G., & Norman, C.A. 2002, ApJ, 577, 197

Williams, J.P., de Geus, E.J., & Blitz, L. 1994, ApJ, 428, 693

Wolfire, M.G., Hollenbach, D., Mckee, C.F., Tielens, A.G.G.M., & Bakes, E.L.O. 1995, ApJ, 443, 152

Wolfire, M.G, Mckee, C.F., Hollenbach, D., & Tielens, A.G.G.M. 2003, ApJ, 587, 278

Zuckerman, B. & Palmer, P. 1974, ARA&A, 12, 279